

This is to certify that the dissertation entitled

HEMODYNAMIC MONITORING BY SYSTEM IDENTIFICATION

presented by

ZHENWEI LU

has been accepted towards fulfillment of the requirements for the

Ph.D. degree in Electrical Engineering

Major Professor's Signature

7/24/06

Date

MSU is an Affirmative Action/Equal Opportunity Institution

LIBRARY Michigan State University

PLACE IN RETURN BOX to remove this checkout from your record. TO AVOID FINES return on or before date due. MAY BE RECALLED with earlier due date if requested.

DATE DUE	DATE DUE	DATE DUE

2/05 p:/CIRC/DateDue.indd-p.1

HEMODYNAMIC MONITORING BY SYSTEM IDENTIFICATION

Ву

Zhenwei Lu

A DISSERTATION

Submitted to
Michigan State University
in partial fulfillment of the requirements
for the degree of

DOCTOR OF PHILOSOPHY

Department of Electrical and Computer Engineering

2006

ABSTACT

HEMODYNAMIC MONITORING BY SYSTEM IDENTIFICATION

By

Zhenwei Lu

The hemodynamic variables, cardiac output (CO), left atrial pressure (LAP), and left ventricular contractility in terms of the maximum elastance (E_{lv}^{max}), may be utilized either individually or collectively to guide therapy in patients with cardiovascular disease. However, the conventional methods for monitoring each of these variables are highly invasive and/or operator dependent, thereby limiting their clinical application. In this dissertation, we introduce three signal processing techniques for monitoring the aforementioned hemodynamic variables. The unifying theme of the three techniques is the analysis of subtle beat-to-beat variations in cardiovascular signals that may be routinely measured in clinical practice using the system identification method in conjunction with prior physiologic knowledge. The three techniques specifically aim to monitor 1) CO changes from a single peripheral arterial blood pressure (ABP) waveform, 2) CO changes and absolute LAP from either a pulmonary artery pressure waveform or a right ventricular pressure waveform, and 3) E_{lv}^{max} changes from random-interval, respiratory-induced ABP variations. In this dissertation, we also initially validate each of these techniques with respect to hemodynamic data obtained from realistic computer simulations, animal subjects, human volunteers, and patients. With further successful testing, the techniques may ultimately be employed to expand the monitoring of CO,

LAP, and E_{lv}^{max} in clinical applications such as critical care, home health care, and even combat casualty care.

To my wife, Ling Mei,
my parents, Fujiang Lu and Xian Zhang,
and my sister, Tian Lu.

ACKNOWLEGDEMENTS

I want to thank these people who make this thesis work become possible. First of all, I am deeply indebted to my advisor Dr. Ramakrishna Mukkamala for introducing me to the cardiovascular signal processing research area and guiding me through all the thesis work. He has set a role model of a serious and hardworking young scientist. He was always there to help and encourage me. His unique approach of physiological monitoring by system identification is the basis of this thesis. Moreover, the first technique in the thesis is the continuous research of his work in MIT.

I would like to thank my thesis committee, Dr. Bari Olivier, Dr. Robert Scheluter and Dr. Lalita Udpa. Their invaluable guidance is very important for the completion of this thesis. Especially, Dr. Bari Olivier and his laboratory helped us collect the dog data for the preliminary evaluation of the second and third techniques presented in the thesis. And he gave good suggestions about the experiment design and the thesis writing.

I am grateful to my colleagues for their generous help: Mr. Jacob Kuiper, who helped me download and evaluate the two sets of ICU data; Mr. Rafat Elahi, who generated the simulation data; and Dr. Ahmed Türkman, who gave me valuable suggestions in algorithm development. I enjoyed working with them. I also want to thank those scientists who provided the ICU patients data and the non-invasive data for technique evaluations.

Finally, I thank my wife Ling Mei. I believe that without her love, understanding, and encouragement during the past four years, I could not have completed the thesis work. I thank my parents for their selfless love even they are on the other side of the

planet. I also thank my teachers from the elementary school to graduate school and my former advisors in China.

This work is supported by Michigan State University, National Heart and Lung Institute Grant HL-080568, and American Heart Association Grant SDG 0535523Z.

TABLE OF CONTENTS

LIST OF	TABLES	ix
LIST OF	FIGURES	x
CHAPT!	ER 1	
INTROI	DUCTION	1
1.1	Hemodynamics	1
1.2	Conventional Hemodynamic Monitoring	1
1.3	Hemodynamic Monitoring by System Identification	3
1.4	Thesis Organization and Contributions	3
CHAPT:	ER 2	
BACKG	ROUND	6
2.1	Cardiovascular System	
2.1.		
2.1.		
2.1.	-	
2.2	System Identification Analysis in Hemodynamics	
2.2.		
2.2.		
	NUOUS MONITORING OF CARDIAC OUTPUT FROM A PERIPHERA LIAL BLOOD PRESSURE WAVEFORM	
3.1	Background	
3.2	The Technique	31
3.3	Technique Evaluation	41
3.3.		
3.3.		
3.3.	- · · · · · · · · · · · · · · · · · · ·	
3.4	Evaluation Results	
3.5	Discussion	
	1 Potential Sources of CO Error	
3.5.	· · · · · · · · · · · · · · · · · · ·	
3.5.		
3.5.		
3.5.	5 Potential Applications of the Mathematical Analysis Technique	58
CHAPT		
	NUOUS MONITORING OF CARDIAC OUTPUT AND LEFT ATRIAL	
	JRE FROM A PULMONARY ARTERY PRESSURE OR RIGHT	
	ICULAR PRESSURE WAVEFORM	
4.1	Background	60

4.2 Moi	nitoring of CO and LAP from PAP	63
4.2.1	The Technique	63
4.2.2	Technique Evaluation	69
4.2.3	Evaluation Results	72
4.2.4	Discussion	75
4.3 Moi	nitoring of CO and LAP from RVP	78
4.3.1	The Technique	78
4.3.2	Pilot Evaluation of the Technique	80
4.3.3	Results	81
CHAPTER 5		
MONITORIN	G LEFT VENTRICULAR CONTRACTILITY FROM RESPIR	ATORY-
INDUCED B	LOOD PRESSURE VARIABILITY	84
5.1 Bac	kground	84
5.2 Phy	siologic Basis	90
5.2.1	Respiratory-Induced Pa Variability Mechanisms	90
5.2.2	Direct Capacitive Effects	
5.2.3	Ventilatory Mechanism	97
5.2.4	Three Indices Derived From E _{lv}	99
5.3 Sign	nal Processing Algorithm	100
5.4 Eva	luation	
5.4.1	Theoretical Evaluation	106
5.4.2	Pilot Experimental Evaluation	110
5.5 Eva	luation Results	
5.5.1	Theoretical Evaluation Results	111
5.5.2	Pilot Experimental Evaluation Results	115
5.6 Disc	cussion	118
CHAPTER 6		
CONCLUSIO	NS	122
6.1 Sun	nmary	122
6.2 Futi	re Work	123
BIBLIOGRA	PHY	126

LIST OF TABLES

Table 3.1: Advantages and disadvantages of some conventional cardiac output (CO) measurement techniques	. 27
Table 3.2: Summary of the intensive care unit patient records and CO estimation result of the invasive human hemodynamic data set	
Table 3.3: Summary of the healthy young adult records and CO estimation results of t non-invasive human hemodynamic data set	
Table 4.1: Summary of the intensive care unit patient records and cardiac output (CO) and left atrial pressure (LAP) estimation results of the human hemodynamic data set	
Table 6.1 Summary of three hemodynamic monitoring techniques	123

LIST OF FIGURES

Figure 1.1 A simple diagnostic algorithm based on the monitoring of cardiac output (CO), left atrial pressure (LAP) and left ventricular maximum elastance (E_{lv}^{max})
Figure 2.1 Two-element Windkessel model of systemic circulation in terms of its electrical circuit analog
Figure 2.2 Two-element Windkessel model of pulmonary circulation in terms of its electrical circuit analog
Figure 2.3 Interaction between heart rate (HR) and ABP
Figure 2.4 Hemodynamic signals and electrocardiogram (ECG) waveforms in one cardiac cycle
Figure 2.5 Left ventricular pressure-volume loop
Figure 2.6 Respiratory waves on ABP waveform
Figure 2.7 Illustration of respiratory sinus arrhythmia
Figure 2.8 Power spectrum of HR fluctuation
Figure 3.1 Comparison of the changes in blood pressure (BP) and cardiac output (CO) during venesection and resulting faint
Figure 3.2 Illustration of thermodilution CO and pulmonary capillary wedge pressure (PCWP) measurements using pulmonary artery catheter (PAC)
Figure 3.3 The technique of Bourgeois et al for monitoring CO from ABP waveform 32
Figure 3.4 Comparison of central ABP measured in aorta and peripheral ABP waveforms measured in radial artery
Figure 3.5 Two swine ABP waveforms measured at the same time but at different sites in the arterial tree
Figure 3.6 ABP waveform (top panel) can be viewed as a sum of a group of blood pressure responses (lower panels) to cardiac contractions
Figure 3.7 Illustration of identifying the time constant τ from a peripheral ABP waveform

Figure 3.8 Visual examples of CO estimation results in three intensive care unit (ICU) patients
Figure 3.9 Visual examples of CO estimation in three healthy subjects
Figure 4.1 Illustration of pulmonary capillary wedge pressure (PCWP) measurement 62
Figure 4.2 Illustration of construction of pulmonary artery pressure (PAP) from right ventricular pressure (RVP) during ejection phase
Figure 4.3 PAP waveform and pulmonary circulation Windkessel model
Figure 4.4 Illustration of identifying the time constant τ and LAP from a PAP waveform
Figure 4.5 Illustration of the "knee" order selection algorithm
Figure 4.6 PCWP measurement evaluation procedure
Figure 4.7 Visual examples of CO and LAP estimation from three intensive care unit (ICU) patients
Figure 4.8 Illustration of identifying the time constant τ and LAP from RVP
Figure 4.9 Estimation results of CO and LAP from long time-interval PAP waveform and RVP waveform in a dog
Figure 5.1 Illustration of left ventricular elastance (E_{lv}) and the left ventricular maximum elastance (E_{lv}^{max})
Figure 5.2 Illustration of conventional E _{lv} measurement method
Figure 5.3 Respiratory waves on ABP waveform. 92
Figure 5.4 Illustration of respiratory sinus arrhythmia (RSA)
Figure 5.5 Two-compartment model of the left ventricle and systemic arteries in terms of the electrical circuit analog
Figure 5.6 Model of ventilatory mechanics in terms of its electrical circuit analog 98
Figure 5.7 Illustration of enhanced venous return phenomenon
Figure 5.8 Random interval breathing power spectrum is much wider than spontaneous breathing power spectrum

Figure 5.9 Illustration of system identification of index h ₁	104
Figure 5.10 Block diagram summarizing the human cardiovascular simulator	108
Figure 5.11 Summary of theoretical evaluation results against the corresponding ac simulator E _{lv} ^{max} value	
Figure 5.12 Pressure signals in canine experiment of monitoring left ventricular contractility	116
Figure 5.13 Comparison of our technique with a highly invasive measurement of ca	

CHAPTER 1

INTRODUCTION

1.1 Hemodynamics

Cardiovascular disease is the number one cause of mortality in the United States. A properly functioning, well-regulated cardiovascular system is essential to meet the metabolic and mechanical demands of the various physiologic and pathophysiologic situations. Hemodynamics is a branch of cardiovascular physiology studying the dynamic properties of blood: flow (velocity), pressure, volume, and their relationships. It is very important for the body to maintain the hemodynamic parameters in a narrow range despite a wide variety of physiological perturbations. Otherwise, the person may be in serious status. For example, a very low arterial blood pressure (ABP) may cause the death of the brain in a few seconds, and low cardiac contractility may cause heart failure. Therefore, hemodynamic monitoring is extremely important for directing therapy in patients with cardiovascular disease.

1.2 Conventional Hemodynamic Monitoring

Most current hemodynamic monitoring systems provide continuous, automatic measurements of blood pressures. Invasive fluid-filled catheters are broadly utilized in critically ill patients to monitor the pressures in the radial artery and pulmonary artery. Peripheral ABP may be measured non-invasively via tonometry and finger-cuff

photoplethysmography. Right ventricular pressure (RVP) could be measured by implanted devices (e.g., two-lead pacemaker).

To a large extent, conventional patient monitoring systems simply measure and display physiologic signals without attempting to interpret them. As a result, these systems are limited in that they require a high level of invasiveness, necessitate an operator, and/or provide nonspecific clinical information. For instance, the continuous monitoring of ABP is commonly utilized to help physicians to assess the patients' cardiovascular status. However, the main limitation of this monitoring is that the measured ABP are multi-factorial and therefore not sufficiently specific to guide therapy. For example, hypotension or low pressure may be caused by the inability of the heart to fill or contract or the inability of the circulation to return blood to heart. To assess the hemodynamic status, the measurement of other clinical parameters such as cardiac output (CO) is desirable (Fig. 1.1). The thermodilution method is currently employed in most intensive care units (ICU) and operating rooms to measure CO. This method involves inserting a pulmonary artery catheter (PAC), injecting cold saline in the right atrium, measuring temperature change downstream in the pulmonary artery, and then computing CO using conservation of mass laws. This method is very invasive and only warrants use in a subset of critically ill patients. In addition, because an operator is required, the CO cannot be monitored continuously. Finally, it is not very accurate due to the many assumptions upon which it is based.

Other important specific hemodynamic parameters include left atrial pressure (LAP) and cardiac contractility. Left atrial pressure (LAP), also known as left heart filling pressure, can be utilized together with CO to distinguish between circulatory and

cardiac diseases. The standard LAP monitoring method is the pulmonary capillary wedge pressure (PCWP) method. This method also requires an operator and is therefore discrete. Left ventricular maxim elastance (E_{lv}^{max}) is a specific index heart contractility. The monitoring of E_{lv}^{max} can help detect left ventricular systolic failure. The conventional measurement method of E_{lv}^{max} involves catheterizing the left ventricle through the aorta to measure the left ventricular pressure and volume, altering the loading conditions by, for example, inferior vena cava balloon occlusion, and then computing the slope of the line that best fits the end-systolic pressure-volume points. This method is clearly too invasive for routine use.

1.3 Hemodynamic Monitoring by System Identification

In this thesis, we seek to overcome limitations of conventional hemodynamic monitoring systems. Our general approach to advancing the state-of-the-art of patient monitoring systems is to reveal the significant, "hidden" information in routinely measured blood pressure waveforms by employing system identification with physiologic knowledge. In this way, the patient monitoring systems are possibly less invasive, provide automated physiologic assessment, and/or indicate specific clinical parameters that significantly contribute to therapeutic decision-making.

1.4 Thesis Organization and Contributions

The main contributions of this thesis is in the development and evaluation of three techniques for monitoring CO, LAP and/or left ventricular contractility in terms of

 E_{lv}^{max} . Common to the three techniques is the analysis of continuous long time intervals of blood pressure waveforms.

In Chapter 2, we discuss the background for this thesis, namely, cardiovascular physiology, hemodynamic models, and basic system identification algorithms. In chapter 3, we describe a previously developed technique for continuously monitoring CO from peripheral ABP. We then describe the refinement of the technique and its validation, for the first time, in humans. In chapter 4, we extend the algorithm of Chapter 3 to a PAP or RVP waveform for continuously monitoring LAP and CO and describe its preliminary evaluation in ICU patients and a canine experiment. In Chapter 5, we introduce a technique to monitor changes in E_{lv}^{max} from the ABP waveform variations induced by respiratory activity during a random interval breathing protocol. We then describe its evaluation with respect to beat-to-beat variability generated from a realistic human cardiovascular simulator and a canine experiment. Finally, in chapter 6, we summarize the thesis work and outline future directions.

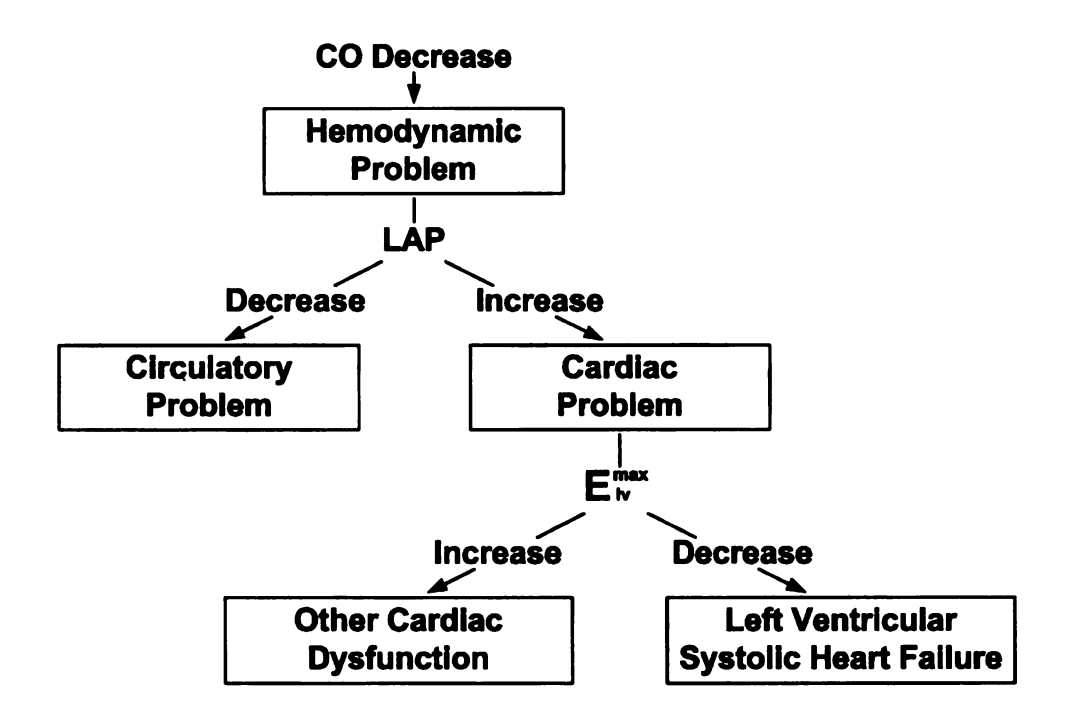


Figure 1.1 A simple diagnostic algorithm based on the monitoring of cardiac output (CO), left atrial pressure (LAP) and left ventricular maximum elastance (E_{lv}^{max}) (Modified from Pinsky and Vincent, 2005).

CHAPTER 2

BACKGROUND

2.1 Cardiovascular System

The cardiovascular system serves to transport and distribute essential substances to the tissues and to remove by-products of metabolism as well as regulate body temperature, adjust oxygen and nutrient supply and etc. [Berne and Levy, 1998]. The cardiovascular system includes the circulatory system and the nervous control system.

2.1.1 Circulations

The circulatory system consists of a pump (the heart), a series of distributing and collecting tubes (blood vessels), and thin vessels for exchange between the tissues and the vascular channels (capillaries). The vascular system is composed of two major subdivisions in series with one another: the pulmonary circulation and systemic circulation. Each subdivision consists of several types of vessels (e.g., arteries, capillaries, veins) aligned in series with one another. In the pulmonary circulation, the right ventricle propels oxygenated blood through the lungs for exchange of oxygen and carbon dioxide. In the systemic circulation, the left ventricle propels blood to all other tissues of the body.

There have been numerous models of the circulation. For example, Fig. 2.1 shows a simple electrical analog model of the systemic circulation. Here, the left heart is represented by a current source supplying the CO. The systemic arterial tree is represented by a two-element Windkessel model accounting for the lumped compliance

of the large arteries (arterial compliance, AC) and the total peripheral resistance (TPR) of the small arteries. The veins are not considered in the model, because due to the high value of TPR, the venous pressure is usually negligible with respect to ABP.

Similarly, the pulmonary circulation could also be modeled as an electrical circuit as shown in Fig. 2.2. The right heart is represented by a current source supplying the CO; pulmonary vessels (including arteries, capillaries and veins) are represented by a Windkessel model accounting for pulmonary vessel compliance (PVC) and pulmonary vessel resistance (PVR). LAP must be considered in the model, because the pulmonary circulation is a low pressure system.

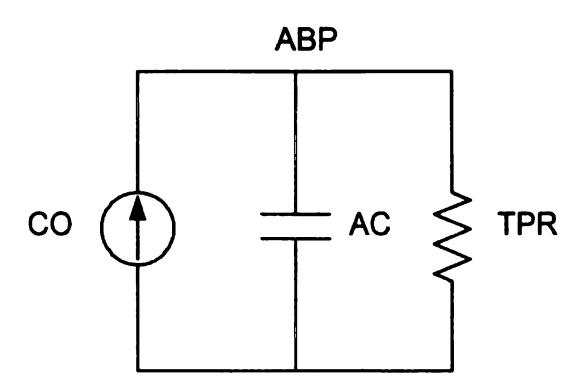


Figure 2.1 Two-element Windkessel model of systemic circulation in terms of its electrical circuit analog. Left ventricle is represented by a current source with a value of cardiac output (CO) and arterial tree is represented by total peripheral resistance (TPR) and arterial compliance (AC). ABP, arterial blood pressure.

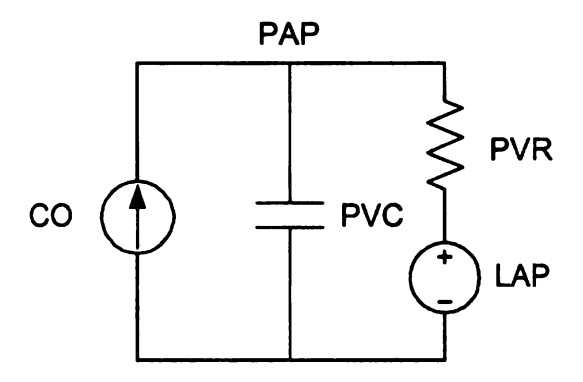


Figure 2.2 Two-element Windkessel model of pulmonary circulation in terms of its electrical circuit analog. Right ventricle is represented by a current source with a value of CO and pulmonary vessels are represented by pulmonary vessel resistance (PVR) and pulmonary vessel compliance (PVC). LAP, left atrial pressure.

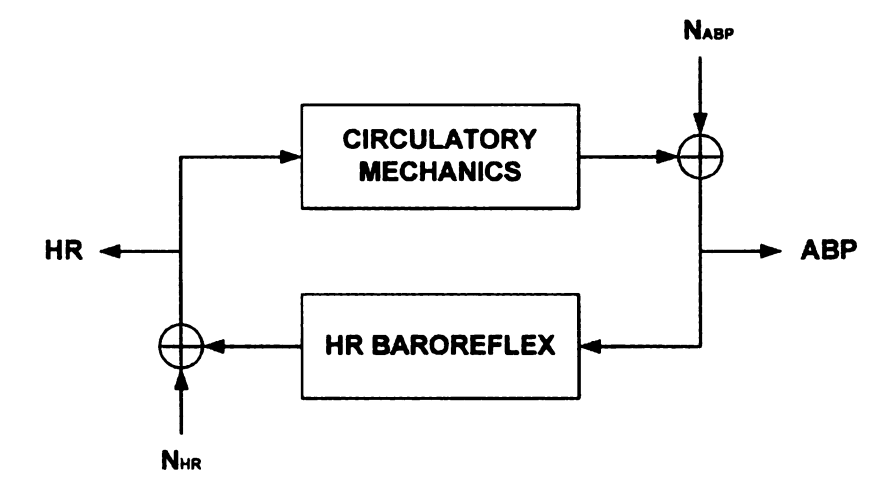


Figure 2.3 Interaction between heart rate (HR) and ABP. N_{HR} , N_{ABP} , noise disturbance of HR and ABP.

2.1.2 Cardiovascular Regulation

A principle objective of the cardiovascular system is to maintain ABP within a narrow range in order to drive blood through the tissues and provide oxygen and other essential substances. This goal is realized by not only the mechanical system (circulation), but also the cardiovascular regulatory system. In the short term (seconds to minutes, which is the focus of this thesis), the arterial and cardiopulmonary baroreflex feedback systems are normally responsible for extrinsic regulation over short time scales of seconds to minutes. For example, ABP is sensed via baroreceptors that lie in the carotid sinus and aortic arch and this pressure is transferred to the brainstem via afferent nerve fibers. The brain then try to keep ABP near its desired value by adjusting heart rate (HR), left ventricular contractility (i.e., E_{lv}^{max}), TPR, and systemic venous unstressed volume (SVUV). If ABP decreases, then HR, ventricular contractility and TPR would increase, while SVUV would decrease. Then, ABP would be increased back towards its desired value via the mechanical system. Thus, the system is closed-loop. For example, HR affects ABP through circulatory mechanics, while ABP also affects HR through the baroreflex feedback control system (Fig. 2.3) [Mullen et al., 1997].

2.1.3 Hemodynamic Waveforms

Knowledge of the variability of hemodynamic signals (blood pressures, flows and volumes) and the electrocardiogram (ECG) is very important in this thesis. In this section, we will discuss the waveform variability and the mechanisms underlying this phenomenon.

Intra-Beat Variability

The cardiac cycle refers to the sequence of electrical and mechanical events occurring in the heart during a single beat. These events result in the changes of blood pressures, volumes and flows, and the body surface potential that is usually monitored with the ECG. The waveforms of aortic pressure (AOP, central ABP), left ventricular pressure (LVP), LAP, left ventricular volume, and ECG during one cardiac cycle are shown in Fig. 2.4. Ventricular systole (contraction) and diastole (relaxation) can be defined in terms of both mechanical and electrical events. In mechanical terms, systole is defined as the period between the closure of the mitral valve and the closure of the aortic valve. In electrical terms, it is the period between the QRS complex and the end of the "T" wave in the ECG signal. Ventricular diastole is remaining time of the cardiac cycle. Systole is composed of the isovolumetric contraction phase and the ejection phase. During the ejection phase, the aortic valve is opened and blood flows out from the ventricle, thus the ventricular volume decreases and the waveforms of AOP and LVP are overlapped. In the remaining of the cardiac cycle, the aortic valve closes, thus the AOP waveform is always above the LVP waveform due to the blood conservation effect of the AC. Note that the "R" wave in the ECG waveform corresponds to the beginning of isovolumetric contraction, when the LVP begins to increase rapidly and the mitral valve closes. Two waves appear in LAP waveform during one beat: the "a" wave after the "P" wave of the ECG and the "v" wave after the "T" wave of the ECG (Fig. 2.4). The "v" wave corresponds to the end of the isovolumetric relaxation when the mitral valve opens. PAP and right ventricular pressure (RVP) waveforms are very similar with AOP and

LVP respectively except that their values are much lower. As implied above, a left ventricular pressure-volume loop of the cardiac cycle in Fig. 2.4 is shown in Fig. 2.5.

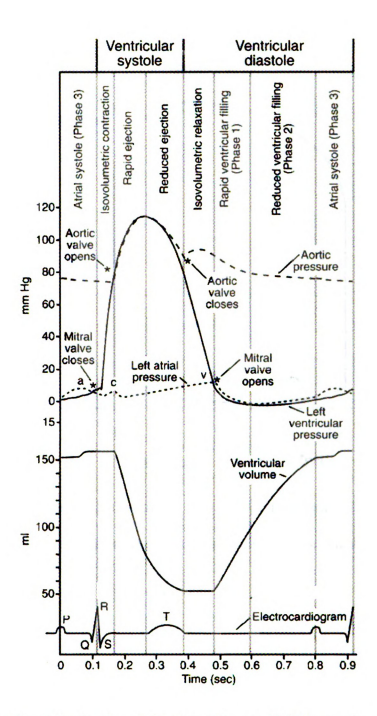


Figure 2.4 Hemodynamic signals and electrocardiogram (ECG) waveforms in one cardiac cycle. Aortic pressure, left ventricular pressure, LAP, left ventricular volume and ECG are shown from top to bottom. Ejection happens when the aortic valve is open. "a" and "v" waves are apparent in LAP waveform. "R" wave in ECG corresponds to the beginning of ventricular systole.

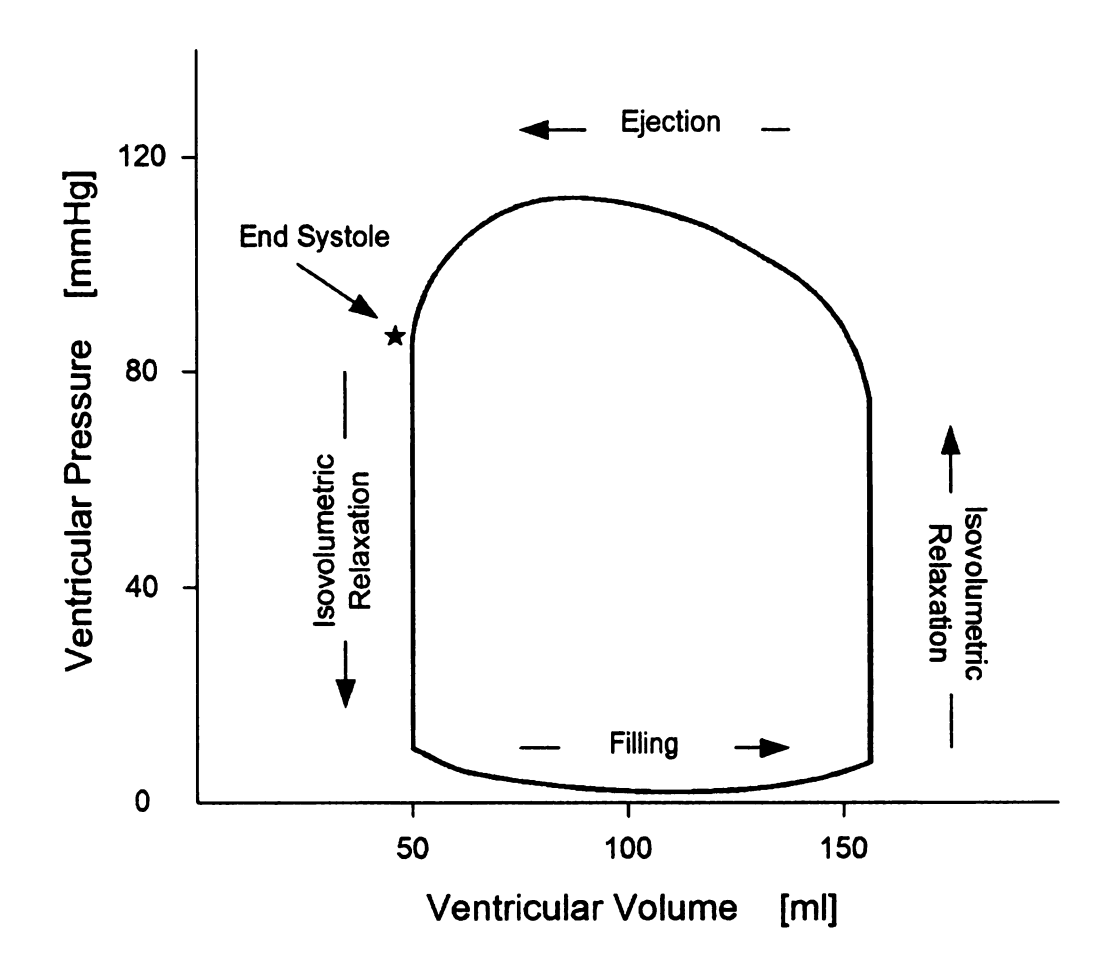


Figure 2.5 Left ventricular pressure-volume loop. The pressure and volume corresponds to the pressure and volume in the cardiac cycle shown in Fig. 2.4. The star marks the end systole.

Beat-to-Beat Variability

Hemodynamic waveforms also vary from beat-to-beat due to various naturally occurring physiological perturbations and the response of the short-term cardiovascular regulation to these perturbations. For example, the beat-to-beat fluctuations in ABP due to respiration are clearly seen in Fig. 2.6. These fluctuations are caused by both the mechanical effects and the autonomic nervous system. The variation of intrathoracic pressure caused by chest expansion (inspiration) or chest contraction (expiration) mechanically perturbs the venous return, ventricular pressure, and the arterial pressure. Autonomic mechanisms are responsible for the respiratory sinus arrhythmia phenomenon in which HR and respiratory variations are in synchrony (Fig. 2.7) [Eckberg et al., 1984; Saul and Cohen, 1994]. The HR changes will then cause ABP changes through circulation. These mechanisms are mediated by the fast parasympathetic nervous system and the slower sympathetic nervous system [Akselrod et al., 1981]. Another example of an ongoing perturbation is fluctuations in the TPR as vascular beds regulate their own resistance in order to match blood flow demand. These fluctuations in turn can perturb arterial pressure and affect HR.

With the conventional power spectral analysis, we can study the frequency content of the fluctuations in HR (Fig. 2.8). The short-term fluctuations are normally concentrated in three principal spectral peaks: low-frequency peak (0.02-0.09 Hz), mid-frequency peak (0.09-0.15Hz), and high-frequency peak (respiratory frequency). The two lower frequency peaks in the power spectrum proves that other perturbations (e.g., autoregulation of local vascular beds) aside from respiration exist.

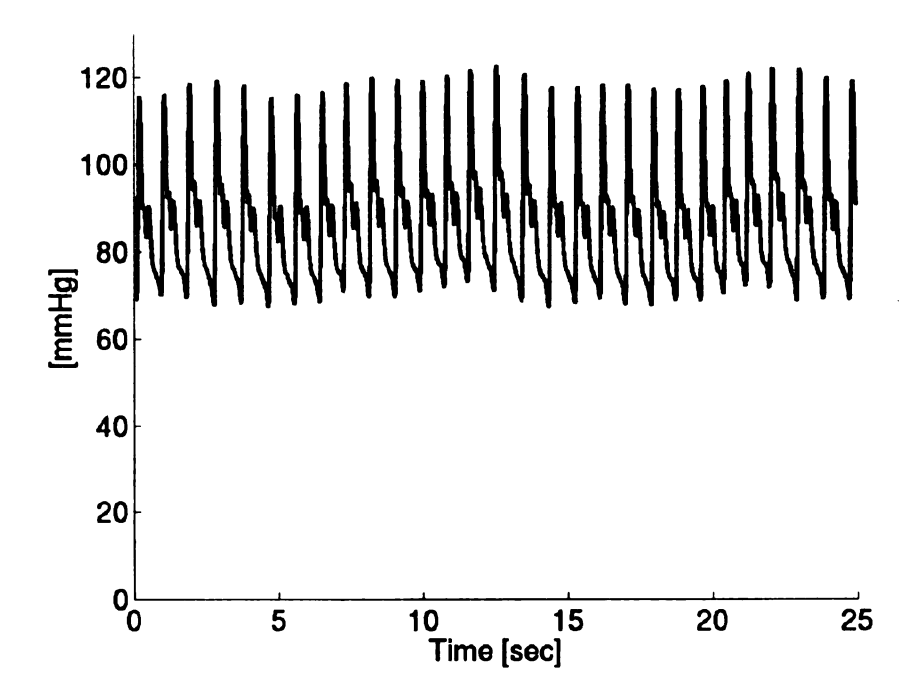


Figure 2.6 Respiratory waves on ABP waveform.

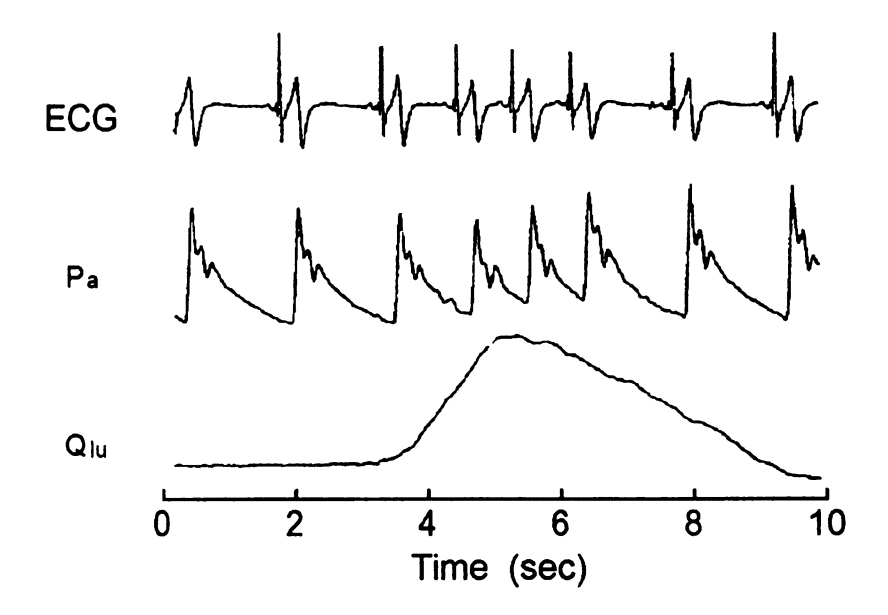


Figure 2.7 Illustration of respiratory sinus arrhythmia. The heart rate (ECG) is in synchrony with the respiratory activity (Q_{lu} , instantaneous lung volume).

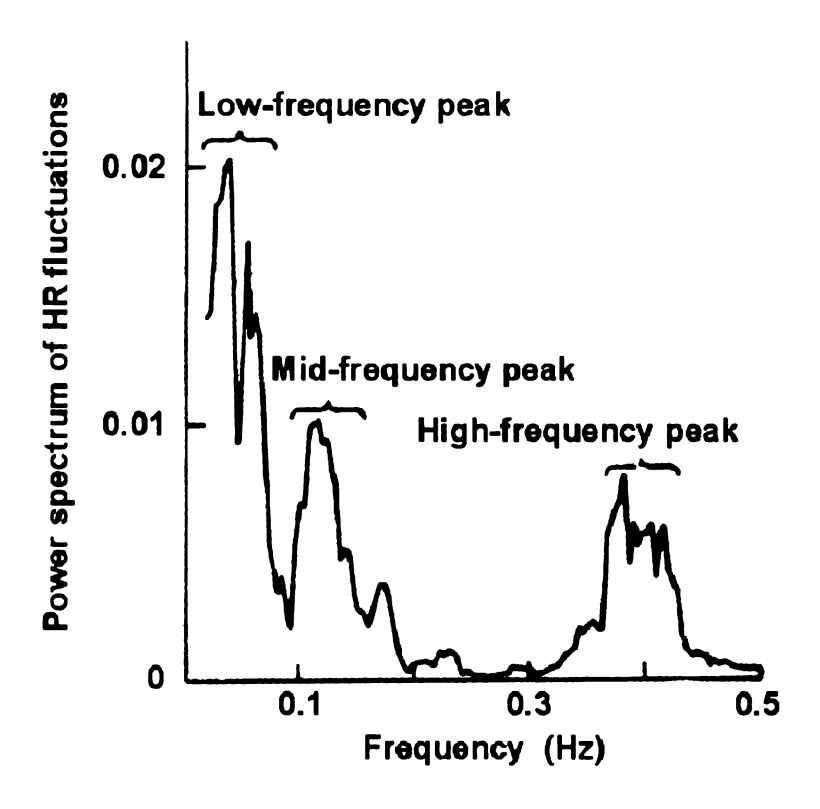


Figure 2.8 Power spectrum of HR fluctuation featuring 3 main peaks: low-frequency peak (0.02-0.09 Hz), mid-frequency peak (0.09-0.15Hz), and high-frequency peak (around respiratory frequency) [Akslrod et al., 1981].

2.2 System Identification Analysis in Hemodynamics

The construction of the cardiovascular models described in Fig. 2.1 and Fig. 2.2 is called forward modeling, which could be utilized in hemodynamic computation. For example, the blood flow can be computed from ABP by solving differential equations based on the systemic circulation model shown in Fig. 2.1. The inverse modeling problem is to identify dynamic models from observed data. This approach is called system identification and is the basis of signal processing methods used in this thesis. System identification could be categorized into nonparametric and parametric methods.

2.2.1 Nonparametric Identification

Multivariable statistical methods such as cross-correlation functions, cross-spectra, and nonparametric transfer functions have been used to analyze the relationships between fluctuations in different cardiovascular signals [Mullen et al., 1997]. Consider an LTI (linear time invariant) system whose input-output relationship can be expressed as follows:

$$y(t) = \sum_{k=-\infty}^{\infty} h(k)u(t-k) + e(t),$$
 (2.1)

where t is discrete time; u(t), input; y(t), output; h(t), impulse response; and e(t), unobserved, stochastic process that is uncorrelated to u(t). Thus, the output signal can be computed by convolving the impulse response and the input signal plus an unobserved noise signal. The impulse response is defined to be the system response to an arbitrarily narrow, unit-area input and completely characterizes the LTI system. The Fourier

transform of the impulse response, transfer function, may be estimated from input-output data in closed-form as follows:

$$H(e^{j2\pi f}) = \frac{S_{uy}(e^{j2\pi f})}{S_{uu}(e^{j2\pi f})},$$
(2.2)

where $S_{uy}(e^{j2\pi f})$ is the cross-spectrum from u(t) to y(t); $S_{uu}(e^{j2\pi f})$, auto-spectrum of u(t); and $H(e^{j2\pi f})$, optimal transfer function in the least squares sense [Ljung, 1999], which is also known as the Wiener filter. Since the cross-spectrum is generally complex, $H(e^{j2\pi f})$ provides both magnitude and phase characteristics of the system. The nonparametric transfer function has been used to analyze the arterial heart rate baroreflex system [Berger et al., 1989b] and respiratory sinus arrhythmia.

Nonparametric identification methods have proven to be powerful analytic tools because they are easy to use and capable of giving unique results without assuming any model structure. However, the major limitation is that they only can be utilized in identifying systems operating in open-loop. For example, in Fig. 2.3, the nonparametric transfer function analysis of HR and ABP fluctuations would provide a single transfer function relating the two variables and include the properties of both circulatory mechanics and HR baroreflex. These two totally distinct physiological mechanisms would thus be intertwined together. Therefore, neither circulatory mechanics cannot be characterized due to the existence of the baroreflex system. Similarly, the HR baroreflex characteristics cannot be obtained either.

2.2.2 Parametric Identification

On the other hand, the parametric identification may be even more illuminating. The advantage of this approach is that it provides a quantitative characterization of the open-loop hemodynamic mechanisms responsible for coupling the variability between hemodynamic signals despite the pressure of the feedback. Beginning from the middle to late 1980s, parametric identification has become an increasingly popular approach for quantitatively probing cardiovascular mechanisms. Next, we will introduce three mathematical models popularly utilized for parametric identification.

ARX Model and MA model

Amongst different existing models, the autoregressive exogenous input (ARX) model is perhaps the most widely employed parametric model in system identification. For example, in Fig. 2.3, since each pathway of the closed-loop coupling is causal, parametric identification has been utilized to estimate the circulatory mechanics and HR baroreflex separately [Mullen et al., 1997]. Each channel can be represented by an ARX model and quantitated with a limited number of parameters. The details of the ARX modeling approach are described below.

Given an LTI causal system, where u(t) is the input, y(t) is the output, and e(t) is an unobserved white noise disturbance that is uncorrelated with the input, the ARX model can be conveniently represented as follows:

$$y(t) = \sum_{i=1}^{n} a_i y(t-i) + \sum_{i=0}^{m} b_i u(t-i) + e(t).$$
 (2.3)

The unknown coefficients $\{a_i\}$ and $\{b_i\}$ are respectively referred to as the autoregressive (AR) and exogeneous parameters. The AR part refers to the effect of the past values of y(t) on the current value of y(t); the exogeneous part refers to the effect of the past and

current values of u(t) on the current value of y(t). The constants m and n are model orders limiting the number of these parameters. The coefficients may be estimated from measured input-output data by minimizing the variance of e(t) via the closed form linear least squares solution. The Z transform of the ARX model may be expressed with the following equation:

$$Y(z) = \frac{B(z)}{1 - A(z)}U(z) + \frac{E(z)}{1 - A(z)},$$
 (2.4)

where $A(z) = a_1 z^{-1} + a_2 z^{-2} + \cdots + a_n$, $B(z) = b_0 + b_1 z^{-1} + b_2 z^{-2} + \cdots + b_m$, and E(z) is the Z transform of the unobserved noise e(t). This equation illustrates that the influence of the unobserved, white disturbance on the system output is colored by the AR coefficients. Thus, the ARX model is able to represent LTI systems in the presence of colored noise. The impulse response h(t) can be obtained by substituting $u(t) = \delta(t)$ into Eq. 2.3. The transfer function H(z) is the Z transform of the impulse response h(t) and may be computed with the following equation:

$$H(z) = \frac{\sum_{k=0}^{n} b_k z^{-k}}{1 - \sum_{k=1}^{m} a_k z^{-k}}.$$
 (2.5)

If the AR part is removed from Eq. 2.3, we obtain a finite impulse response (FIR) model as follows:

$$y(t) = \sum_{i=0}^{m} b_i u(t-i) + e(t).$$
 (2.6)

Here, the output only depends on the input. For an LTI causal system represented by Eq. 2.6, the impulse response h(t) is actually the coefficients $\{b_i\}$. The coefficients $\{b_i\}$ could

be estimated by the linear least squares solution from measured input-output data. The Z transform of the FIR model is as follows:

$$Y(z) = B(z)X(z) + E(z)$$
. (2.7)

OE Model

The relationship between x(t) and y(t) may also be represented by an output error (OE) model given in Z transform as follows:

$$Y(z) = \frac{B(z)}{1 - A(z)}X(z) + E(z).$$
 (2.8)

Comparison of Models

Comparing Eq. 2.4, Eq. 2.7 and Eq. 2.8, we can see that the three models are different based on the noise portion. The unobserved noise e(t) is "colored" by AR coefficients in the ARX model, whereas e(t) is not limited by this assumptions in FIR and OE model. One big advantage of the ARX and FIR models is that they can be conveniently estimated by solving the linear equations 2.3 and 2.6 using the linear least squares solution. In contrast, the parameters of the OE model have to be estimated numerically by, for example, Newton's iteration method. Another advantage of the FIR model is that it does not make any assumptions about the model structure (no poles in Eq. 2.7) and therefore its impulse response has no restriction. However, accurate system identification using an MA FIR model requires a large number of parameters. Thus, the FIR model can only characterize the system whose true impulse response is very short.

Model Order Selection

In order to identify the coefficients of the models, the model orders m and n must be determined. Because the ARX model is perhaps the most widely used, we describe model order selection method based on the ARX model.

Assuming the true model orders in Eq. 2.3 are n_0 and m_0 , and n_0 = m_0 , if the selected model order $n < n_0$, then the estimated model will not include all of the true parameters and therefore lacks the degrees of freedom necessary to represent the system. On the other hand, if the selected model order $n > n_0$, then there would be extra parameters in the estimated model that do not exist in the true model. These extra parameters serve only to make the estimated model more sensitive to the noise during the particular time period [Perrott and Cohen, 1996]. Thus, order selection is a tradeoff between completeness and robustness.

To obtain the true model order, first, a set of candidate model orders are chosen based on the physical properties of system. Next, the best model order is sought from the candidate orders. We cannot choose the order corresponding to the minimum mean square error (MSE) of e(t), because the MSE is a monotonically decreasing function of model order. The most popular strategy is to minimize a theoretically derived formula or criterion, which consists of a goodness-of-fit index such as MSE and a penalty factor for model complexity. The Minimum Description Length (MDL) and Final Prediction Error (FPE) [Ljung, 1999; Perrott and Cohen, 1996] are amongst the most widely used model order selection criteria. The MDL value is computed via the following formula:

$$MDL(k) = \left(1 + k \frac{\log(N)}{N}\right) \frac{\left\|e_k\right\|^2}{N},$$
(2.9)

where k is defined to be the number of parameters contained within the model, N is the number of samples contains in the input and output data sets, and $||e_k||^2$ is the MSE.

Model order selection using the MDL criterion amounts to finding the model amongst the candidate set with the minimum MDL value. The FPE value is computed via the following formula:

$$FPE(k) = \frac{N+k}{N-k} \frac{\|e_k\|^2}{N}$$
 (2.10)

Similarly, model order selection using the FPE criterion aims to find the model order with the minimum FPE value.

CHAPTER 3

CONTINUOUS MONITORING OF CARDIAC OUTPUT FROM A PERIPHERAL ARTERIAL BLOOD PRESSURE WAVEFORM

3.1 Background

Since cardiac output (CO) represents the total flow of blood supplying all the tissue beds of the body, it is perhaps the most valuable indicator of overall cardiovascular health. For example, circulatory status is typically monitored through ABP, which is easy to measure. However, in the early stages of a bleed, ABP is maintained while CO is falling due to the body's multiple feedback and control systems (Fig. 3.1) [Barcroft et al., 1944]. Thus, continuous CO monitoring would provide an early indication of deleterious changes in circulatory status and thereby provide sufficient time for successful therapy.

Due to the importance of CO, it is currently monitored in most ICUs and surgical suites in order to guide therapy for critically ill patients. These patients include, for example, those in shock (e.g., cardiogenic, septic, and hemorrhagic) or heart failure and those during and after surgery (e.g., coronary artery bypass grafting or heart valve replacement). An ideal method for CO measurement should be continuous (autonomous operation), minimally invasive, accurate, and inexpensive. Although numerous techniques have been developed for the measurement of CO, none of the conventional techniques possesses all these characteristics (Table 3.1) [Ehlers et al., 1986]. Consider, for example, the standard thermodilution technique, which is currently employed in most ICUs and surgical suites. This technique involves introducing a pulmonary artery catheter (PAC) [Swan et al., 1970] in the right heart, injecting cold saline in right atrium, and

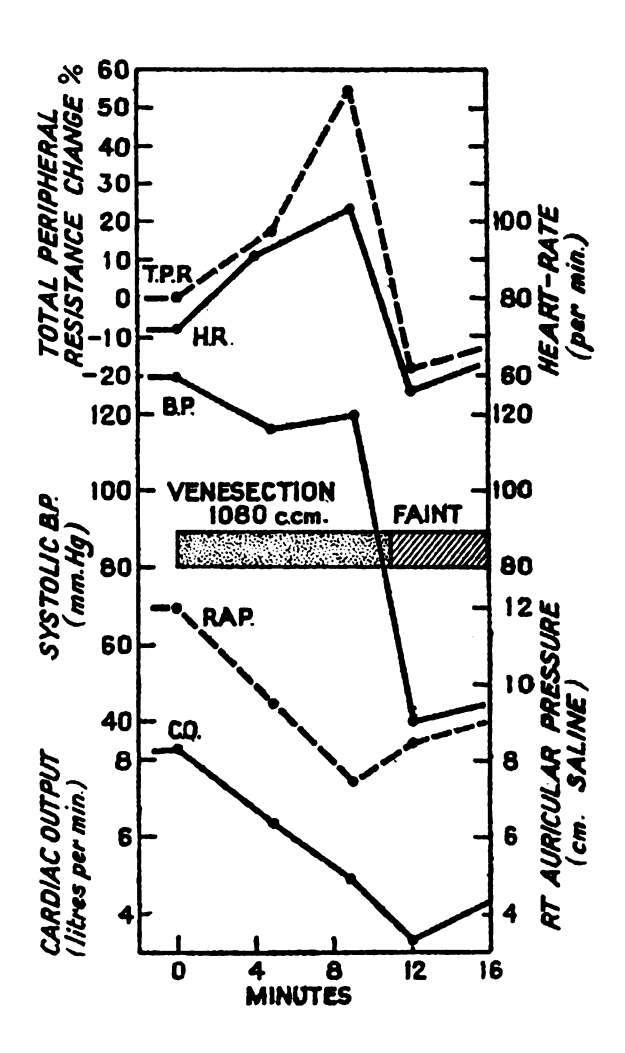


Figure 3.1 Comparison of the changes in blood pressure (BP) and cardiac output (CO) during venesection and resulting faint. Until to the end of venesection, BP is maintained by peripheral vasoconstriction (increased total peripheral resistance) in spite of falling CO. During the faint, the cardiac output increases slightly and the fall in BP is therefore due to the decrease in total peripheral resistance (TPR) [Barcroft et al., 1944].

measuring the temperature downstream in the pulmonary artery (Fig. 3.2). The average CO over the measurement period may then be computed based on conservation of mass laws. Although the technique is relatively inexpensive, it is very invasive and does not operate autonomously. Moreover, the measurement is not very accurate due to the many assumptions upon which it is based (e.g., no saline recirculation and thorough blood mixing) [Ehlers et al., 1986]. As a result, it is used in only a minority (e.g., 10-20%) of all critically ill patients [Rapoport et al., 2000]. In fact, although PAC can be utilized to measure pressures (right atrial, right ventricle, pulmonary capillary wedge pressure, and pulmonary artery pressures) as well as other important hemodynamic parameters (e.g., CO, LAP, mixed venous oxygen saturation), the apparent failure to demonstrate improvements in patient outcome and risks associated with the PAC use have long been criticized and therefore the applications of PAC are falling in this decade [Pinsky and Vincent, 2005]. Another conventional technique for monitoring CO is transthoracic impedance. Thoracic bioimpedance involves the placement of voltage sensing and current transmitting electrodes on the chest, which may be regarded as a conductor whose impedance is altered by changes in blood volume and velocity with each heartbeat. Stroke volume is calculated from an equation involving baseline and maximum rate of change in impedance, ventricular ejection time, and thoracic segment length. This measurement technique is non-invasive and operates autonomously; however, it is generally considered to be very inaccurate, especially in critically ill patients who often have excessive lung fluids [Critchley et al., 1998]. Doppler ultrasound methods, which measure the Doppler shift in the frequency of an ultrasound beam reflected from the flowing aortic blood, require an expert operator to stabilize an external ultrasound

transducer as well as expensive equipment. The most accurate, conventional technique for measuring CO involves surgically implanting a flow probe, either electromagnetic or ultrasonic, directly on the aorta. Although this technique operates autonomously, it does require the drastic procedure of opening the chest. A practical, continuous, minimally invasive or non-invasive CO monitoring method would benefit not only ICU and surgical suite care but also potentially home health care, primary care, and even combat casualty care.

Table 3.1: Advantages and disadvantages of some conventional cardiac output (CO) measurement techniques [Ehlers et al., 1986]

CONVENTIONAL TECHNIQUES	ADVANTAGES	DISADVANTAGES		
Aortic Flow Probe	most accurate; continuous	thoracotomy; expensive		
Doppler Ultrasound	accurate; non-invasive	expert operator; expensive		
Oxygen Fick	inexpensive	two catheterizations; inaccurate; discrete		
Thermodilution	inexpensive	heart catheterization; inaccurate; discrete		
Transthoracic Impedance	non-invasive; inexpensive; continuous	inaccurate		

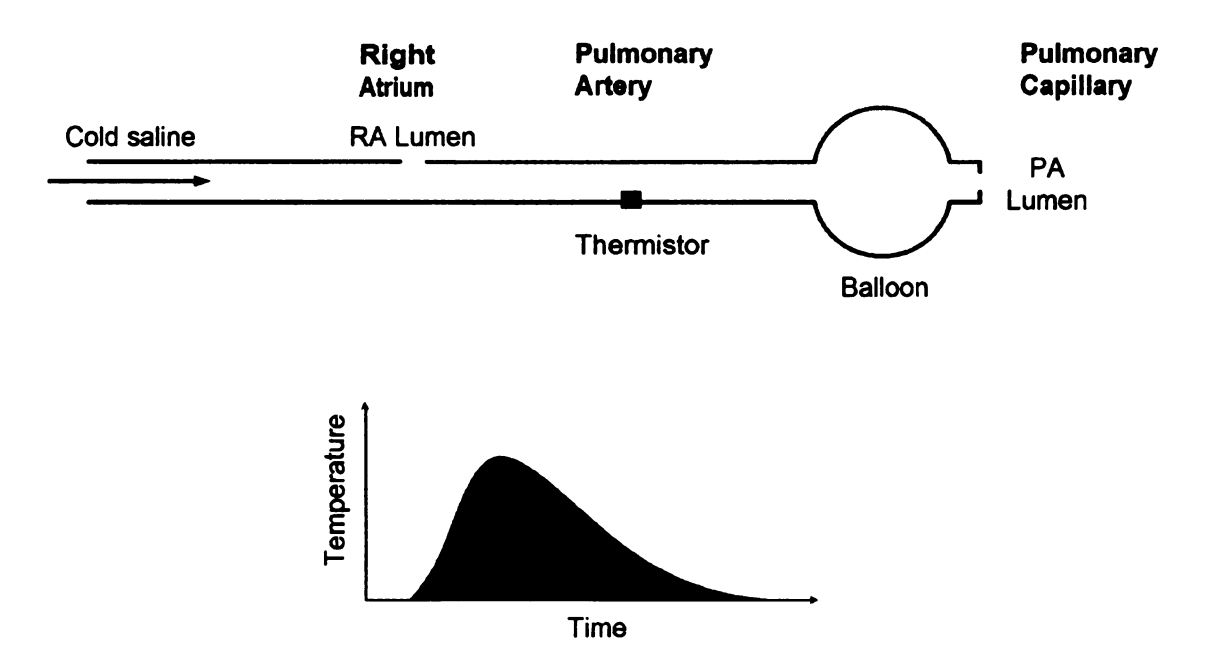


Figure 3.2 Illustration of thermodilution CO and pulmonary capillary wedge pressure (PCWP) measurements using pulmonary artery catheter (PAC). PAC is a flow-directed balloon-tipped catheter. Thermodilution measurement steps: insert PAC into pulmonary artery through right heart, inject cold saline from syringe to right atrium, measure the temperature changes downstream in pulmonary artery and compute CO by the mass conservation law. The curve on the bottom is the temperature measured in pulmonary artery by a thermistor. CO measurement value is proportional to the reciprocal of the area below the curve. PCWP measurement: after inserting PAC into pulmonary artery, position the tip in a small branch of pulmonary artery, and inflate the balloon to occlude blood flow. The pressure measured is PCWP.

While the measurement of CO has proven to be difficult, peripheral arterial blood pressure (ABP), which is related to CO through arterial tree, may be measured reliably and continuously via minimally invasive radial artery catheterization. Indeed, this relatively safe procedure is performed in a majority (e.g., 50-80%) of all critically ill patients [Rhodes and Sunderland, 2005]. Moreover, totally non-invasive methods have been developed to continuously measure peripheral ABP based on finger-cuff photoplethymography [Imholz et al., 1998] and arterial tonometry. These non-invasive methods are available as commercial systems at present, for example, Finapres Medical System. Indeed, since at least 1904 [Erlanger and Hooker, 1904], numerous investigators have therefore sought analysis techniques to monitor CO from ABP waveforms. Techniques based on an adaptive aorta model, which require ABP waveforms measured at two peripheral sites, have been proposed [Redling and Akay, 1997; Welkovitz et al., 1991]. Learning techniques, which require large training data sets consisting of simultaneous measurements of CO and ABP waveforms obtained over the entire physiologic range, have also been suggested [Cerutti et al., 2001; Gratz et al., 1992; Martin et al., 1994]. Finally, Wesseling et al [1993], Linton et al [2001], and other investigators have proposed techniques requiring only the analysis of a single radial ABP waveform. However, Linton et al only showed that their heuristic technique was accurate over a narrow physiologic range, and several studies have demonstrated limitations of the technique of Wesseling et al [Gerhardt et al., 2001; Houtman et al., 1999].

Although a wide variety of techniques have been proposed, they are all conceptually the same to the extent the waveform analysis is performed only over time scales within a cardiac cycle. However, over such short time scales, peripheral ABP

waveforms are heavily corrupted by complex waves propagating back and forth in the distributed arterial tree. Thus, the previous analysis techniques have generally proven to be too inaccurate for clinical use. To date, no non-invasive method has been clinically accepted as a replacement for thermodilution [Levett et al., 1979; Redling et al., 1997].

Our ongoing hypothesis is that CO may be accurately monitored from ABP variations occurring over time scales greater than a cardiac cycle. This hypothesis originates from transmission line theory, which predicts that the confounding effects of wave reflection will diminish with increasing time scale [Noordergraaf, 1978]. Based on the hypothesis, we previously developed a technique to monitor changes in CO by analyzing a single peripheral ABP waveform over long time scales [Mukkamala et al., 2003a, 2004, 2006]. In this study, we refined the technique and evaluated it, for the first time, in humans based on previously published invasive and non-invasive hemodynamic data sets [Elstad et al., 2001; Moody et al., 1996, 2001; Mukkamala et al., 2003b]. With these data, we were specifically able to compare the application of the technique to 1) invasive peripheral ABP waveforms obtained via radial artery catheterization with reference thermodilution measurements in 15 intensive care unit (ICU) patients in which CO was changing due to disease progression and therapy and 2) non-invasive peripheral ABP waveforms obtained via a commercial finger-cuff photoplethysmography system with reference Doppler ultrasound measurements made by an expert in ten healthy subjects in which CO was altered through pharmacological and postural interventions.

3.2 The Technique

Our technique builds upon the previous pulse contour analysis work of Bourgeois et al. [1976]. In the systemic circulation, arterioles and small arteries contribute 75% of the total resistance, and the large arteries act as a capacitive reservoir [Berne and Levy, 1998]. Therefore, these investigators assumed that the arterial tree could be well represents by a two-element Windkessel model accounting for the lumped compliance of the large arteries (arterial compliance, AC) and the resistance of small arteries and arterioles (total peripheral resistance, TPR) as shown in Fig. 3.3a. They further assumed that TPR does not change within a diastolic interval since the autonomic nervous mechanisms responsible for modulating TPR are relatively slow [Berger et al., 1989b]. In addition, AC may be approximately constant over a wide pressure range and on the time scale of days to months [Hallock, 1937; Bourgeois et al., 1976]. Based on these assumptions, these investigators predicted that ABP may decay like a pure exponential during each diastolic interval with a time constant (τ) equal to the product of the TPR and AC (Fig. 3.2b). Thus, their pulse contour technique involved fitting a mono-exponential function to each ABP diastolic interval to measure τ and then dividing the time-averaged ABP with τ to compute the proportional CO scaled by a constant factor of 1/AC (Fig. 3.3b).

Bourgeois et al were able to successfully validate their technique with respect to central ABP waveforms measured near the heart, because the diastolic interval of these waveforms resembles an exponential decay (Fig. 3.4a). However, central ABP is rarely measured clinically because of the risk of blood clot formation and embolization. In contrast, in readily available peripheral ABP waveforms, an exponential diastolic decay

is not apparent (Fig. 3.4b). The reason is that the arterial tree is not simply a lumped system like the two-element Windkessel model suggests but rather a complicated distributed system with impedance mismatches, throughout due to vessel tapering, bifurcations, and caliber changes. The diastolic (and systolic) intervals of peripheral ABP waveforms are therefore corrupted by the complex wave propagation and reflections occurring at every site of impedance mismatch. Thus, the technique of Bourgeois et al cannot be applied to peripheral ABP waveforms.

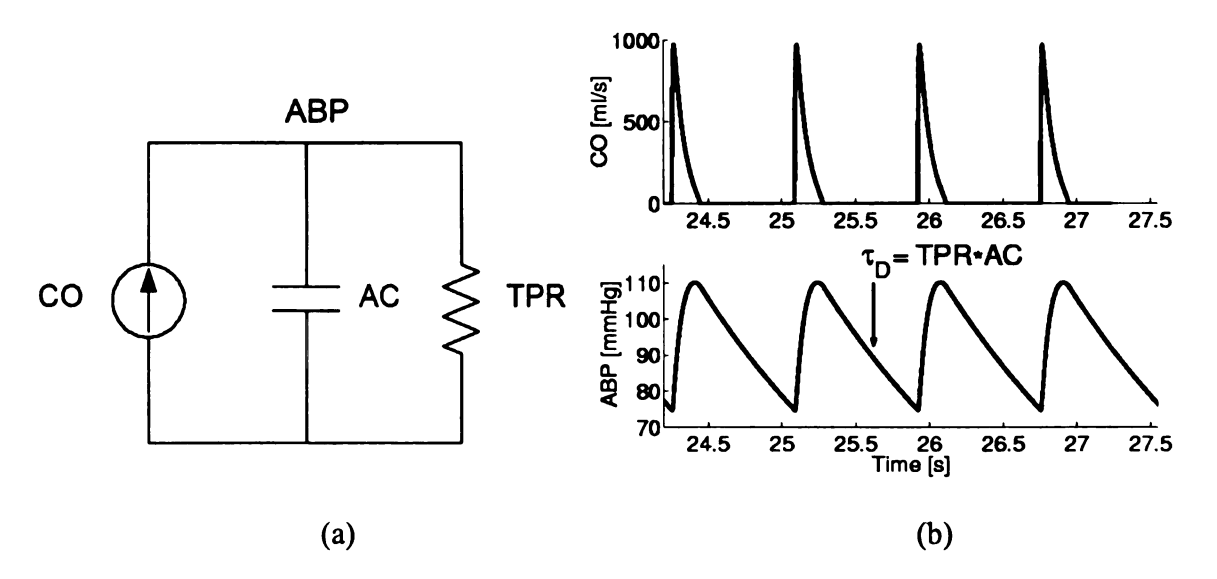


Figure 3.3 The technique of Bourgeois et al for monitoring CO from ABP waveform. (a), two-element Windkessel model of artery including total peripheral resistance (TPR) and arterial compliance (AC); (b), CO and ABP waveform. ABP decays like an exponential during diastole with a time constant (τ) equal to the product of TPR and the nearly constant AC. The proportional CO is calculated by dividing the mean ABP with τ [Bourgeois et al., 1976].

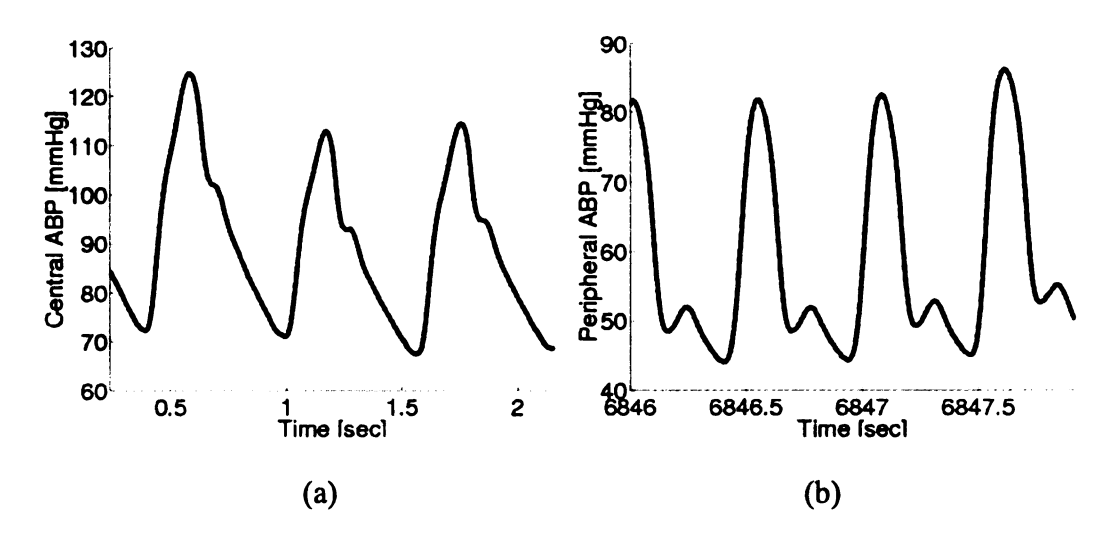
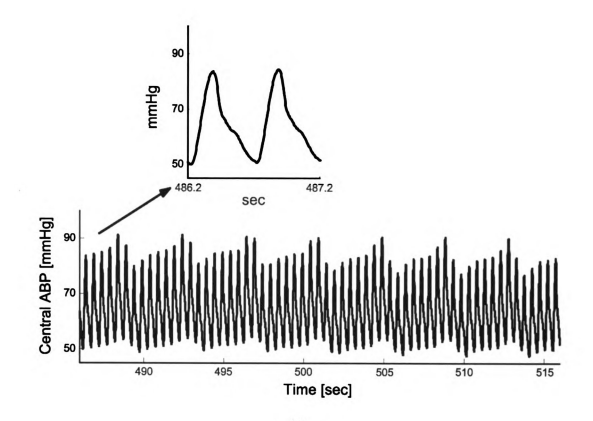


Figure 3.4 Comparison of central ABP measured in aorta (a) and peripheral ABP waveforms measured in radial artery (b). The diastolic intervals of the central ABP waveform resemble exponential decays; however, central ABP is rarely measured clinically. In contrast, exponential diastolic decays are not visible in the peripheral ABP waveforms, which are corrupted by complex wave reflections.

However, the two-element Windkessel model is a more valid representation of the long time scale dynamics of the systemic arterial tree. That is, according to transmission line theory, the confounding effects of complex waves in the arterial tree will diminish with increasing time scale [Noordergraaf, 1978]. That is, the wave effects significantly corrupt the peripheral ABP waveforms within a cardiac cycle (high frequencies) without complicating the waveforms over long time scales (low frequencies). This important concept is demonstrated in Fig. 3.5, which illustrates two ABP waveforms measured at the same time but at different sites in the arterial tree. The short time scale (within a beat)

variations are different in the two waveforms, as the characteristics of the complex wave effects differ at the two measurement sites. In contrast, the long time scale (beat-to-beat) variations are more similar, since the confounding effects of wave phenomena are less significant. (Note, the beat-to-beat variations are due to ongoing perturbations to the cardiovascular system (e.g., breathing), and the dynamic, compensatory response of the regulatory system (e.g., baroreflex)). Thus, the two-element Windkessel model is a more valid representation of the long time scale behavior of the arterial tree. This implies that if the pulsatile activity suddenly ceased, then a peripheral ABP waveform may eventually decay like a pure exponential as soon as the faster wave reflections vanish. Similarly, the peripheral ABP response to a single cardiac contraction would be corrupted in short time and would appear like a pure exponential decay in long time. In Fig. 3.6, the peripheral ABP waveform of an ICU patient is shown in the top panel, and the ABP responses to cardiac contractions, which are located at the beginning of each beat, are shown in the lower panels. The peripheral ABP waveform is actually the sum of ABP response to each cardiac contraction.



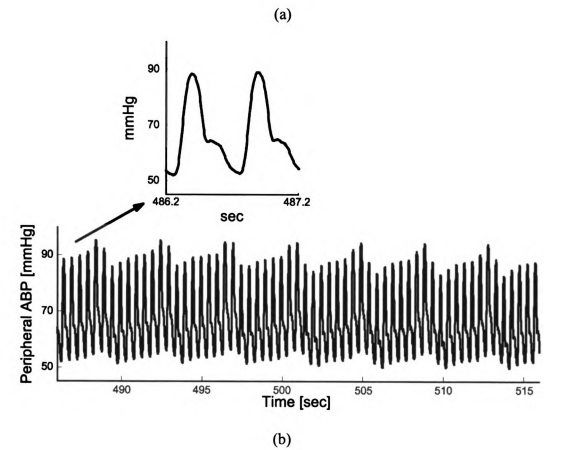
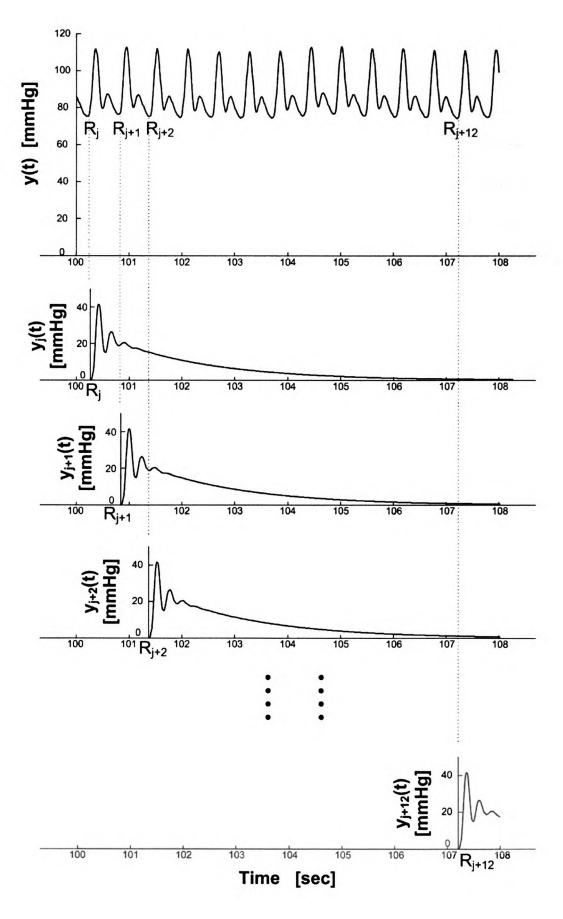


Figure 3.5 Two swine ABP waveforms measured at the same time but at different sites in the arterial tree. (a), ABP waveform measured centrally in the aorta; (b), ABP waveform measured peripherally in the radial artery. While the short time scale variations (top panels) differ due to highly complex wave motion, the long time scale variations (bottom panels) are more similar as the wave phenomena are only a high frequency effect.

Figure 3.6 ABP waveform (top panel) can be viewed as a sum of a group of blood pressure responses (lower panels) to cardiac contractions. y(t), arterial blood pressure; R_j , onset time of upstroke of No. j ABP wavelet; $y_j(t)$, blood pressure response located at R_j . In the short time (high frequency), $y_j(t)$ oscillates vigorously; while in the long time scale (low frequency), for example, longer than 2 sec, it decays like a pure exponential.



Therefore, our technique analyzes a peripheral ABP waveform over time scales greater than a cardiac cycle in order to determine the pure exponential decay in a peripheral ABP response (h(t)) to a single cardiac contraction after the wave reflection vanishes. In Fig. 3.6, in order to clearly illustrate the technique on a beat to beat basis, we only show an eight-second segment of the peripheral ABP waveform. In the analysis, we selected a time interval of about six-minute in order to provide enough beat to beat variability for system identification. One may think h(t) could be estimated by computing the nonparametric transfer function derived from power spectral of input and cross power spectral of input and output using Eq. 2.2. However, as we explained in Chapter 2, the circulatory mechanics cannot be obtained independently due to the existence of baroreflex feedback mechanism (Fig. 2.3). Therefore, we must use system identification to solely estimate the circulatory mechanics.

Fig. 3.7 illustrates the technique and indicates that the single contraction ABP response h(t) is determined in two steps. First, a signal representing the cardiac contractions (x(t)) is constructed from the ABP waveform based on a slightly modified impulse ejection model. That is, x(t) is formed as an impulse train in which each impulse is located at the onset of upstroke of an ABP pulse and has an area equal to the pulse pressure determined after lowpass filtering the waveform (with a cutoff frequency of 2 Hz) to attenuate the wave effects (FPP, filtered pulse pressure). Then, the impulse response function h(t) which when convolved with x(t) best fits the (unfiltered) ABP waveform (y(t)) in the least squares sense is estimated according to the following autoregressive exogenous (ARX) input equation:

$$y(t) = \sum_{k=1}^{m} a_k y(t-k) + \sum_{k=1}^{n} b_k x(t-k) + e(t), \qquad (3.1)$$

where e(t) is the unobserved residual error, the parameters $\{a_k b_k\}$ completely specify h(t), and m and n limit the number of these parameters (model order) [Ljung, 1999]. For a fixed model order, the parameters are closed form solution. The model order is determined by minimizing the Minimum Description Length (MDL) criterion introduced in Chapter 2. By definition, the estimated h(t) represents the (scaled) ABP response to a single, solitary cardiac contraction.

Next, τ is determined over the interval of h(t) ranging from two to four seconds after the time of its maximum value based on the following exponential equation:

$$h(t) = Ae^{-t/\tau} + w(t)$$
. (3.2)

(This time interval was established empirically by almost always observing a pure exponential decay in h(t) over this period in the hemodynamic data sets studied herein.) The parameters A and τ are estimated through the least squares minimization of the unmeasured residual error w(t). This optimization problem is solved in closed-form by log transformation of h(t) [Ljung, 1999]. In theory, accurate determination of the Windkessel time constant τ is achieved by virtue of h(t) coupling the long time scale or beat-to-beat variations in x(t) to y(t). That is, the technique is not just trivially extrapolating the ABP waveform at the end of diastole.

Finally, CO is computed to within a constant scale factor equal to 1/AC by dividing the time-averaged ABP with τ . Note that the above mathematical steps can easily be implemented in near real time with only a delay on order of a few seconds with a standard home PC.

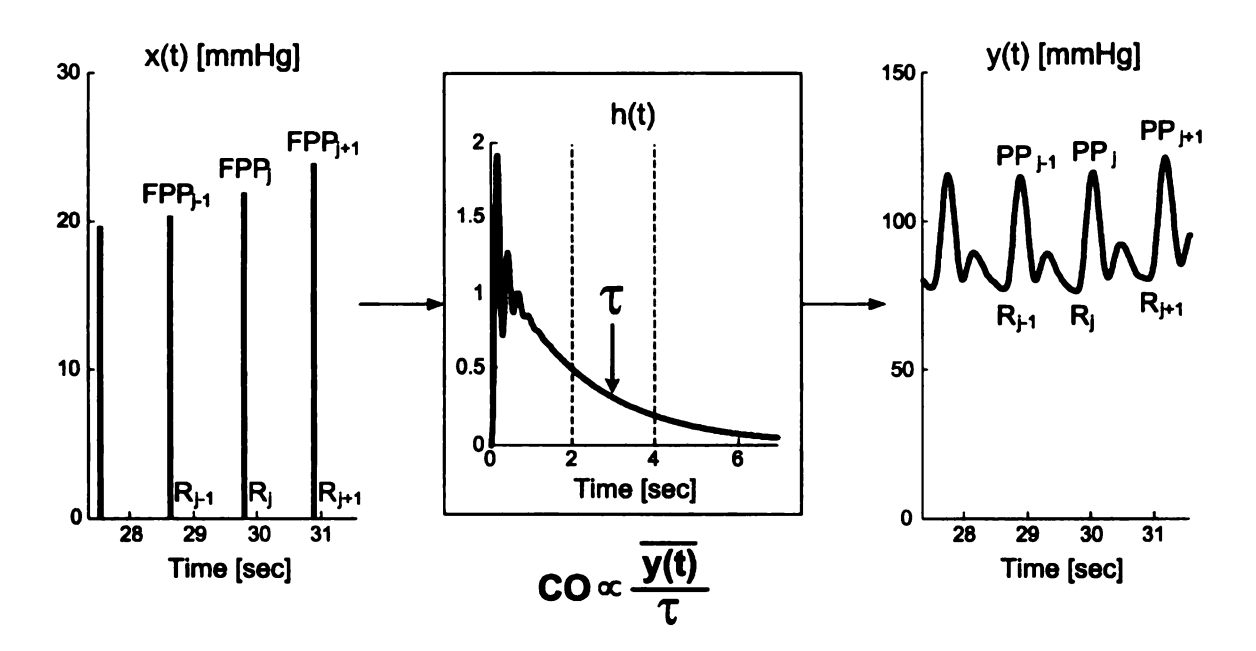


Figure 3.7 Illustration of identifying the time constant τ from a peripheral ABP waveform. FPP is pulse pressure of the filtered ABP (lowpass filter with cutting frequency of 2Hz); R, onset time of upstroke of each ABP wavelet; j, beat number; x(t), a constructed cardiac contractions signal; y(t), an ABP waveform; and h(t), an estimated impulse response coupling x(t) to y(t). Then proportional CO is ratio of mean y(t) to τ .

3.3 Technique Evaluation

To validate the technique, we applied it to invasive and non-invasive human data and compared the results with corresponding reference CO measurements.

3.3.1 Invasive ICU Patient Data

The hemodynamic data utilized to evaluate the mathematical analysis technique with respect to human invasive peripheral ABP waveforms were obtained from the MIMIC (Multi-parameter Intelligent Monitoring for Intensive Care) database, which is freely available from the PhysioNet website (www.physionet.org) and described in detail elsewhere [Moody et al., 1996, 2001]. Briefly, this database includes 72 ICU patient records, typically ranging from 24 to 48 hours in duration, which were archived from patient monitors in the medical, surgical, and cardiac ICUs of the hospital formerly known as the Beth Israel Hospital, Boston, MA. Each of these records consists of continuous waveforms sampled at 125 Hz such as invasive peripheral ABP via radial artery catheterization and surface ECG leads as well as one-minute trends such as thermodilution CO, mean ABP (MAP), and heart rate (HR). 16 of the 72 patient records were applicable to the present evaluation study, as they included radial ABP waveforms and multiple, reference thermodilution CO measurements. Within each of these records, CO was changing due to disease progression and therapy.

Based on these 16 MIMIC patient records, we created a data set for technique evaluation as follows. First, we downloaded from these records all of the distinct, one-minute thermodilution CO measurements and six-minute contiguous segments of the corresponding radial ABP waveforms (from 2.5 minutes preceding the one-minute CO

measurements to 2.5 minutes following these measurements). Then, we visually examined each of the radial ABP waveforms and extracted the longest contiguous, artifact-freed segment from each of these waveforms (see Discussion section). Finally, we excluded from the study all radial ABP waveforms that were less than 5 minutes in duration, had a significant linear trend (≥ 20 mmHg change), or represented the only waveform segment within a patient record (as the technique estimates changes in CO). A total of 101 pairs of simultaneous measurements of invasive radial ABP waveforms and reference thermodilution CO from 15 ICU patients [ten men and five women; age: 67 ± 12 yr (mean±SD)] remained for technique evaluation. Table 3.2 summarizes the clinical class and hemodynamic data for each of these patients.

3.3.2 Non-Invasive Human Experimental Data

The hemodynamic data utilized to evaluate the technique with respect to human non-invasive peripheral ABP waveforms were obtained from previous experiments designed to address different specific aims and are described in detail elsewhere [Elstad et al., 2001]. Here, we briefly present those aspects of the experiments that are relevant to the present study.

Ten healthy human volunteers [five men and five women, age: 25 ± 4 year (mean±SD)] participated in the experiments. Each subject was instrumented for non-invasive measurement of peripheral ABP, instantaneous CO, and other cardio-respiratory signals. The peripheral ABP waveform was measured with a finger-cuff PPG system (2300 Finapres Continuous Blood Pressure Monitor, Ohmeda; Englewood, CO), while instantaneous CO was measured according to a previously described Doppler ultrasound

technique [Eriksen et al., 1990] implemented by an expert. Specifically, aortic blood velocity was measured with a bi-directional ultrasound Doppler velocimeter (CFM-750, GE Vingmed; Horten, Norway), which was operated in pulsed mode at 2MHz with the hand-held transducer placed on the suprasternal notch. The area of the rigid aortic ring was determined in a separate session by parasternal sector-scanner imaging (CFM-750, GE Vingmed). Instantaneous CO was then calculated via the product of the measured instantaneous maximum blood velocity and the area of the aortic valve orifice.

Each instrumented subject was studied on two separate days before and after the administration of atropine (0.04 mg/kg) and/or propranolol (14.6 mg) under different postures to vary the experimental conditions. For each experimental condition, approximately six-minute intervals of the non-invasive measurements were continuously recorded at a sampling frequency of 50 Hz. In the present study, we specifically analyzed the digitized recordings from the following six experimental conditions: 1) supine, baseline, 2) supine, propranolol, 3) supine, propranolol+atropine, 4) 30° upright tilt, baseline, 5) 30° upright tilt, atropine, and 6) 30° upright tilt, atropine+propranolol. Based on these non-invasive recordings, we created a data set for technique evaluation following a similar procedure as the invasive study. First, we visually examined each non-invasive finger ABP waveform and instantaneous CO waveform and extracted the longest contiguous, artifact free segment from each waveform. Then, we excluded from the study the four instantaneous CO waveforms that were less than one minute in duration and the three finger ABP waveforms that were less than five minutes in duration or had unreasonably high-pressure values (see discussion). Finally, the reference CO value corresponding to each of the remaining instantaneous CO waveforms was

determined by computing its time-average. A total of 57 pairs of simultaneous measurements of artifact-free, non-invasive finger ABP waveforms and reference Doppler ultrasound CO values from the ten healthy subjects remained for technique evaluation. Table 3.3 summarizes the hemodynamic data for each of the subjects.

3.3.3 Data Analysis

Before applying the technique to the invasive radial ABP waveforms, we resampled ABP from 125Hz to 90Hz. In Eq. 3.1, we empirically chose the maxim orders m and n as 15. For the non-invasive finger ABP waveforms, we chose the maxim orders m and n as 10 due to the lower sampling frequency (50Hz).

After applying the mathematical analysis technique to all of the invasive and non-invasive peripheral ABP waveforms in the two human data sets, we quantitatively compared the resulting, proportional CO estimates with their reference, absolute CO values in each data set as follows. First, we scaled the proportional CO estimates to have the same mean value as the corresponding reference CO in each patient/subject. Then, we pooled the data together from all the patients/subjects in each data set and computed the root-mean-squared-normalized error (RMSNE) of the calibrated CO estimates (normalized by their reference CO values and given in percent) as a metric for comparison. (This metric indicates the ability of the technique to measure changes in CO from its mean value within an individual.) We also computed the correlation coefficient (p) between the pooled CO error and the corresponding CO, MAP, TPR, and HR values in each data set to determine the extent to which the hemodynamic conditions affected the performance of the technique.

3.4 Evaluation Results

Tables 3.2 and 3.3 respectively summarize the results of evaluating the mathematical analysis technique based on the invasive and non-invasive human hemodynamic data sets. These results indicate that the technique as applied to invasive radial ABP waveforms was in strong agreement with thermodilution measurements with an overall CO RMSNE of 15.3% in 15 ICU patients, while the technique as applied to non-invasive finger ABP waveforms was in equally strong agreement with Doppler ultrasound measurements made by an expert with an overall CO RMSNE of 15.1% in ten healthy subjects. Figs. 3.8 and 3.9 provide visual examples of the correspondence between the once calibrated CO estimates and their reference CO values in three individuals from each data set. Moreover, as indicated in the table captions, the CO error was only mildly correlated with MAP and even less correlated with CO, HR, and TPR.

Table 3.2: Summary of the intensive care unit patient records and CO estimation results of the invasive human hemodynamic data set. The technique was applied to 101 invasive radial ABP waveform segments from 15 patients achieved an overall CO root-mean-squared-normalized error (RMSNE) of 15.3% with respect to reference thermodilution measurements. Moreover, the CO error here was essentially uncorrelated with CO (ρ =-0.14) and heart rate (HR; ρ =0.04) and only mildly correlated with mean ABP (MAP; ρ =0.41) and TPR (ρ =0.38).

PATIENT RECORD	CLINICAL CLASS	OF COMPA- RISONS	CO RANGE [L/MIN]	MAP RANGE [MMHG]	TPR RANGE [PRU]	HR RANGE [BPM]	CO RMSNE [%]
041	Bleed	2	8.5-9.5	74-81	0.5-0.6	78-104	0.5
055	Resp. failure	7	3.9-5.2	78-106	0.9-1.4	88-106	6.9
281	NA	4	3.7-4.9	94-99	1.2-1.6	100-114	6.8
410	Sepsis	7	4.3-9.4	74-97	0.6-1.1	60-94	22.3
411	Resp. failure	6	3.2-4.6	84-94	1.2-1.7	50-61	14.4
451	CHF	5	4.1-5.8	51-58	0.5-0.9	74-84	15.0
453	Post-op valve	12	3.4-4.8	60-79	0.9-1.3	50-89	10.7
454	Post-op valve	5	3.7-4.8	67-74	0.9-1.1	49-70	5.4
456	Post-op CABG	8	3.8-8.5	57-100	0.6-1.0	67-108	22.5
474	NA	5	3.8-4.4	72-79	1.1-1.2	86-94	15.6
476	Post-op CABG	6	4.2-4.6	58-71	0.8-0.9	90-105	11.2
477	Post-op CABG	6	4.5-6	54-75	0.6-0.8	79-111	10.6
480	Post-op CABG	6	5-6.7	63-75	0.6-0.8	85-112	11.1
484	NA	9	5.1-7.5	62-78	0.6-0.8	79-96	12.4
485	NA	13	2.9-4.7	69-87	1.0-1.8	94-126	23.0
TOTAL		101	2.9-9.5	51-106	0.5-1.8	49-126	15.3

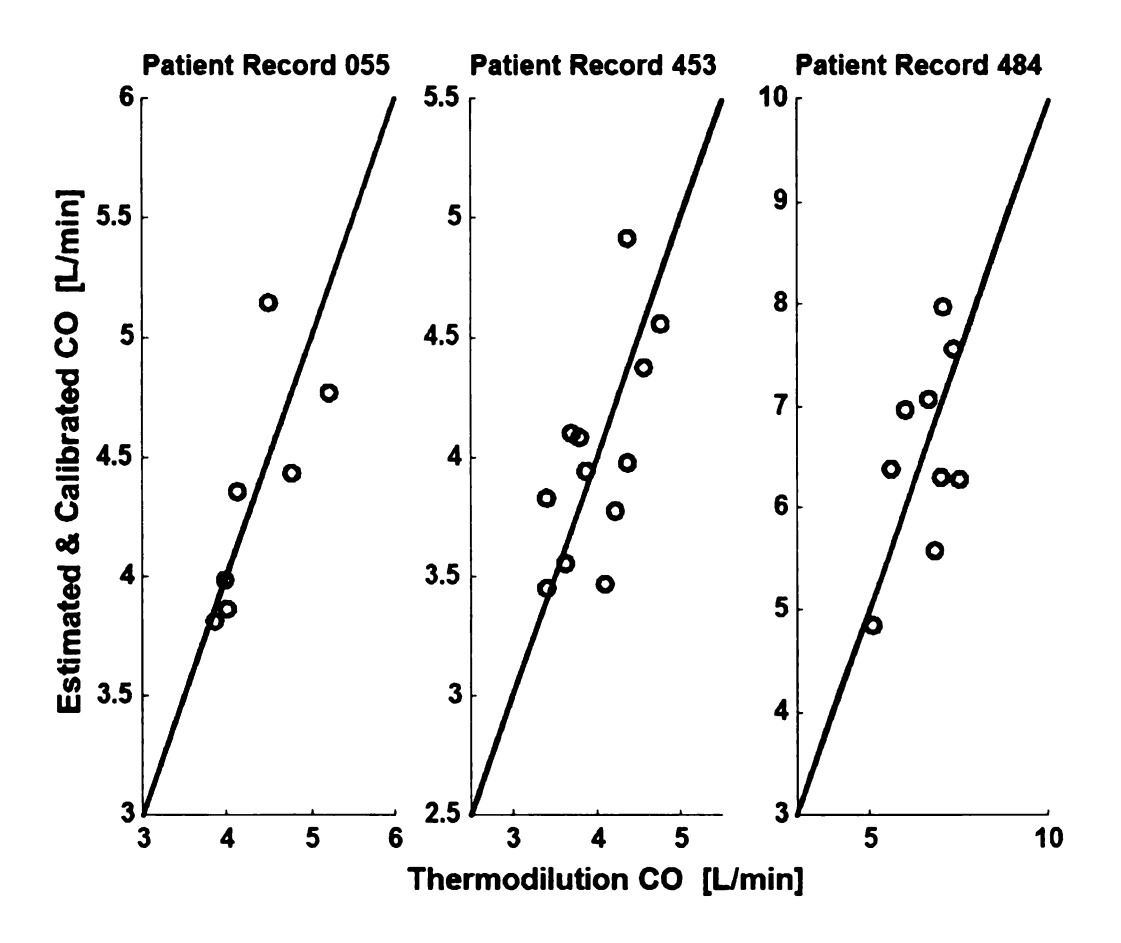


Figure 3.8 Visual examples of CO estimation results in three intensive care unit (ICU) patients. For each patient, the estimated and calibrated CO is plotted against corresponding thermodilution measurement.

Table 3.3: Summary of the healthy young adult records and CO estimation results of the non-invasive human hemodynamic data set. The technique was applied to 57 non-invasive finger ABP waveform segments from ten healthy young adults achieved an overall CO root-mean-squared-normalized error (RMSNE) of 15.1% with respect to reference Doppler ultrasound measurements made by an expert. Moreover, the CO error here was essentially uncorrelated with CO (ρ =-0.17), TPR (ρ =0.10) and heart rate (HR; ρ =0.19) and only mildly correlated with mean ABP (MAP; ρ =0.37).

SUBJECT	NUMBER OF	СО	MAP	TPR	HR	СО
		RANGE	RANGE	RANGE	RANGE	RMSNE
RECORD	COMPARISONS	[L/MIN]	[MMHG]	[PRU]	[BPM]	[%]
LD	5	3.6-6.8	82-128	1.0-1.9	43-108	13.0
WP	6	4.3-6.3	68-93	0.7-1.1	60-113	16.9
CG	6	4.5-7.7	75-118	0.9-1.3	48-98	20.2
JE	6	4.5-8.2	85-125	0.9-1.4	51-135	14.6
AE	6	3.5-5.3	79-124	1.2-1.5	32-72	18.3
DL	4	3.5-4.7	92-104	1.2-1.9	60-88	14.8
GB	6	4.6-7.2	65-83	0.6-1.0	56-126	13.3
LB	6	4.3-7.1	70-95	0.8-1.1	47-100	9.0
MR	6	4.4-6.8	75-102	0.8-1.2	50-115	12.1
NB	6	3.7-8.4	72-116	0.8-1.5	48-99	15.3
TOTAL	57	3.5-8.4	65-128	0.6-1.9	32-135	15.1

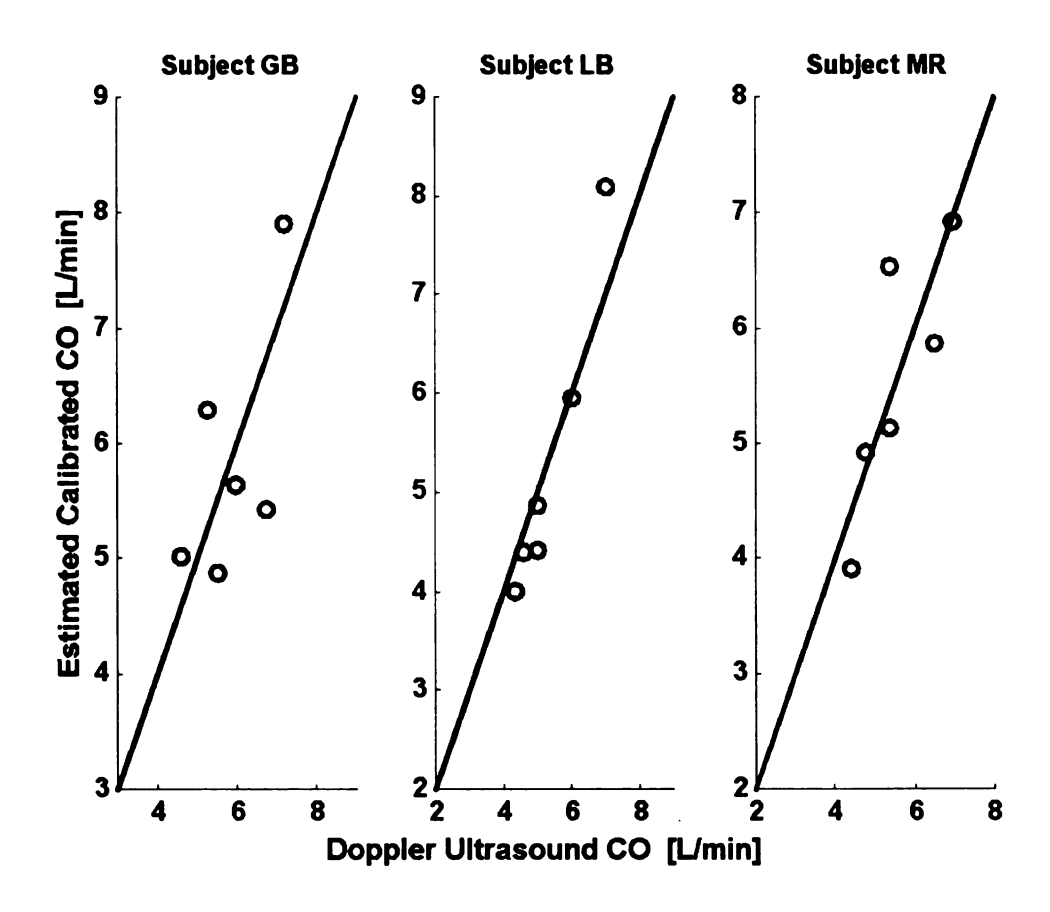


Figure 3.9 Visual examples of CO estimation in three healthy subjects. For each patient, the estimated and calibrated CO is plotted against corresponding Doppler ultrasound measurement.

3.5 Discussion

In summary, we improved and further evaluated a previously developed CO monitoring technique from a peripheral ABP waveform. The uniqueness of the technique lies in the analysis of the peripheral ABP waveform over long time scales in which the confounding effects of wave phenomena are attenuated. Here, to better reduce the short-term reflection effect on the system identification, the pulse train representing the cardiac

contractions (input of the system identification) was weighted by the pulse pressure of the filtered ABP waveform; while in our previous technique, the pulse train was weighted simply by the pulse pressure of the original ABP waveform. We evaluated the technique in humans based on previously published invasive and non-invasive hemodynamic data sets. With the former data set, we compared the application of the technique to invasive radial ABP waveforms with reference thermodilution measurements in 15 ICU patients in which CO was changing due to disease progression and therapy. With the latter data set, we compared the application of the technique to non-invasive finger ABP waveforms with reference Doppler ultrasound measurements made by an expert in 10 healthy subjects during pharmacological and postural interventions. We report an overall CO estimation error of about 15% with respect to each of these human data sets (see Tables 3.2 and 3.3 and Figs. 3.8 and 3.9). Although the evaluations described herein were retrospective, it is noteworthy that neither of these data sets was designed for the evaluation of our technique or any other pulse contour analysis technique.

3.5.1 Potential Sources of CO Error

The CO errors reported here could be partly explained by inadequacies in the quality and accuracy of the hemodynamic measurements within the studied invasive and non-invasive data sets. However, as described below, we excluded from the study all data segments of poor quality (e.g., corrupted by significant noise artifact) so as to benchmark technique performance. On the other hand, nothing could be done in this retrospective study to improve upon the accuracy of the measurements, which is largely intrinsic to the employed transducers.

The radial ABP waveforms in the invasive data set were measured with generally accurate, intra-arterial catheters. However, in the MIMIC database upon which this data set was based, ABP waveform artifact was sometimes present. The artifact may have been due to, for example, patient movement, arterial line flushing, catheter obstruction, loss of signal, and proximal ABP cuff inflation. We excluded from the study all radial ABP waveforms that were significantly corrupted by such artifact (~11% of the available, simultaneous pairs of radial ABP waveforms and thermodilution measurements). While we identified ABP artifact here by visual means, it may be possible to automatically and reliably detect ABP artifact in real time (e.g., with a simultaneous surface ECG measurement based on an algorithm recently introduced by Zong et al. [2004]) so as to warn the clinician that the CO estimate derived from the ABP analysis may not be valid or preclude the output of such a CO estimate. Note that, for reasons described above, we also excluded from the study all radial ABP waveforms with linear trends of ≥20 mmHg (~13% of the available, simultaneous pairs of radial ABP waveforms and thermodilution measurements).

In contrast to the radial ABP waveforms in the invasive data set, it was not possible to assess the quality of the corresponding thermodilution measurements.

However, the error in clinical thermodilution measurements is known to be in the 15-20% range [Levett et al., 1979; Stetz et al., 1982]. Assuming such an error, Critchley et al. argued that a new CO measurement method should be accepted as an alternative to thermodilution provided that their limits of agreements are within ±30% [1999]. We note that the level of agreement between our technique and thermodilution measurements from 15 ICU patients is essentially in this range (see Table 3.2 and Fig. 3.8).

The non-invasive hemodynamic data utilized in this study were obtained from controlled experiments, and none of the non-invasive finger ABP waveforms were excluded from the study due to noise artifact. However, two non-invasive finger ABP waveforms were excluded from the study because of unreasonably high-pressure levels. This artifact may have been due to an upward drift in finger ABP caused by prolonged application of cuff pressure [Ristuccia et al., 1997]. Note that this finger-cuff photoplethysmography artifact may be attenuated or eliminated by intermittent finger exercise [Ristuccia et al., 1997] or with the currently available Portrapres system, which alternates the application of cuff pressure between different fingers.

Although artifact in the non-invasive finger ABP waveforms was not a significant factor here, the intrinsic level of accuracy of the employed Finapres system may have affected our results. In a review of Finapres technology, Imholz et al. gathered 43 previous studies comparing the Finapres system with intra-arterial or non-invasive, discrete ABP measurements and reported that the systolic and mean pressure levels of the Finapres system were not within the limits of accuracy suggested by the American Association for the Advancement of Medical Instruments [Imholz et al., 1998]. On the other hand, Omboni et al. showed that the Finapres system and radial artery catheterization produce similar beat-to-beat (mean) ABP fluctuations [Omboni et al., 1993]. That is, while the Finapres system distorts the peripheral ABP waveform over short time scales, it may have little effect on the waveform over longer time scales. Thus, since the technique analyzes the ABP waveform over long time intervals, the inherent inaccuracies of the Finapres system may not have been a major contributor to the CO

error reported herein. However, we cannot confirm this possibility, because simultaneous intra-arterial ABP recordings were not available.

The reference Doppler ultrasound measurements in the non-invasive data set were made by an expert, and only four of these CO measurements were excluded from the study due to poor signal quality. Despite the generally excellent signal quality, the assumptions underlying the Doppler ultrasound technique could have been partially violated thereby affecting our results. These assumptions include the following: 1) the velocity profile in the aortic valve orifice is rectangular and this velocity is conserved as the central maximum velocity of a jet 3-4 cm downstream; 2) the insonication angle is 20°; and 3) the aortic valve is circular [Eriksen and Walloe, 1990]. However, these assumptions are likely to have little effect on the accuracy of the measured relative changes in CO. Since our technique is designed to measure relative changes in CO and we evaluated it here as such (see Statistical Analysis section), we believe that the Doppler ultrasound measurements serve as a reasonably accurate reference here (i.e., at least as accurate as standard thermodilution measurements).

Other potential sources of the CO errors reported here are any violations to the assumptions upon which the technique is based. These assumptions include the following: 1) AC is constant within each individual; 2) peripheral venous pressure is negligible with respect to ABP; 3) ABP exceeds the critical closing pressure; and 4) the time constant governing arterial viscoelastic effects is negligible with respect to the Windkessel time constant [Mukkamala et al., 2006]. The first of these assumptions is perhaps the most controversial, since there is currently no generally accepted, gold standard method for measuring in vivo AC. Nevertheless, we believe that in vivo AC

53

must be nearly constant over a wide hemodynamic range in at least some animals based on the success of the pulse contour analysis of Bourgeois et al. and Osborn et al. with respect to canine central ABP waveforms [Bourgeois et al., 1974; Osborn et al., 1968] and the present mathematical analysis technique with respect to swine peripheral ABP waveforms [Mukkamala et al., 2006]. We are unaware of any existing in vivo data likewise demonstrating constancy of the human AC. However, Hallock and Benson did show that, although the compliance of excised human aortas of various ages at autopsy (ranging from young adults to the elderly) decreased with increasing pressure, in vitro aortic compliance could be approximated as constant over a wide pressure range [Hallock and Benson, 1937]. If in vivo AC sharply changed in the opposite direction of MAP within each individual record of our study, then our technique would have grossly overestimated CO at high MAP levels and underestimated CO at low MAP levels (i.e., a strong, positive correlation between CO error and MAP). Although the correlation between CO error and MAP is positive, the degree of correlation is mild (see above), suggesting that in vivo AC within each of the 15 ICU patient and ten healthy young adult records may have been approximately constant.

3.5.2 Comparison to Intra-Beat Pulse Contour Analysis Techniques

In a previous paper introducing our mathematical analysis technique [Mukkamala et al., 2006], we used signal-to-noise theory to argue that estimating the average Windkessel time constant τ (and thus average, proportional CO via Ohm's law) by analyzing a peripheral ABP waveform over time intervals greater than a cardiac cycle should be more accurate than analyzing the ABP waveform over individual cardiac cycles and then

averaging the beat-to-beat results. To support this theoretical argument, we fitted complex exponentials function(s) to individual diastolic decay intervals of swine peripheral ABP waveforms to estimate τ on a beat-to-beat basis, averaged the resulting individual τ estimates, and then computed average, proportional CO via Ohm's law. The best result we were able to achieve with this intra-beat analysis was an overall CO RMSNE that was 52% larger than that obtained by our technique. We repeated this intrabeat analysis with respect to the human invasive and non-invasive hemodynamic data sets here and obtained overall CO RMSNEs that were respectively 23% and 81% higher than those obtained by our technique. (Note that one possible reason that this intra-beat analysis is much less effective with respect to the non-invasive hemodynamic data set is that, as described above, the non-invasive ABP waveforms may suffer from high frequency distortion due to the employed Finapres system). We believe that these comparative studies confirm the theory that important information is indeed present in beat-to-beat ABP variations and that analysis of these subtle variations leads to improved average, proportional CO estimation in practice. However, we note that future studies should also be conducted to compare our technique with the recent intra-beat techniques of [Wesseling et al., 1993] and [Linton et al., 2001], which also require a single peripheral ABP waveform for analysis.

3.5.3 Limitations of the Long Time Interval Analysis Techniques

Two limitations of the current form of the long time interval analysis technique are:

1) beat-to-beat CO monitoring is not feasible and 2) artifact is a more significant problem

(as compared to beat-to-beat pulse contour analysis techniques such as the

aforementioned). With respect to the former limitation, we feel that attempts to improve the accuracy of average, proportional CO estimation, even at the cost of temporal resolution, are worthwhile from a clinical point of view. For example, although many previous pulse contour analysis techniques can offer beat-to-beat proportional CO monitoring, they have still not been widely adopted in clinical practice presumably due to accuracy concerns. Moreover, automatic estimation of proportional CO at intervals on the order of seconds but representing the last six-minutes (i.e., boxcar moving average) would represent a significant improvement upon discrete, operator-required determinations of CO by the clinical thermodilution method (assuming similar accuracy). With respect to the second limitation, the requirement of approximately six-minute intervals of relatively artifact-free ABP waveforms does not substantially limit the practical applicability of the technique. For example, only ~11% of the invasive radial ABP waveforms from the real world MIMIC database were discarded in our study due to artifact. Moreover, the six-minute intervals of analysis may be reduced to smaller intervals (e.g., one minute) without materially affecting the accuracy of the estimates (e.g., CO RMSNE of 15.1% in the invasive hemodynamic data set and 15.7% in the noninvasive hemodynamic data set). Future formal studies are needed to determine the minimum interval for analysis that does not significantly compromise the accuracy of the technique.

3.5.4 Limitations of the Human Evaluation Study

In the invasive hemodynamic data set, CO was naturally changing within each ICU patient record due to disease progression and therapy. Typical ICU therapy is known to

include medications such as dobutamine, dopamine, intravenous fluids, and nitroprusside (i.e., both cardiac and vascular interventions) [Marino, 1998]. However, since timestamped annotations were not available here, we were not able to evaluate the technique in the ICU patients with respect to each of these common therapeutic interventions. In contrast, in the non-invasive hemodynamic data set, CO was changing in each healthy subject due to precisely known interventions of atropine, propranolol, and/or a 30° upright shift in posture. As described above, the CO RMSNEs were largest during the double blockade conditions, presumably because beat-to-beat HR variability was totally abolished. While vascular changes (TPR and fluid shifts) occurred reflexively upon administration of atropine and propranolol as well as via the postural shift (see Table 2), we were not able to test the technique with respect to non-invasive ABP waveforms during interventions that directly act on the vasculature (e.g., phenylephrine, nitroprusside). Finally, since the reference thermodilution CO in the invasive hemodynamic data set could not be assumed to be valid during unsteady conditions (e.g., ABP waveform segments with significant trends) and the non-invasive ABP waveforms were only recorded during steady conditions (see above), we were not able to evaluate the technique in humans during unsteady conditions (i.e., rapid changes in CO). However, we have previously shown that the technique performs quite accurately during unsteady conditions in swine instrumented with aortic flow probes measuring instantaneous flow [Mukkamala et al., 2006]. Moreover, in the present human study, we were at least able to show that the technique performed approximately the same regardless of the size or direction of the CO change, as the correlations between the CO error and $\triangle CO$ and $|\triangle CO|$ were only mild (see above).

3.5.5 Potential Applications of the Mathematical Analysis Technique

Our technique mathematically analyzes a single peripheral ABP waveform over long time intervals in order to continuously (i.e., automatically and without the need for an operator) measure CO to within a constant scale factor. The technique may therefore be utilized to quantitatively monitor relative changes in CO. The proportional CO may be calibrated, if desired, with a single, absolute CO measurement (e.g., thermodilution). For normal individuals, it may be possible to determine the proportionality constant from a nomogram. However, we believe determination of the proportionality constant is unnecessary in the context of continuous monitoring in the acute setting in which only CO changes are clinically relevant.

The results of this retrospective human evaluation study indicate that the technique may be sufficiently accurate in terms of estimating relative changes in CO with respect to invasive radial ABP waveforms from critically ill patients and non-invasive finger ABP waveforms from healthy subjects. With further mathematical analysis development (including the incorporation of an automated artifact detector) and successful prospective testing, the technique may potentially be applied to continuously monitor CO in the acute setting. The most prominent such application is in critically ill patients in the ICU and operating and recovery rooms. In critically ill patients instrumented with both pulmonary and radial artery catheters, the technique could be calibrated with a single thermodilution measurement to permit subsequent continuous monitoring of absolute CO. In the numerous critically ill patients with only radial artery catheters installed (see above), the technique could provide continuous, quantitative monitoring of relative changes in CO. Other such applications in which non-invasive peripheral ABP transducers would be

most appropriate include patients in the emergency room and the hospital ward, trauma patients in transport, as well as soldiers in combat. The human evaluation study described herein represents an initial step towards the realization of such applications.

CHAPTER 4

CONTINUOUS MONITORING OF CARDIAC OUTPUT AND LEFT ATRIAL PRESSURE FROM A PULMONARY ARTERY PRESSURE OR RIGHT VENTRICULAR PRESSURE WAVEFORM

4.1 Background

Left atrial pressure (LAP) generally indicates the blood pressure attained in the left ventricle during the cardiac filling phase. LAP can be utilized together with CO to distinguish the two types of cardiovascular diseases. When both CO and LAP decrease over time period, the disease should be circulatory problem such as hemorrhage; while when CO decreases and LAP increases, the disease should be a cardiac problem due to, for example, a heart attack. In the ICU, LAP is approximated with the pulmonary capillary wedge pressure (PCWP), which is also known as the pulmonary artery wedge pressure (PAWP) or the pulmonary artery occlusion pressure (PAOP). In order to measure PCWP, a pulmonary artery catheter (PAC, see Chapter 3) is wedged in a branch of the pulmonary artery and then a balloon is inflated at the tip of the catheter [Swan et al., 1970]. The resulting non-pulsatile pressure tracing is the PCWP (Fig. 4.1). Under the proper circumstances that a static column is created between the PAC tip and the left atrium, this pressure approximately reflects the mean LAP. This approximation is correct only if the PAC tip is in the proper lung zone and no vascular obstruction, such as pulmonary vein stenosis, occurs downstream. In fact, the measurement of PCWP is associated with a high incidence of technical problems due to partial wedging, over

inflation of the balloon, lack of fluid column continuity between the transducer and the vascular lumen, and etc [Morris et al., 1984]. Moreover, recent researches has indicated that the inadequate knowledge of physicians (and nurses) in using this technique might lead to incorrect interpretation of PCWP [Marik et al., 1998]. Even if the PCWP measurement is proper, it can only be obtained every few hours, as it requires an operator to inflate the balloon. Therefore, PCWP has been criticized due to the apparent failure to demonstrate improvements in patient outcome and risks associated with its use for a long time [Pinsky and Vincent, 2005].

As a result, physicians may resort to, for example, crude estimates of LAP through pulmonary artery diastolic pressure (PADP) in order to obtain immediate feedback about patient status. Although LAP may be measured continuously by direct catheterization of the left heart, this procedure is too invasive and risky for clinical use. A few non-invasive methods have been suggested for estimating LAP through physical signs, cardiac imaging, and the Valsalva maneuver [McIntyre et al., 1992]. However, these methods are evidently insensitive and inaccurate [Chakko et al., 1991; Diamond et al., 1993; Stevenson et al., 1989]. Moreover, each of these methods can only provide discrete estimates of LAP. Although the empirical techniques have been developed to monitor LAP using Doppler ultrasound [Nishimura and Tajik, 1997; Dokainish et al., 2004], they are proved to be not accuracy. A clinically usable technique for continuous LAP monitoring is therefore needed to permit more optimal therapy.

In fact, with the PAC, pulmonary artery pressure (PAP), right atrial pressure and right ventricular pressure (RVP) can be measured reliably and continuously (i.e., autonomous operation) via fluid-filled systems attached to external pressure transducers.

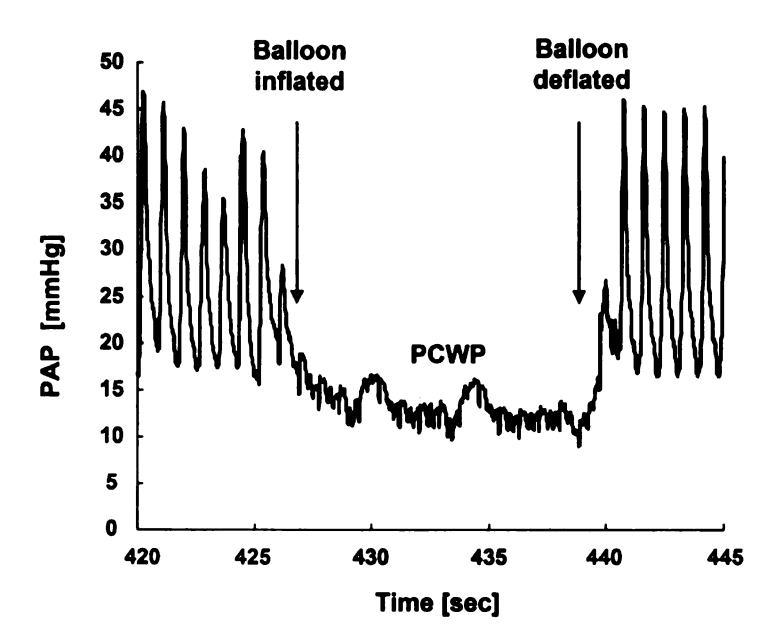


Figure 4.1 Illustration of pulmonary capillary wedge pressure (PCWP) measurement.

PCWP is obtained by inserting pulmonary artery catheter into pulmonary artery, and inflating its balloon at a branch of artery to occlude blood flow.

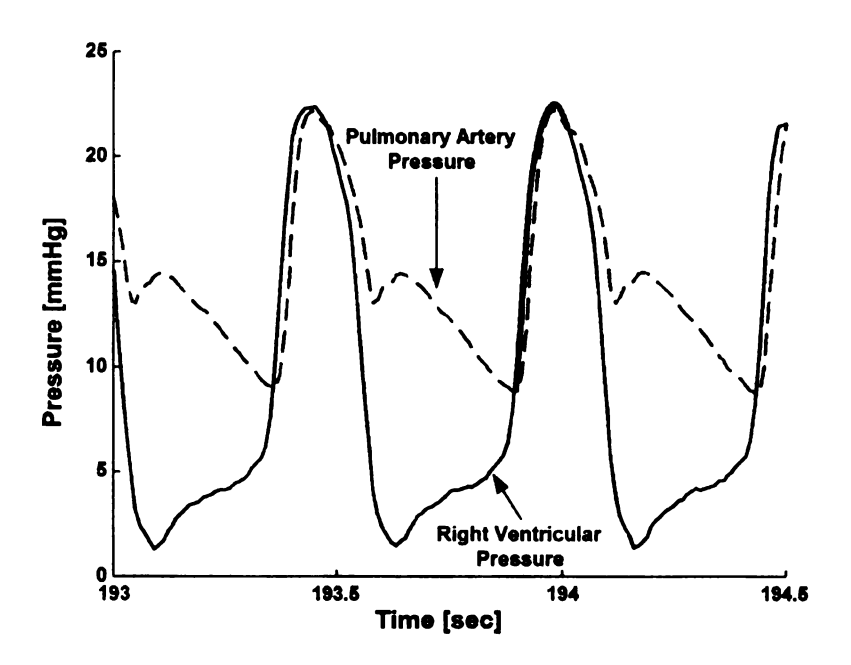


Figure 4.2 Illustration of construction of pulmonary artery pressure (PAP) from right ventricular pressure (RVP) during ejection phase. Thin line, RVP; dash line, actual PAP; thick line, RVP during ejection phase, which is used as a surrogate of PAP.

If PAP or other pressure measurements could be utilized to monitor LAP as well as CO, this continuous monitoring technique could help doctors to, for example, assess the effects of fluid and pharmaceutical interventions and be quickly altered to possible complications. A few intra-beat techniques to monitor CO from PAP waveform (e.g., [Tajimi et al., 1983]). But these techniques faced the similar difficulty as technique monitoring CO from peripheral ABP: distortion caused by the complex vascular structure and mechanical character. Moreover, to our knowledge, no technique has yet been developed to continuously monitor both CO and LAP from a PAP waveform. In Chapter 3, we have introduced a minimally invasive or non-invasive technique for continuously monitoring CO changes from a single peripheral ABP waveform. Here, we extend the technique in order to monitor CO and LAP simultaneously from a single PAP waveform.

We can further extend the technique to RVP. The implanted devices, such as two-lead pacemaker, can measure both LAP and RVP. Similarly to LVP and ABP (Fig. 2.4), during the ejection period of the right ventricle, RVP and PAP waveforms are almost overlapped as shown in Fig. 4.2 provided there is no stenosis of the pulmonary valve. Thus, the PAP waveform during the ejection period may be approximated by the RVP waveform and therefore the technique for estimating CO and LAP from PAP may be extended to RVP.

4.2 Monitoring of CO and LAP from PAP

4.2.1 The Technique

Unlike the systemic arterial tree, pulmonary circulation is a low resistance system with high bifurcation. In a person breathing normally, the alveolar wall capillaries

contribute up to 40% of the total resistance, the arteries about 50%, and the veins about 10% [Berne and Levy, 1998]. Pulmonary capillaries also contribute a large fraction of the total pulmonary vessel compliance. These properties result in more serious wave reflections (Fig. 4.3a). In addition, unlike right atrial pressure, LAP is a significant fraction of PAP due to the low resistance of the pulmonary microcirculation. Despite these complications, we assume the simple two-element Windkessel model (Fig. 4.3b) is a valid representation of the behavior of pulmonary circulation over long time scales greater than one cardiac cycle. Here, pulmonary vessel compliance (PVC) consists of the compliances of all vessels (arteries, capillaries and veins), and pulmonary vessel resistance (PVR) consists of the resistances of all vessels. We also assume that PVC is a constant.

Thus, we have extended the technique in Chapter 3 to also account for the contribution of LAP to PAP. The technique analyzes a PAP waveform over long time intervals in order to determine the pure exponential decay to LAP that would eventually result once pulsatile activity abruptly ceased. More specifically, the extension is to estimate both the average LAP and the response of PAP-LAP to a single cardiac contraction. Fig. 4.4 illustrates the technique, which is applied to a PAP waveform of duration of approximately 6 minutes. This technique is employed analogously to the technique in Chapter 3, except that the contributions of both a cardiac contractions signal (x(t)) and average LAP to the PAP waveform (y(t)) are incorporated.

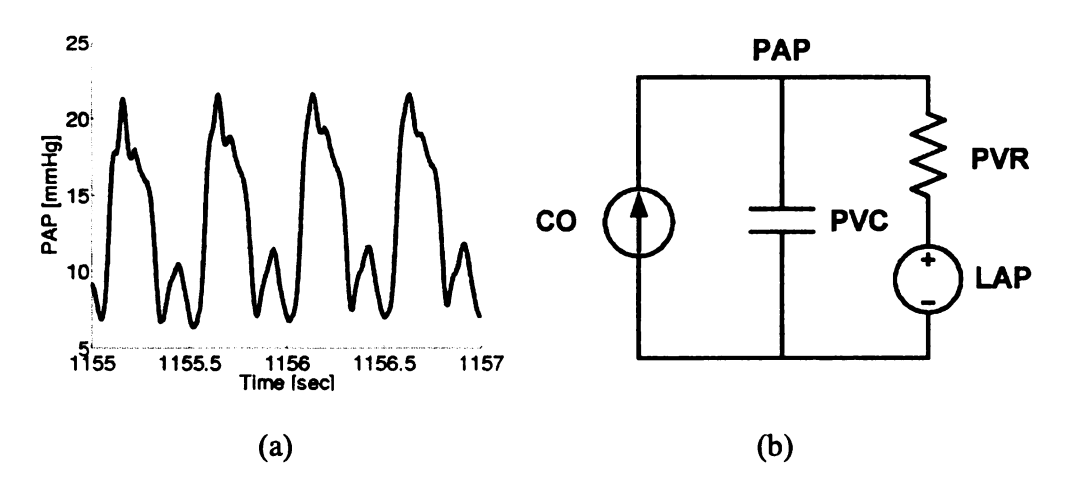


Figure 4.3 PAP waveform (a) and pulmonary circulation Windkessel model (b). PVC, pulmonary vessel compliance; PVR, pulmonary vessel resistance; CO, cardiac output; LAP, left atrial pressure.

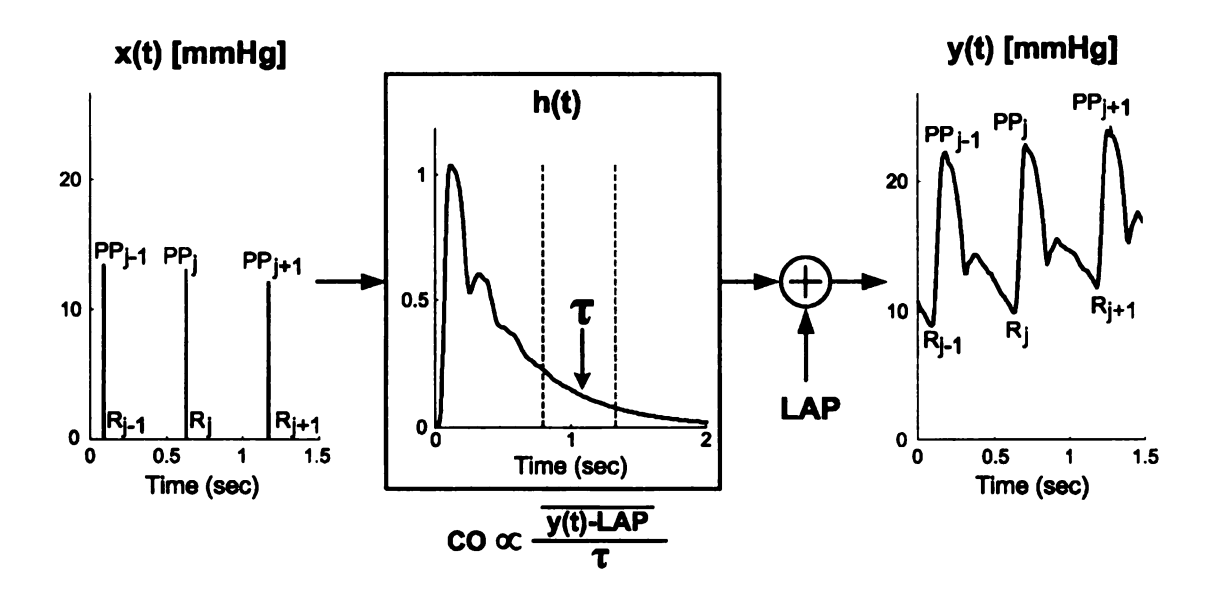


Figure 4.4 Illustration of identifying the time constant τ and LAP from a pulmonary PAP waveform. PP is pulse pressure; R, onset time of upstroke of each PAP wavelet; j, beat number; x(t), a constructed cardiac contractions signal; y(t), an PAP waveform; and h(t), an estimated impulse response coupling x(t) to y(t). Then proportional CO is ratio of mean PAP (MPAP)-LAP to τ .

First, a cardiac contractions signal is constructed by formation of an impulse train.

Each impulse is located at the R-wave of a simultaneous surface electrocardiogram

(ECG) measurement and has unity area.

Second, the PAP waveform segment (y(t)) is fitted according to the sum of an unknown constant term and the convolution between an unknown impulse response (h(t)) and the constructed cardiac contractions signal (x(t)). That is, the constant term and h(t) are estimated so as to permit the best fit or prediction of y(t) in the least squares sense. The estimated constant term represents the average LAP, while the estimated h(t) is defined to represent the PAP-LAP response to a single cardiac contraction. The impulse response h(t) and average LAP are specifically estimated with the following autoregressive exogenous (ARX) input equation with constant term c:

$$y(t) = c + \sum_{k=1}^{m} a_k y(t-k) + \sum_{k=1}^{n} b_k x(t-k) + e(t), \qquad (4.1)$$

where e(t) is the unmeasured residual error, $\{a_k, b_k\}$ are unknown parameters, and m and n limit the number of these parameters (model order) [Ljung, 1999]. For a fixed model order, the parameters including c are estimated from x(t) and y(t) through the least-squares minimization of e(t), which has a closed-form solution [Ljung, 1999]. With the estimated parameters, average LAP is computed as follows:

LAP =
$$\frac{\hat{c}}{1 - \sum_{k=1}^{m} \hat{a}_{k}}$$
, (4.2)

where ^ indicates estimates.

Next, τ is computed similarly as in Chapter 3. Finally, proportional CO may be computed by dividing the time-averaged PAP-LAP with τ and calibrated with thermodilution measurements.

We developed a new model order selection algorithm. Basically, we search the best model order from a set of candidate orders within a pre-defined range by analyzing the relationship between the mean square error (MSE) of the estimation and the model order. The estimation MSE is equal to $||e||^2/N$, where e is the residual error in Eq. 4.1, N is the length of the signals. As described in Chapter 2, the estimation MSE is a monotonically decreasing function of model order, while the decreasing speed of MSE becomes slower as the model order increases. Importantly, at a certain model order (*knee*), the decreasing speed dramatically becomes very slower. We regard this model order as the true model order. This model order selection criterion is based on the fact that initially the MSE decrease is caused by minimizing the estimation error due to the incompleteness of the estimation model; while after the model order is greater than the true model order, the MSE decrease is caused by minimizing the estimation error due to the noise.

Specifically, the best order is obtained as follows (Fig. 4.5). First we plotted the estimation MSE= $||e||^2/N$ against the model order (r). Next, for each order r, we fit the curve with two straight lines intercepted at the point (r,P_r) . The slopes of the two lines and the value of P_r are chosen optimally to fit the curve best using the minimal square error criterion. The mean square error of this fitting is f_r . Finally, among the candidate model orders, the model order m with the minimum fitting error, f_m , is selected as the true model order. In addition to the knee selection criterion, we also constrained that the

estimated h(t) must be positive and finite after its peak value, and the estimated LAP must be greater than zero as well as smaller than PADP.

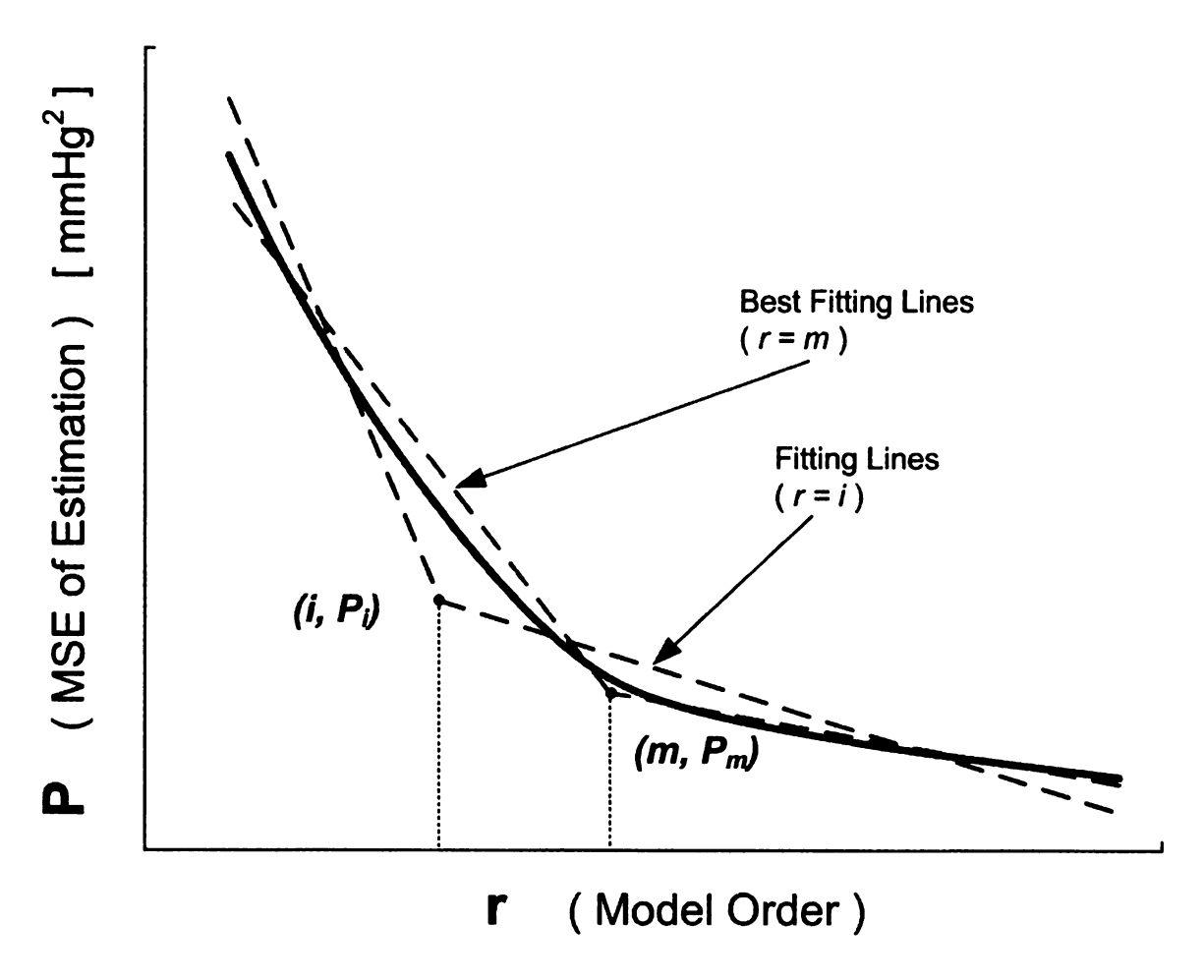


Figure 4.5 Illustration of the "knee" order selection algorithm. The solid line is the estimation mean square error (MSE) of Eq. 4.1 plotted against the MA model order (r). The two dash lines are two fitting lines at r=i and r=m respectively. (i, P_i) and (m, P_m) are interceptions of the fitting lines. Because the fitting error at r=m is minimum (could be seen from the plot), the true model order is m.

4.2.2 Technique Evaluation

We evaluated this technique with respect to pulmonary artery catheterization data from the MIMIC database (see Chapter 3). We created a sub-database based on 8 patient records including both PAP waveforms and multiple CO measurements and 5 patient records including both PAP waveforms and PCWP measurements as follows.

Step 1, we downloaded all of the one-minute thermodilution CO values as well as twelve-minute contiguous segments of the corresponding PAP waveforms (from 6 minutes preceding the beginning of the CO measurements to 6 minutes after the beginning of the CO measurements). We downloaded the PCWP and PAP measurement pairs in the same way.

Step 2, we visually examined each PAP waveform and extracted the longest continuous segment of relatively artifact free data from each waveform. We discarded those segments that were less than 5 minutes in duration. To this end, a total of 52 pairs of simultaneous measurements of PAP waveforms and thermodilution CO from 8 patient records, and 33 pairs of simultaneous measurements of PAP waveforms and PCWP from 7 patient records remain. For LAP estimation, we further evaluated the gold standard PCWP measurements according to the next three steps.

Step 3, we looked through all of the PAP waveforms corresponding to the PCWP measurements and eliminated those that apparently did not contain PCWP measurements and those invalid measurements.

Step 4, we eliminated those PAP waveforms with misinterpreted PCWP measurements. The timing of PCWP measurement is critical because intrathoracic pressures can vary widely with inspiration and expiration and are transmitted to the

pulmonary vasculature. During spontaneous inspiration, the intrathoracic pressures decrease (more negative); during expiration, intrathoracic pressures increase (more positive). The situation is reversed by the positive pressure ventilation. In order to minimize the effect of the respiratory cycle on intrathoracic pressure, measurements are usually obtained at end-expiration, when intrathoracic pressure is closest to zero. To simplify the measurement, the mean pressure during wedge measurement period could be utilized as a rough approximation of end-expiratory pressure. Therefore, we used the mean pressure during the wedging measurement period as a gold standard to evaluate the PCWP measurement value in the database.

Step 5, we evaluated the PCWP measurements following the selection criteria shown in Fig. 4.6. The physiologic principles behind the criteria are: a) mean PAP must be higher than LAP to maintain uni-direction blood flow from right ventricle to left atrium; b) under certain conditions, "a" and "v" waves on LAP must be visible on the wedge pressure waveform while PAP pulses are not visible [Morris et al., 1984; Leatherman et al., 2003]. The possible reason of mean PAP<=PCWP may be the balloon over-inflation. Pulmonary hypertension is defined as the condition that pulmonary artery pressure higher than 25mmHg [Weir et al., 1998].

Finally, 26 pairs of simultaneous measurements of PAP waveforms and PCWP from 5 patient records, as well as 52 pairs of simultaneous measurements of PAP waveforms and thermodilution CO from 8 patient records, remained for the subsequent evaluation of our mathematical analysis technique.

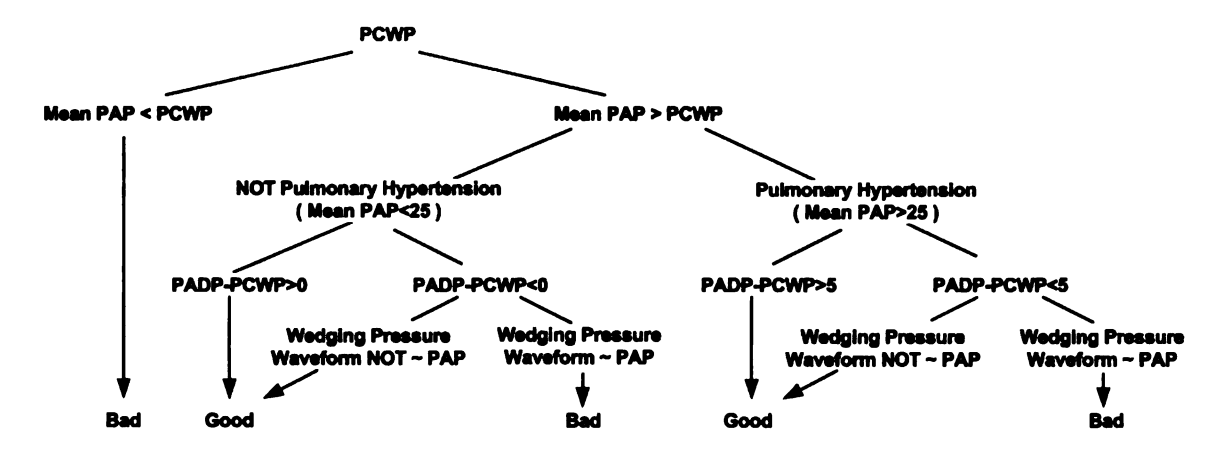


Figure 4.6 PCWP measurement evaluation procedure. Pulmonary hypertension is defined as the condition that pulmonary artery pressure higher than 25mmHg [Weir et al., 1998].

We observed that, for the same patient record in the MIMIC database, the PAP waveforms were generally much more corrupted than radial ABP waveforms, mainly because the pulmonary circulation is a low pressure and low resistance system. In addition, the phenomena of bifurcation and tapering are much more serious than the arterial tree. Moreover, the periodic respiration waves on the PAP waveforms were more significant, because the whole pulmonary circulation is in the thorax and as a result, the intrathoracic pressure (negative pressure in thorax) has bigger effect on the PAP than ABP. The movement of the catheter due to respiration also causes big artifact. This corruption introduced a problem was that sometimes the beginning of the upstroke of PAP was difficult to determine. In contrast, the "R" wave in ECG signal (measured in most ICU patients) was easy to identify and therefore used as a surrogate for the beginning of the upstroke of PAP. Then, the input (x(t)) in Eq. 4.1 was constructed as a

train of unit-area impulses located at the "R" waves. In fact, "R" wave represents the beginning of the ventricular systole, which is a more valid representation of cardiac contraction theoretically. For Eq. 4.1, we empirically set the AR order m to equal half of the MA order n and searched the optimal MA order from 15 to 70.

We were then able to compare the technique as applied to each PAP waveform segment with the corresponding thermodilution measurement or corresponding PCWP measurement. After scaling the resulting proportional CO estimates to have the same mean value as thermodilution in each patient record, we computed the CO RMSNE (normalized by thermodilution measurement value and given in percent) as well as the LAP RMSNE (normalized by PCWP and given in percent) as scalar metrics for comparison.

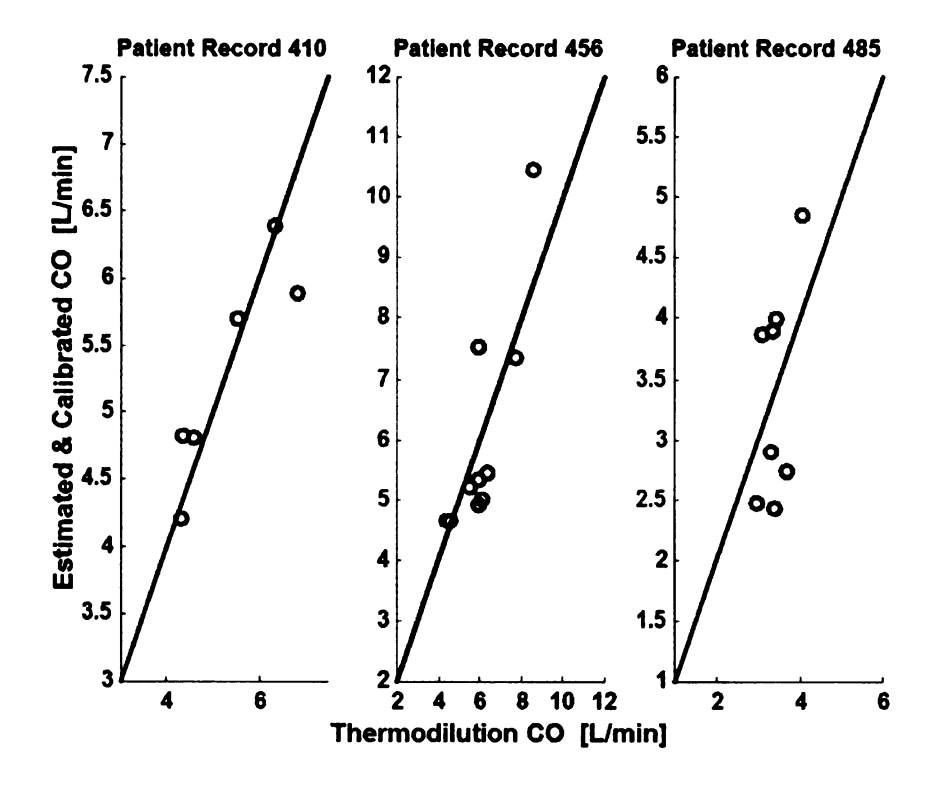
4.2.3 Evaluation Results

Table 4.1 summarizes the study and shows that the technique achieved an overall CO RMSNE of 14.6% and overall LAP RMSNE of 15.2%, which would be acceptable levels of error according to Critchley [1998]. For comparison, LAP estimation via median pulmonary artery diastolic pressure (PADP) resulted in an overall LAP RMSNE of 34.6%. Our estimated LAP values distribute evenly above and below the PCWP measurements. Fig. 4.7a gives visual examples of the CO estimation results from 3 patients, in which the estimated and calibrated CO values are plotted against the corresponding thermodilution measurements. Fig. 4.7b gives visual examples of the LAP estimation results from 3 patients, in which the estimated LAP values are plotted against

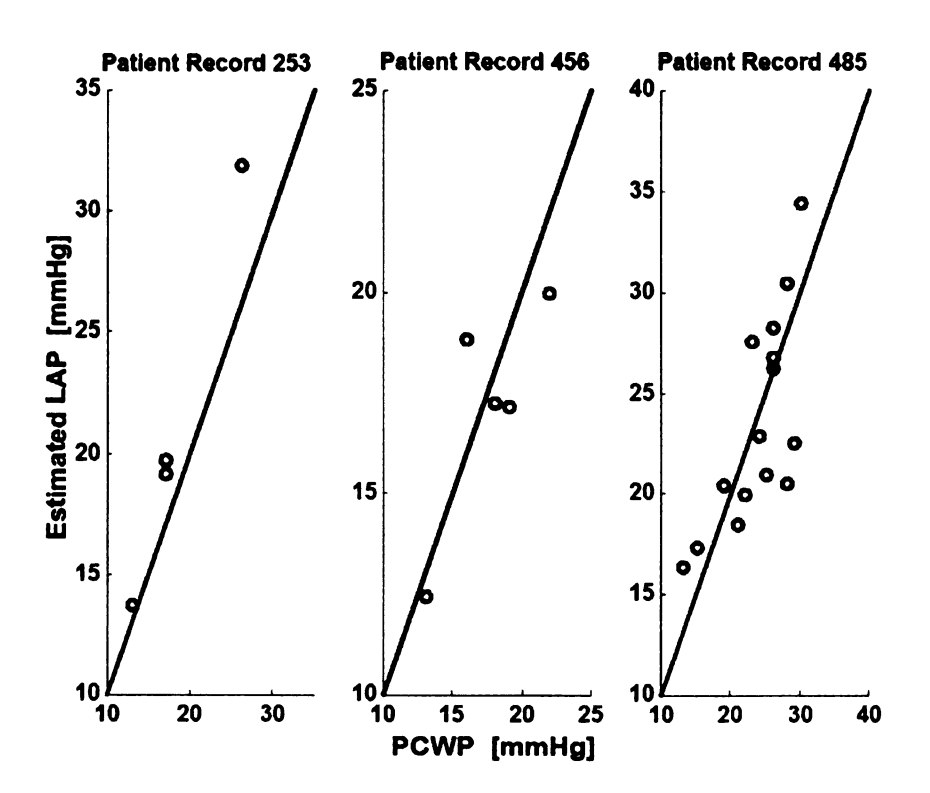
the corresponding PCWP values. We believe that these estimation results demonstrate the feasibility of the technique.

Table 4.1: Summary of the intensive care unit patient records and CO and LAP estimation results of the human hemodynamic data set. The technique was applied to PAP waveforms from 9 patient records and achieved an overall CO root-mean-squared-normalized error (RMSNE) of 14.6% with respect to 52 thermodilution measurements and an overall LAP error of 15.2% with respect to 26 PCWP measurements. MPAP is mean PAP.

PATIENT RECORD	CO RANGE [L/MIN]	MPAP RANGE [MMHG]	PCWP RANGE [MMHG]	HR RANGE [BPM]	CO RMSNE [%]	LAP RMSNE [%]
253		23-41	13-26	54-72		13.2
410	4.3-6.8	19-23		60-90	7.6	
411	3.2-4.6	30-37		58-60	13.8	
456	4.4-8.5	22-33	13-22	78-108	14.8	11.4
474	3.8-4.9	21-26	9-14	84-108	15.7	12.7
476	3.8-4.8	15-20		102-108	13.8	
482	4-4.3	25-28	13	84	5	25.4
484	5.1-6.8	28-31		84-96	7.4	
485	3.0-4.1	23-44	19-30	102-114	21.9	16.3
TOTAL	3.0-10.5	15-44	9-30	50-116	14.6	15.2



(a)



(b)

Figure 4.7 Visual examples of CO and LAP estimation from three intensive care unit (ICU) patients. (a), for each patient, the estimated and calibrated CO is plotted against corresponding thermodilution measurement; (b), for each patient, the estimated LAP is plotted against corresponding pulmonary capillary wedge pressure (PCWP) measurement.

4.2.4 Discussion

We have developed a technique to continuously monitor CO and LAP by analyzing a PAP waveform measured with a PAC over time intervals of about 6 minutes. This technique is an extension of the technique in Chapter 3: continuous monitoring of CO from a peripheral ABP waveform. We evaluated the technique in humans based on the MIMIC database. With this database, we were able to compare the application of the technique to PAP waveforms obtained from the PAC with reference thermodilution and PCWP measurements in a total of a total of 9 ICU patients in which CO and LAP were changing due to disease progression and therapy. We report an overall CO estimation error of 14.6% and an overall LAP estimation error of 15.2% (see Table 4.1 and Fig. 4.7).

The technique is based on the assumption that the simple Windkessel model (Fig. 4.3b) is a valid representation of the long time scale behavior of the pulmonary

circulation. The model has two important assumptions. The model ignores ITP which contributes more to PAP than ABP because PAP is much lower than ABP. The model also assumes that the PVC is constant over time scales of hours to days. Any violation to these assumptions may introduce CO and LAP estimation error. However, the preliminary evaluation result implies that this assumption is valid at least to this data set.

The main advantage of this technique with respect to previous techniques for monitoring CO from PAP is the additional capability of estimating the absolute value of LAP. If the technique could estimate LAP accurately, then theoretically the CO estimation would also be accurate. Thus, LAP estimation should actually help improve the CO estimation.

Bourgeois et al may be utilized to compute the time constant τ if the diastolic pressure waveform of one specific cardiac cycle resembles an exponential decay. It works well especially when part of the waveform is very clean while the overall quality is corrupted. However, it is hard to evaluate the waveform quality and extract the good part automatically.

As discussed in the introduction, the clinical measurement methods, thermodilution and PCWP, have questionable accuracy due to their assumptions, potentially poor operation, and misinterpretation. In the MIMIC data, many PCWP waveforms have large periodic artifact caused by respiration (e.g., movement of catheter). We also found that there were significant differences in the quality of PCWP measurements between different patients. That is, the PCWP measurement quality was highly dependent upon the experience of the operator, which is consistent with the findings of Morris et al. For example, for patient record 456, all of the wedging pressure waveforms were clean and

all of the PCWP values were measured at the end-expiration. However, for patient record 485, most of the wedging pressure waveforms were affected by the respiration and the PCWP values were computed by simply taking the averages of the pressure during the wedging period. Because the PCWP waveform can be observed on the PAP waveform, we can at least to some degree assess its quality. This is an advantage of PCWP over thermodilution.

The CO may be easily calibrated with thermodilution because a PAC has already been used to measure PAP. However, the measurement of absolute CO value may be unnecessary in the context of continuous monitoring in the acute setting in which only CO changes are clinically relevant.

Comparison of the CO estimation results of this technique and the technique of Chapter 3 is very interesting. As shown in Table 3.2 and Table 4.1, seven patients had both radial ABP and PAP measurements and consisted of more than one thermodilution measurement. In four patient records, 411, 474, 476, and 485 the estimation results from the two techniques have equivalent accuracy. While in the other three patient records, 410, 456, and 484, the estimation of CO from PAP is much better than from ABP. This comparison is surprising, because the ABP signals are much "cleaner" than the PAP signals (e.g., patient record 456). However, we note that the comparison is based on a few data points.

The result of this ICU patient evaluation study indicates that our mathematical analysis technique for continuously monitoring CO and LAP may be sufficiently accurate with respect to PAP waveforms measured from critically ill patients. With further

successful human testing, the technique may potentially be applied in ICU patients instrumented with the PAC.

4.3 Monitoring of CO and LAP from RVP

4.3.1 The Technique

First, we rewrite the ARX model of Eq. 4.1 as follows:

$$y(t) = c + \sum_{k=1}^{m} a_k y(t-k) + \sum_{k=1}^{n} b_k x(t-k) + w(t), \qquad (4.3)$$

ć.

where, y(t) is the partially constructed the PAP waveform from RVP waveform (Fig. 4.2), x(t) is a pulse train representing heart contractions, and c is reflective of the contribution of LAP to PAP. The solution of this ARX model equation requires continuous measurement of the PAP waveform. However, by constructing the PAP waveform from RVP waveform, we can only obtain the PAP waveform during each ejection phase. Thus, the $\{a_k\}$ and $\{b_k\}$ parameters cannot be identified, and the response of PAP to a single ventricular contraction and the average LAP cannot be obtained.

Instead of the ARX model in Eq. 4.3, the relationship between x(t) and y(t) may be represented by an output error (OE) model in Z transform as follows:

$$Y(z) = \frac{B(z)}{A(z)}X(z) + c + W(z),$$
 (4.4)

where $A(z) = 1 - \sum_{k=1}^{n} a_k z^{-1}$ is the Z transform of the coefficients $\{a_k\}$, $B(z) = \sum_{k=1}^{m} b_k z^{-1}$ is

the Z transform of the coefficients $\{b_k\}$, and W(z) is the Z transform of the unobserved noise [Ljung, 1999]. Note that the coefficients $\{a_k\}$, $\{b_k\}$, and c are different from those parameters in Eq. 4.3.

In order to solve the coefficients $\{a_k\}$, $\{b_k\}$, and c, we convert Eq. 4.4 to a linear equation. Assuming for the moment that $\{a_k\}$ is known, we establish a time series u(t) with the Z transform as follows:

$$U(z) = \frac{1}{A(z)}X(z)$$
. (4.5)

Then, by substituting Eq. 4.5 into Eq. 4.4, we obtain

$$Y(z) = B(z)U(z) + c + W(z)$$
. (4.6)

The $\{b_k\}$ and c can then be estimated using the linear least square method.

To estimate the $\{a_k\}$ parameters, for the sake of simplicity, we assume that the poles are composed of two components: a pure exponential decay (with time constant τ_I) and a cosine (frequency f) attenuated exponentially (with time constant τ_2). The first component is due to the long time scale behavior of the pulmonary vessels, which are represented by the pulmonary vessel resistance (PVR) and compliance (PVC) as shown in Fig. 4.3b. The second component represents faster wave reflection and inertial effects. Thus, in Eq. 4.4, the order of A(z) is n=3, and Z transform of $\{a_k\}$ is specifically:

$$A(z) = (1 - e^{-T/\tau_1} z^{-1})(1 - 2e^{-T/\tau_2} \cos(2\pi f T) z^{-1} + e^{-2T/\tau_2} z^{-2}), \qquad (4.7)$$

where T is sampling period.

Therefore, in our estimation algorithm, we compute coefficients the $\{a_k\}$, $\{b_k\}$ and c as follows. First, we choose the values of τ_I , τ_2 and f in Eq. 4.7 within a physiologically reasonable range to compute A(z). Then, we compute u(t) using Eq. 4.5. Next, we estimate $\{b_k\}$ and c in Eq. 4.6 using the linear least squares method by minimizing $\|\mathbf{w}(t)\|^2$. LAP is given by c, and the time constant of the pulmonary artery is given by $\mathbf{r}=\mathbf{r}_1$. We repeat these steps for a range of different time constants τ_I and τ_2 and frequency

f. The true $\{a_k\}$, $\{b_k\}$ and c are those parameters that result in the minimal least square error in Eq. 4.6. The proportional CO is then computed as the convolution of h(t) and u(t) divided by τ .

Fig. 4.8 illustrates the technique, which is an extension of the estimation technique of CO and LAP from a single PAP waveform. The difference here is that the PAP waveform (y(t)) is known only during the ejection phase (thick solid line) while unknown during the remaining time (thin dash line). The technique is basically to minimize the estimation error of the PAP waveform constructed from the RVP waveform during the ejection phase.

4.3.2 Pilot Evaluation of the Technique

To evaluate this technique, we conducted a pilot experiment in a female adult anaesthetized dog on a ventilator. ECG, CO, aortic pressure, RVP, PAP and LAP were measured and sampled at 1000Hz. The dog's chest was open for measurements of CO with an aortic flow probe and LAP with a catheter in the left atrium. These signals were recorded during the following four interventions: baseline, high dose dobutamine, low dose dobutamine, and volume depletion. Each intervention was ten minutes long. The experiment was done carefully and the measured waveforms were artifact-free (Fig.4.2).

We applied the technique in Section 4.2 to the measured PAP waveform and the extended technique in this section. For the RVP waveform, we performed the estimation as follows. First, the RVP signal was decimated down to 100Hz. The beginning of ejection period was determined by finding the maximum slope of the RVP waveform for beat, which conflicts with the assumption based on. Finally we obtained the best

parameters $\{a_k\}$, $\{b_k\}$ and c by minimizing the mean square error in Eq. 4.6.each beat [Adamson et al., 2003]. We assumed that the ejection period ended at a time 0.02 seconds after RVP reaches its peak value. The pulse train representing right ventricular contractions is located at the beginning of ventricular systole with an area equal to the ensuing pulse pressure of the constructed PAP.

The τ_I , τ_2 and f in Eq. 4.7 were selected within a physically valid range and constrained with the criteria $\tau_I > \tau_2$ and $f > 1/\tau_I$. A total of 20000 different sets of τ_I , τ_2 and f were evaluated. We then removed those parameters whose resulting impulse response was physiologically unreasonable, for example, the impulse response became after one

4.3.3 Results

The estimation results of monitoring CO and LAP from the PAP and RVP waveforms in the dog experiment are shown in Fig.4.9. For each technique, the CO estimation error is very small, and the LAP estimation is fairly accurate except one data point. The results demonstrate the potential of the techniques to be utilized in either ICU patients instrumented with PAC or patients with implanted devices for monitoring RVP. However, much more future animal testing is needed.

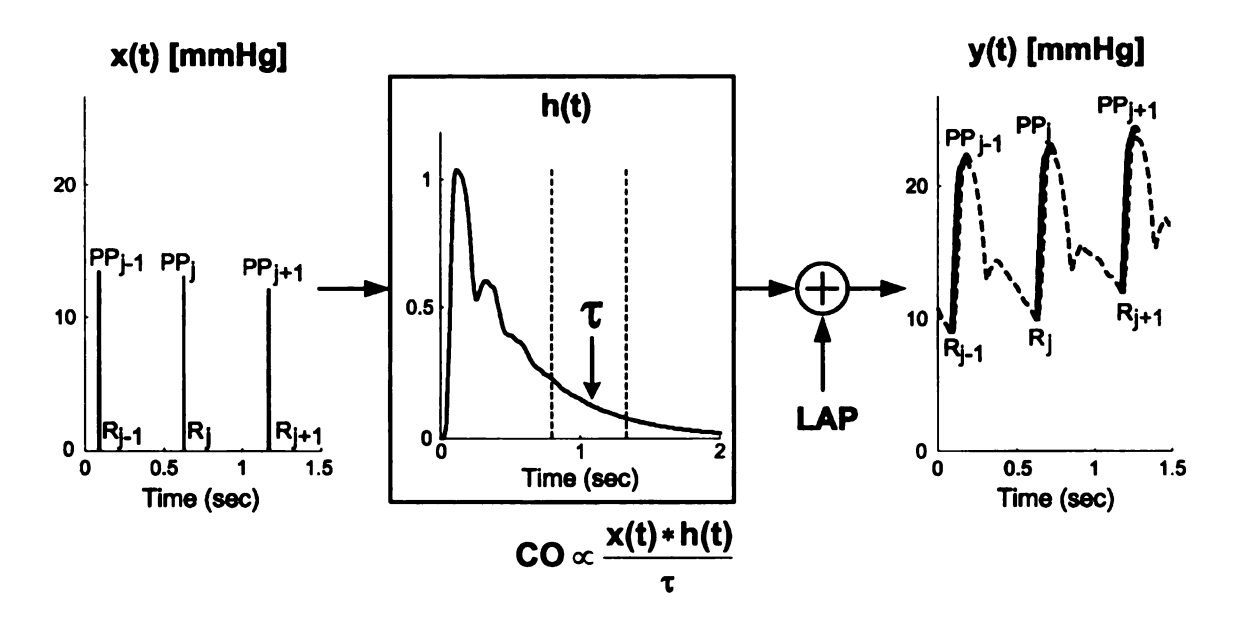


Figure 4.8 Illustration of identifying the time constant τ and LAP from RVP. The h(t) and LAP are obtained by minimizing the mean square estimation error of RVP of the ejection phase. x(t), a cardiac contractions signal constructed from RVP; y(t), a systolic PAP waveform (thick solid line) constructed from ejection phase of RVP; and h(t), an estimated impulse response coupling x(t) to y(t).

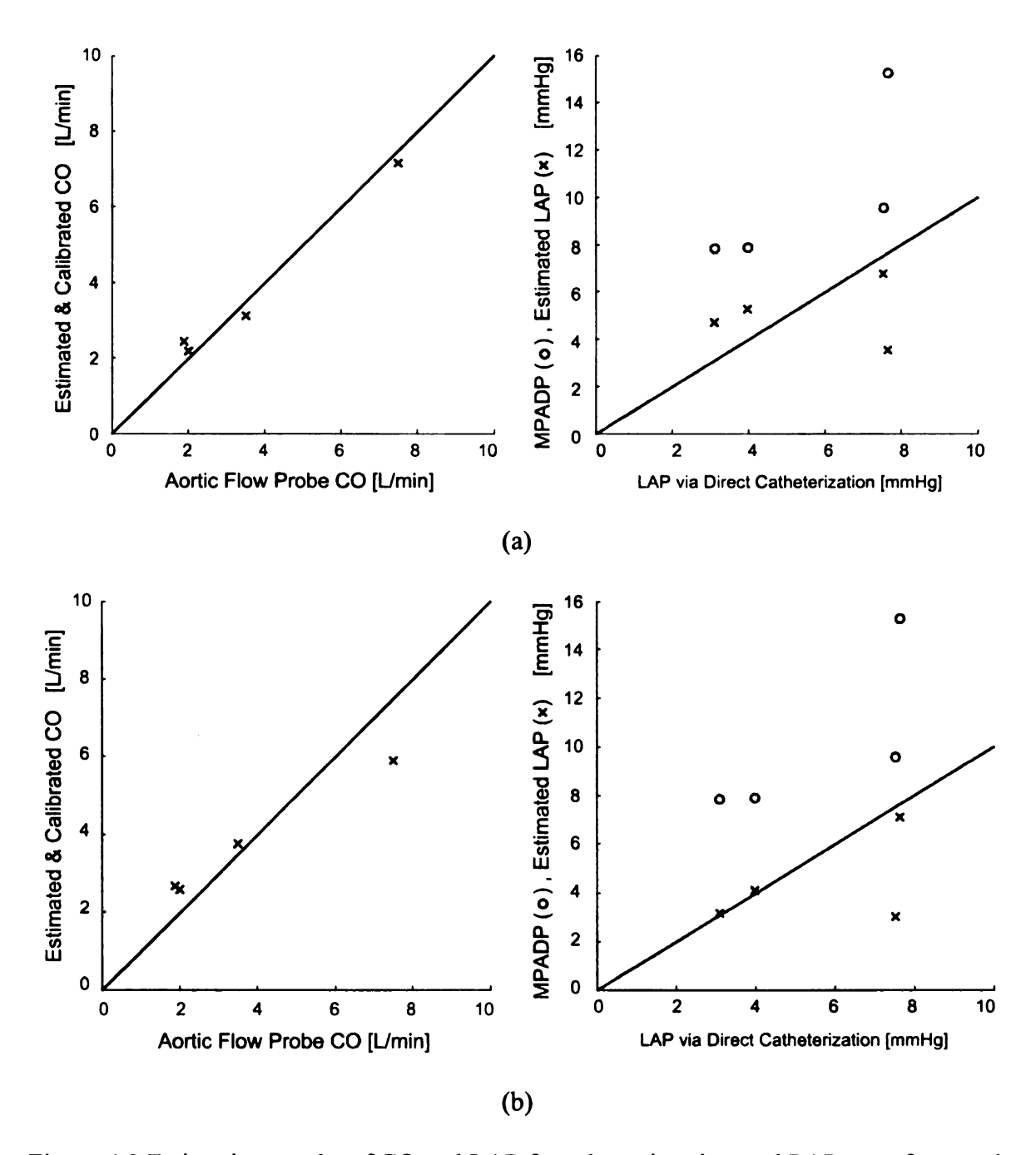


Figure 4.9 Estimation results of CO and LAP from long time-interval PAP waveform and RVP waveform in a dog. (a), CO estimated from PAP waveform plotted against CO measured by aortic flow probe, and LAP estimated from PAP waveform plotted against LAP measured by direct catheterization; (b), CO estimated from RVP waveform plotted against CO measured by aortic flow probe, and LAP estimated from RVP waveform plotted against LAP measured by direct catheterization.

CHAPTER 5

MONITORING LEFT VENTRICULAR CONTRACTILITY FROM RESPIRATORY-INDUCED BLOOD PRESSURE VARIABILITY

5.1 Background

The fastest growing cardiac disease is heart failure (the progressive weakening of the heart), which can lead to exhaustion and disability. It currently affects nearly five million Americans. Heart failure can be a life threatening condition; but if it is detected early enough, it can be treated with life style changes, relatively inexpensive drugs such as ACE inhibitors and beta-blockers, bypass surgery or angioplasty, and implantable devices. Thus, it is becoming increasingly important to be able to measure a specific index of left ventricular contractility so as to guide therapy.

The clinical approach for monitoring cardiac function usually involves employing imaging techniques such as echocardiography and radionuclide ventriculography to measure the ejection fraction (the ratio of the stroke volume to the ventricular end-diastolic volume). Although the ejection fraction is relatively easy to estimate, it is heavily dependent on the pressure in the ventricle prior to ejection (preload) and the pressure against which the ventricle pumps blood (afterload). That is, ejection fraction is not a specific or pure index of ventricular contractility. While other indices have been introduced (e.g., maximum rate of change of left ventricular pressure [Katz et al., 1992]), they all generally suffer from substantial load dependence as well.

Suga and Sagawa were able to identify a relatively specific index of left ventricular contractility [Suga and Sagawa, 1974; Sagawa et al., 1977]. In their pioneering work,

they demonstrated that the pressure-volume relationship of the isolated canine left ventricle can be represented by a line whose slope (elastance) varies from its minimum value at the end of diastole to its maximum value at the end of systole (Fig. 5.1). That is, the left ventricle behaves analogously to a time-varying electrical capacitor whose capacitance is simply the reciprocal of elastance. More importantly, the maximum elastance is highly sensitive to the changes in ventricular contractility, but relatively insensitive to the alterations of the loading conditions [Sagawa et al., 1977; Suga et al., 1973b; Suga and Sagawa, 1974]. They referred to this specific index of left ventricular contractility as E_{lv}^{max} (Fig. 5.1). While subsequent investigators corroborated this result in intact dogs [Kass et al., 1986] and humans [Kass et al., 1989], others complicated the E_{lv}^{max} concept by reporting afterload dependence [Suga et al., 1973a; van der Velde et al., 1991] and contractility-dependent curvilinearity of the ventricular end-systolic pressure-volume relationship [Burkhoff et al., 1987; Kass et al., 1989; van der Velde et al., 1991]. However, the most significant load-dependence and nonlinearity occurred over a wide range of ventricular volumes and/or in vivo in which the accuracy of the measurement technique is reduced (see below). Therefore, E_{lv}^{max} as determined over a limited range of ventricular volumes, is generally considered to be a valuable index of left ventricular contractility [Burkhoff et al., 1986; Chen et al., 2001; Kass et al., 1989; Takeuchi et al., 1991].

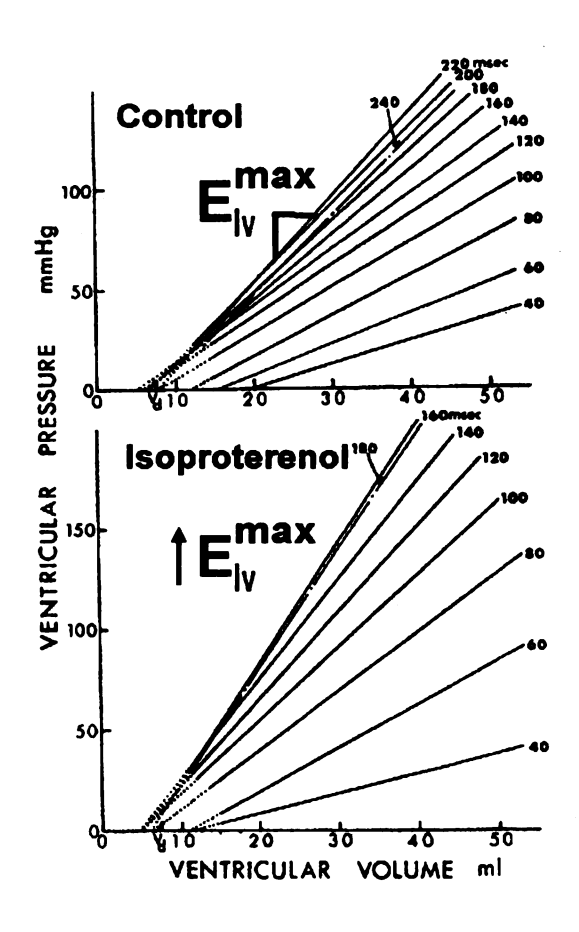


Figure 5.1 Illustration of left ventricular elastance (E_{lv}) and the left ventricular maximum elastance (E_{lv}^{max}). The left ventricular pressure is plotted against the left ventricular volume. Left ventricle can be represented by a time-varying capacitor, which is reciprocal of E_{lv} (slope of lines). E_{lv}^{max} is a specific index of left ventricular contractility. [Suga and Sagawa, 1974].

Although the significance of E_{lv}^{max} is well appreciated, it is rarely employed because of the difficulties involved in its measurement. The conventional technique involves measuring the multiple left ventricular pressure-volume loops during the interventions that ideally alter the loading conditions without affecting the contractility (Fig. 5.2a). Left ventricular pressure can be measured with high fidelity, but very invasive methods are required to do so. Moreover, although left ventricular volume can be estimated with non-invasive methods such as echocardiography, even highly invasive methods are not reliable [Burkhoff, 1990]. An example of experimental left ventricular pressure-volume loops is shown in Fig. 5.2b [Kass et al., 1988]. Finally, the adjustment of loading conditions is not only invasive but also may change the contractile state. Perhaps, as a consequence, Freeman et al reported that E_{lv}^{max} was dependent on the method utilized to adjust the loading conditions [Freeman et al., 1986].

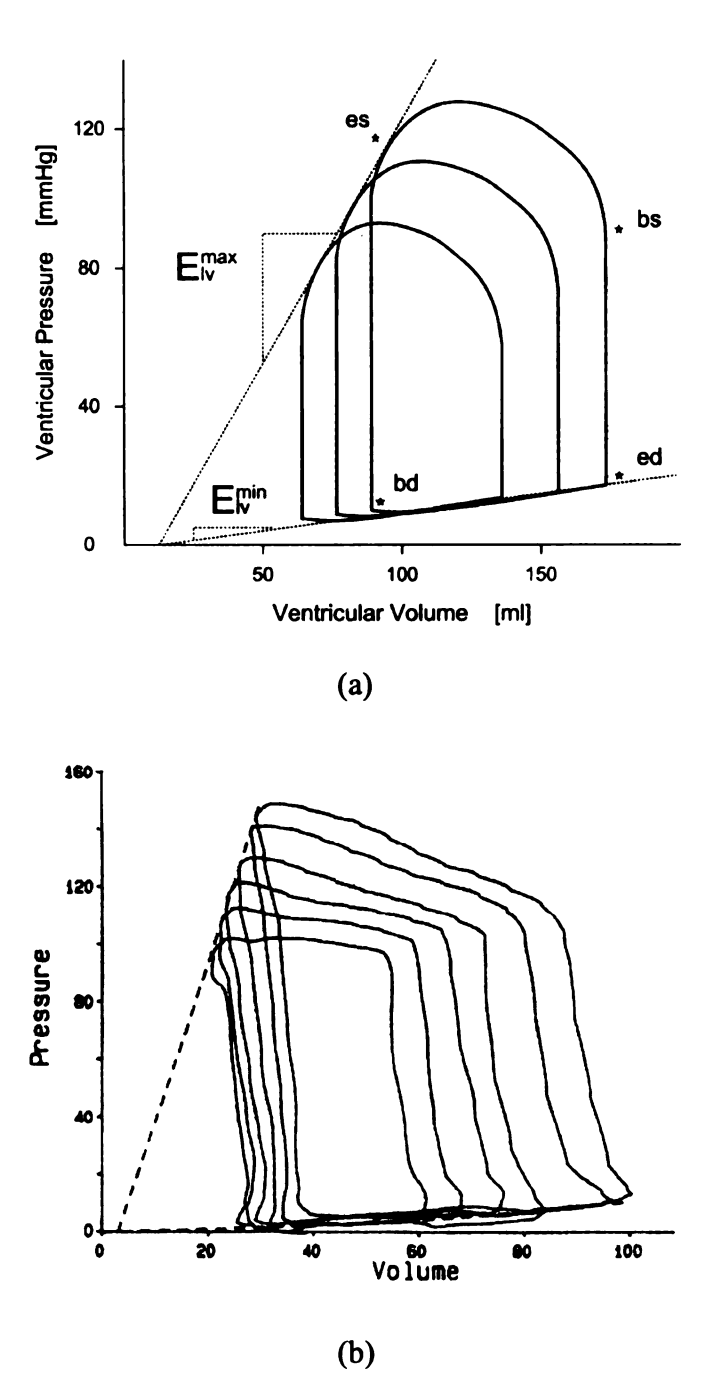


Figure 5.2 Illustration of conventional E_{lv}^{max} measurement method. (a), ideal left ventricular loop changed by preload, and the slope of the line fitting the end systolic pressure-volume points is E_{lv}^{max} ; (b), an experimental result, where left ventricular pressure-volume loop with loading condition were altered by drug administration and inferior vena cava balloon occlusion [Kass et al., 1988].

Previous investigators tried to pursue less invasive methods to measure E_{lv}^{max} .

Most of these methods aimed to estimate E_{lv}^{max} without adjusting the loading conditions from only one single beat. These techniques must be based on strict assumptions, as they are essentially attempting to measure a slope from only one single data point. Investigators have specifically assumed the time evolution of left ventricular elastance normalized in both amplitude and time is identical or very similar for all individuals regardless of cardiac state [Chen et al., 2001; Senzaki et al., 1996; Shishido et al., 2000]. Researchers have also assumed that the maximal isovolumic pressure at a given enddiastolic volume can be extrapolated from isovolumic phase pressure with an empirical formula [Chang et al., 1997; Shih et al., 1997; Sunagawa et al., 1980; Takeuchi et al., 1991]. Perhaps, as a result, it is not surprising subsequent investigators have found poor agreement between the conventional multiple beat method and single beat methods [Iwase et al., 1992; Kjørstad et al., 2002]. Moreover, only a few of the single beat methods did not require the measurement of left ventricular volume [Chang et al., 1997; Shishido et al., 2000], however, these methods do require aortic flow, which is not easy to measure as well [Ehlers et al., 1986].

In this Chapter, we present a practical technique for monitoring E_{lv}^{max} which may ultimately be employed to guide the clinical management of heart failure patients. In contrast to the previous multiple beat method and single beat methods, the novel technique specifically estimate the changes in E_{lv}^{max} by mathematically analyzing the beat-to-beat fluctuation of arterial blood pressure (Pa) and respiratory activities in terms of instantaneous lung volume (Q_{lu}) or intrathoracic pressure (P_{th}) during random-interval

breathing protocol [Berger et al., 1989a] in approximately six minutes. The key idea of this technique is based on the phenomenon named direct capacitive effect, which means that the magnitude of the immediate drop of Pa mechanically induced by inspiration is mainly due to changes in E_{lv}^{max} . Importantly, minimally invasive or non-invasive methods exist to continuously measure Pa (e.g., radial artery catheterization, arterial tonomatry), Q_{lu} (chest-abdomen inductance plethysmography) and P_{th} (esophageal balloon). Moreover, the technique monitors E_{lv}^{max} while the ventricular loading conditions are varied via a random-interval breathing protocol. Thus, multiple data points are effectively utilized to measure the E_{lv}^{max} slope. We then describe the performance of the technique with respect to realistic beat-to-beat variability generated by a human cardiovascular simulator [Mukkamala and Cohen, 2001]. We also conducted a pilot vealuation of the technique with respect to an anesthetized closed-chest canine model. Both experiments show the promise of the technique in monitoring changes in E_{lv}^{max} .

5.2 Physiologic Basis

5.2.1 Respiratory-Induced P_a Variability Mechanisms

Beat-to-beat fluctuations due to respiration are readily apparent in Pa waveforms (Fig. 5.3). These fluctuations are usually slower than the heart rate (HR) and are caused by multiple, distinct physiologic mechanisms operating over different time courses.

These mechanisms may be categorized into those mediated by the autonomic nervous system and those governed by mechanical phenomena.

Autonomic mechanisms are responsible for the well-known respiratory sinus arrhythmia phenomenon in which HR and respiratory variations are in synchrony (Fig. 5.4) [Eckberg et al., 1984; Saul and Cohen, 1994]. It has been shown that HR variations, which may initiate Pa variations through changes in cardiac output, actually precede the respiratory variations [Mukkamala et al., 1999; Mullen et al., 1997]. Specific mechanisms responsible for respiratory sinus arrhythmia may include direct neural coupling of HR and respiratory control centers in the brain (accounting for the non-causal effect) as well as the baroreflex system, which is stimulated by the changes in Pa [Saul and Cohen, 1994]. These mechanisms are mediated by the fast parasympathetic nervous system and the slower sympathetic nervous system [Akselrod et al., 1985]. Baroreflex excitation also causes variations in ventricular contractility, systemic arterial resistance, and systemic venous unstressed volume, which are solely mediated by the slow sympathetic nervous system [Guyton and Hall, 1996].

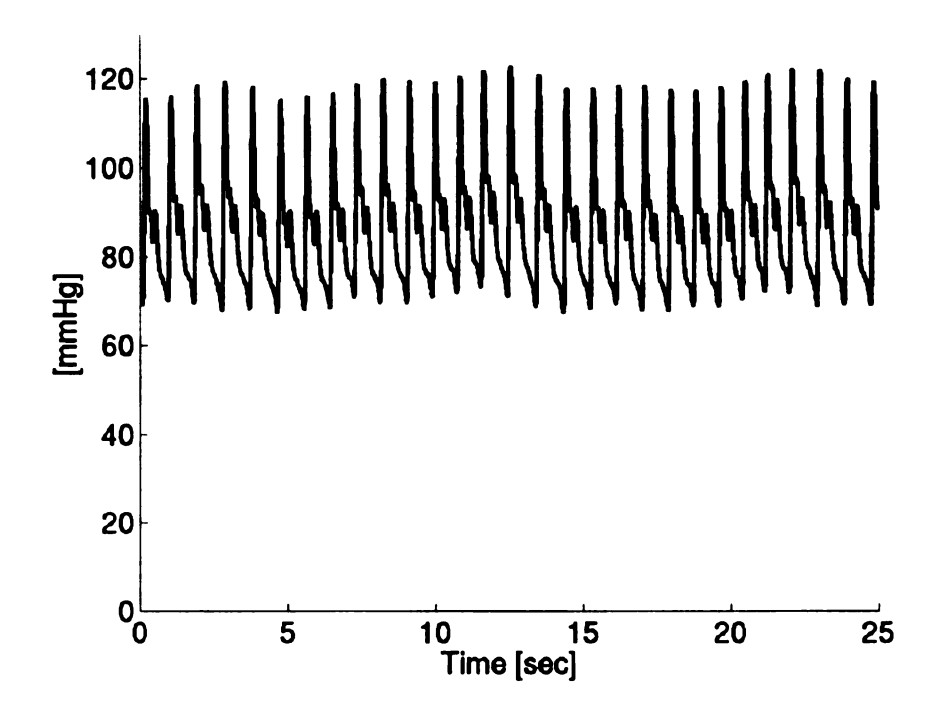


Figure 5.3 Respiratory waves on ABP waveform.

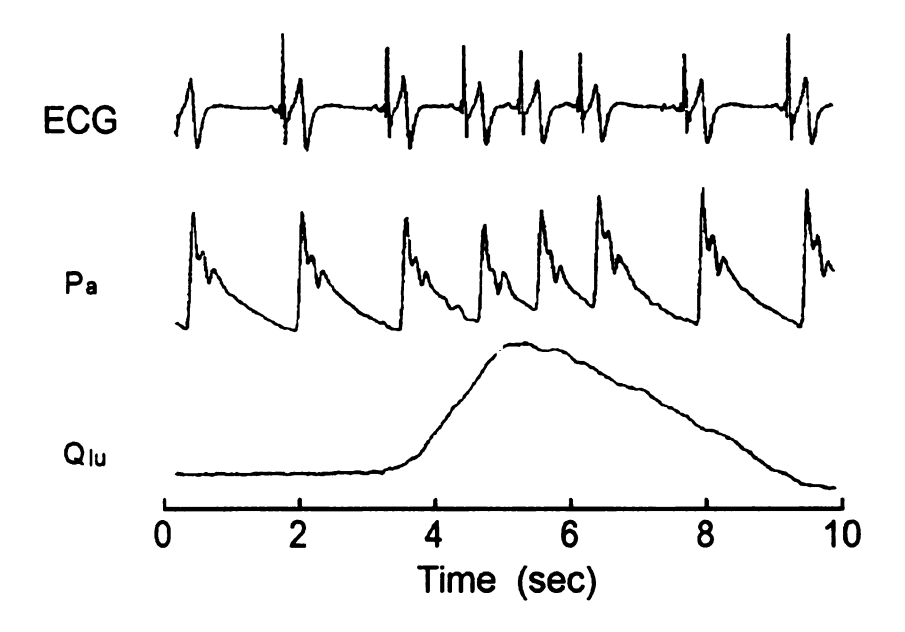
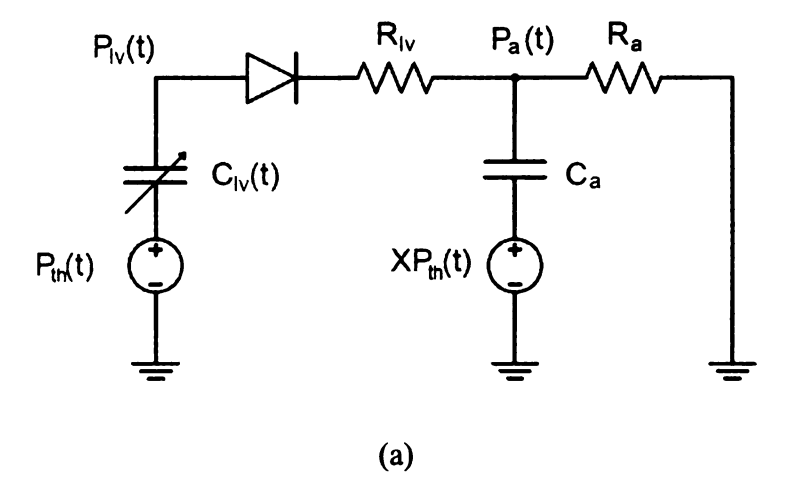


Figure 5.4 Illustration of respiratory sinus arrhythmia (RSA). The heart rate (ECG) is in synchrony with respiratory activity (Q_{lu}, instantaneous lung volume).

The mechanical phenomena are initiated by changes in P_{th} caused by chest expansion (inspiration) or chest contraction (expiration) [Guyton and Hall, 1996]. For example, the act of inspiration causes P_{th} to drop. This drop is immediately transmitted to left ventricular pressure and P_a, which we refer to direct capacitive effects. Then after a couple of beats P_a increases due to the enhanced venous return to the right heart [Saul and Cohen, 1994]. For a given P_{th} drop, the extent to which the enhanced venous return affects P_a is dependent on the properties of the right heart, pulmonary circulation, left heart, and systemic circulation. Thus, it would not be possible to distinguish between, for example, left and right ventricular failure or systolic and diastolic failure even if the extent of increase in P_a due solely to the enhanced venous return to the right heart could be quantified. In contrast, the direct capacitive effects essentially reflect only left ventricular contractility. We will discuss the direct capacitive effects in the next section.

5.2.2 Direct Capacitive Effects

The two-compartment electrical analog model in Fig. 5.5a represents the left ventricle and systemic arteries system. Each compartment consists of a conduit for viscous blood flow, which is characterized by a resistance (R), and a volume storage element, which is characterized by a capacitance (C). The external pressure (P) is P_{th} for left ventricle and X P_{th} for the systemic arteries, where X is the fraction of the total arterial compliance (Ca) subject to P_{th}. (X is caused by only parts of arteries is inside the chest and affected by P_{th}. X is typically about 1/3 in humans [Lawson, 1962]). The capacitance of the left ventricle oscillates over time (t) and is responsible for driving the flow of blood. Finally, the ideal diode represents the aortic valve and ensures uni-



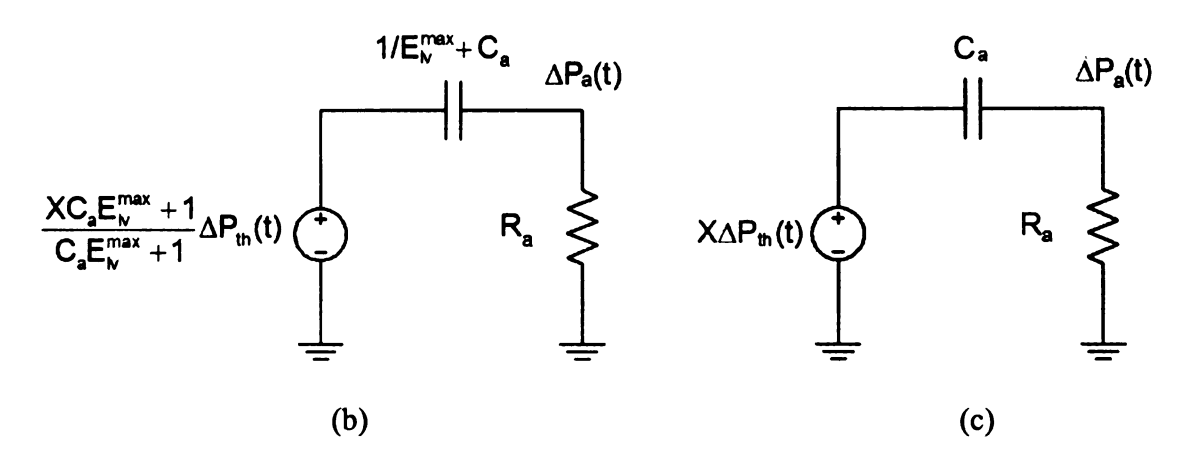


Figure 5.5 Two-compartment model of the left ventricle and systemic arteries in terms of the electrical circuit analog. (a), Model during one beat. R, resistance; C, compliance; P, pressure; diode, aortic valve; Δ , changes; lv, left ventricle; a, artery; th, intrathoracic; t, time. (b), Model during systole (diode representing aortic valve is shorted) in which $R_{lv}=0 \text{ and } C_{lv}(t)\approx 1/E_{lv}^{max} \text{ (as justified in the text). (c), Model during diastole (diode is opened). The technique herein aims to estimate quantities derived from this model that can reflect changes in left ventricular contractility in terms of <math>E_{lv}^{max}$.

directional blood flow. (Note that fast inertial and distributed effects are not considered here.) According to this model, when P_{th} increases suddenly, the arterial blood pressure P_{th} and P_{th} increases immediately because the capacitors P_{th} and P_{th} and P_{th} are called P_{th} in a very short time requires very fast breathing, which is difficult to realize practically. We will describe the direct capacitive effects during normal breathing and then quantitate direct capacitive effects below.

First, we study the two-compartment model shown in Fig. 5.5a. We assume that 1) $R_{lv}=0$ (i.e. no stenosis of the aortic valve) and 2) $C_{lv}(t)\approx 1/E_{lv}^{max}$ during systole. Note that any discrepancy in the second assumption is small and likely to be within the estimation error of the technique (see below), as the systolic ejection time and time derivative of left ventricular elastance (E_{lv}) at the end of systole are both very small, especially for failing hearts [Senzaki et al., 1996; Suga and Sagawa, 1974]. The nonlinear model of Fig. 5.5c may be viewed as two distinct first-order linear systems with the input $z(t)\Delta P_{th}(t)$ and the output $\Delta P_{a}(t)$, one during systole (Fig. 5.5b) and the other during diastole (Fig. 5.5c). The input $z(t)\Delta P_{th}(t)$ of this model is

$$\frac{XC_a E_{lv}^{max} + 1}{C_a E_{lv}^{max} + 1} \Delta P_{th}(t)$$
 during systole, and

$$X\Delta P_{th}(t)$$
 during diastole.

The transfer function is

$$\frac{j\omega R_a (1/E_{lv}^{max} + C_a)}{1 + j\omega R_a (1/E_{lv}^{max} + C_a)}$$
 during systole, and

$$\frac{j\omega R_a C_a}{1+j\omega R_a C_a} \quad \text{during diastole.}$$

According to the above transfer function, this system works like a high pass filter with the approximate cutting off frequency of $\omega_{\text{cut}} = (\text{RaCa})^{-1}$.

Next we will prove that because the frequency components of input are much higher than the cutting off frequency, the input signals will all transfer to output. Assuming the fluctuations $\Delta P_{th}(t) = C\cos(2\pi t/T_r + \phi)$, where Tr is the respiratory period, to compute the lowest frequency in input, we utilize the exponential Fourier series to expand z(t) as follows:

$$z(t) = \sum_{n=-\infty}^{\infty} D_n e^{j\frac{2\pi n}{T}t}.$$

where

$$D_{n} = \frac{j}{2\pi n} \left(1 - e^{-j\frac{2\pi n T_{S}}{T}} \right) \left(X - \frac{XC_{a}E_{lv}^{max} + 1}{C_{a}E_{lv}^{max} + 1} \right) \text{ for } n \neq 0, \text{ and}$$

$$D_{0} = \frac{T - T_{s}}{T} X + \frac{T_{s}}{T} \left(\frac{X C_{a} E_{lv}^{max} + 1}{C_{a} E_{lv}^{max} + 1} \right).$$

Then, the input
$$z(t)\Delta P_{th}(t) = \sum_{n=-\infty}^{\infty} \frac{CD_n}{2} e^{j2\pi\left(\frac{1}{T_r} + \frac{n}{T}\right)t + j\phi} + \sum_{n=-\infty}^{\infty} \frac{CD_n}{2} e^{j2\pi\left(\frac{n}{T} - \frac{1}{T_r}\right)t - j\phi}$$
.

According to the equation, for $T_r \ge 2T$, the smallest frequency of an exponential term in S(t) is $2\pi/T_r$. Thus, since $2\pi/T_r$ (~1.6 rad/sec) is usually larger than $(R_aC_a)^{-1}$ (~0.5 rad/sec [Sato et al., 1974]), we arrive at the approximations

$$\Delta P_a(t) \approx z(t) \Delta P_{th}(t)$$
. (5.1)

Therefore, the response of Pa to a known change in Pth during systole as a result of only the direct capacitive effects is approximately given as follows:

$$\frac{\Delta P_a(t)}{\Delta P_{th}(t)} \approx \frac{XC_a E_{lv}^{max} + 1}{C_a E_{lv}^{max} + 1}.$$
 (5.2)

whereas the response of Pa to a known change in Pth during diastole due to only direct capacitive effects is approximately given as follows:

$$\frac{\Delta P_a(t)}{\Delta P_{th}(t)} \approx X. \tag{5.3}$$

Since C_a (and X) is relatively constant on the time scale of days to months and over a wide pressure range [Bourgeois et al., 1976; Hallock and Benson, 1937; Mukkamala et al., 2003b; Remington et al., 1945], any changes in the direct capacitive coupling between P_{th} and P_a must be specifically due to changes in E_{lv}^{max} .

5.2.3 Ventilatory Mechanism

The measurement of P_{th} is somewhat invasive. The instantaneous lung volume (Q_{lu}) may be measured non-invasively by placing belt around the chest and abdomen, as a surrogate of P_{th} . We utilized the electrical analog model of ventilatory mechanics depicted in Fig. 5.6. This model includes a resistor (R_{air}) representing the viscous airways and a capacitor (C_{lu}) indicating the volume capability of the lungs. Based on this model, changes in P_{th} are related to changes in Q_{lu} as follows:

$$C_{lu}\Delta P_{th}(t) = -\tau \frac{d\Delta Q_{lu}(t)}{dt} - \Delta Q_{lu}(t), \qquad (5.4)$$

where $\tau = R_{air}C_{lu}$ represents the time constant governing ventilatory mechanics. If τ were known, the proportional P_{th} changes could be obtained via Eq. 5.4 and act as a surrogate of P_{th} in Eqs. 5.2 and 5.3 to compute the direct capacitive effects.

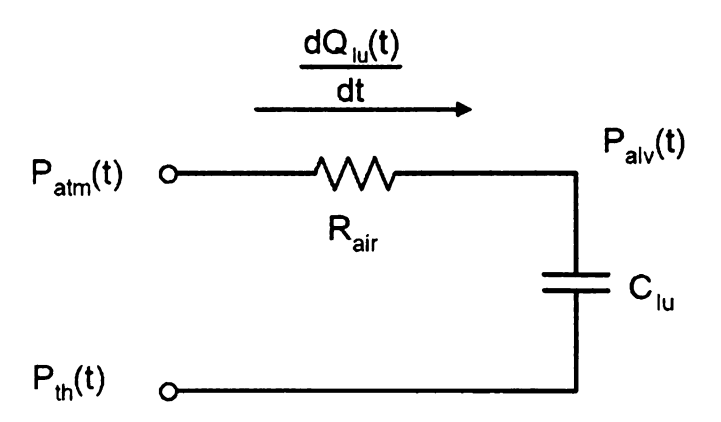


Figure 5.6 Model of ventilatory mechanics in terms of its electrical circuit analog. air, airway; lu, lung; atm, atmosphere; alv, alveolar pressure. See Fig. 5.5 caption for remaining variable definitions. This model is utilized to formulate a quantitative mapping from Q_{lu} to proportional P_{th} in order to develop a totally non-invasive technique for monitoring index h_3 derived from E_{lv}^{max} .

5.2.4 Three Indices Derived From E_{lv}^{max}

Since this technique does not require measuring volume (or blood flow), the absolute value of E_{lv}^{max} cannot be measured. However, from the concept of E_{lv}^{max} we derived three indices of left ventricular contractility, which are sufficient to monitor the changes in left ventricular contractility under different circumstances.

The first index analyzes beat-to-beat P_a and P_{th} fluctuations without regard to the phase of the cardiac cycle (i.e., systole and diastole) in order to estimate a single lumped index reflecting both Eqs. 5.2 and 5.3 (h₁). The actual value of h₁ is determined by C_a , E_{lv}^{max} , X and the ratio of systolic period to diastolic period. This index is expected to increase with decreasing E_{lv}^{max} .

The second index is $h_2=C_a\,E_{lv}^{max}$, which can be computed from Eqs. 5.2 and 5.3. Since C_a is a constant as stated above, this index is proportional to E_{lv}^{max} . The direct capacitive effects in systole and diastole are identified by analyzing beat-to-beat P_a and P_{th} fluctuations separately.

In order to monitor E_{lv}^{max} non-invasively, we utilize the P_a and Q_{lu} to identify a specific index h_3 . With the proportional P_{th} (Eq. 5.4) and P_a , the technique could then estimate the two quantities in Eqs. 5.2 and 5.3, which would each be scaled by C_{lu} . By computing the ratio of the two estimated quantities, the scale factor C_{lu} would be canceled and then the ratio, the third index h_3 , only reflects the changes in E_{lv}^{max} :

$$h_3 \approx \frac{XC_a E_{lv}^{max} + 1}{XC_a E_{lv}^{max} + X}.$$
 (5.5)

This index would increase with decreasing E_{lv}^{max} .

5.3 Signal Processing Algorithm

The direct capacitive effects cannot be measured from beat-to-beat variability by simply computing ratios of Pa fluctuations to Pth fluctuations (as indicated in Eqs. 5.2 and 5.3). The reason is that the Pa fluctuations are also due to the past histories of Pth fluctuations (e.g., enhanced venous return to the right heart) and Pa fluctuations (e.g., baroreflex control of Ra and stroke volume) (Fig. 5.7). Moreover, unlike the other baroreflex controllable parameters, the Pa fluctuations caused by HR variability may not be as adequately reflected in the past histories of Pa (and Pth) because of non-causal, parasympathetically mediated respiratory sinus arrhythmia.

Thus, to measure the direct capacitive effects, our general approach is to employ a system identification analysis to six-minute intervals of the beat-to-beat measurements [Ljung, 1999]. This analysis is able to determine the effect of present fluctuation in P_{th} on present fluctuation in P_a) independent of all confounding input variables (past fluctuations in P_{th} and P_a and present and past HR fluctuations). Since system identification is most effective when the input is rich in spectral content, we employ a previous broadband excitation protocol in which the subject breathes according to a sequence of randomly spaced auditory tones (with a mean of five seconds and a range of one to fifteen seconds) [Berger et al., 1989a]. Fig. 5.8 shows that the P_{th} power spectrum of random-interval breathing is much wider than that of spontaneous breathing. Since E_{lv}^{max} may vary (to a small degree) over the six-minute analysis interval due to the

baroreflex [Sagawa et al., 1977], the estimation result reflects the average E_{lv}^{max} value over this interval.

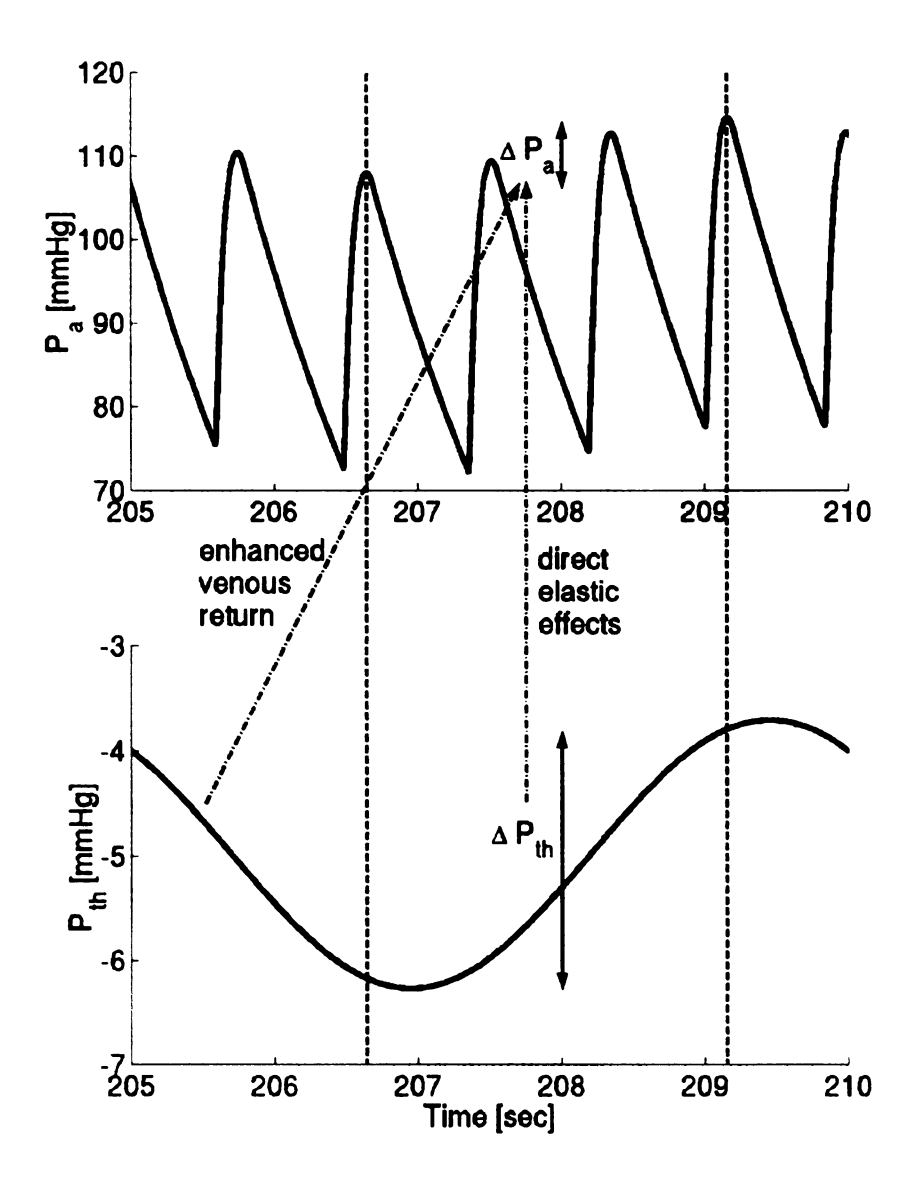


Figure 5.7 Illustration of enhanced venous return phenomenon. In the expiration, P_{th} drops due to the expansion of chest, as a result the venous blood flow back to right atrium increases. Then after a couple of beats, P_a increases. Therefore, P_a changes are not only caused by direct elastic effects, but also by the past history of P_{th}. The phenomenon is dependent on properties of the whole circulation.

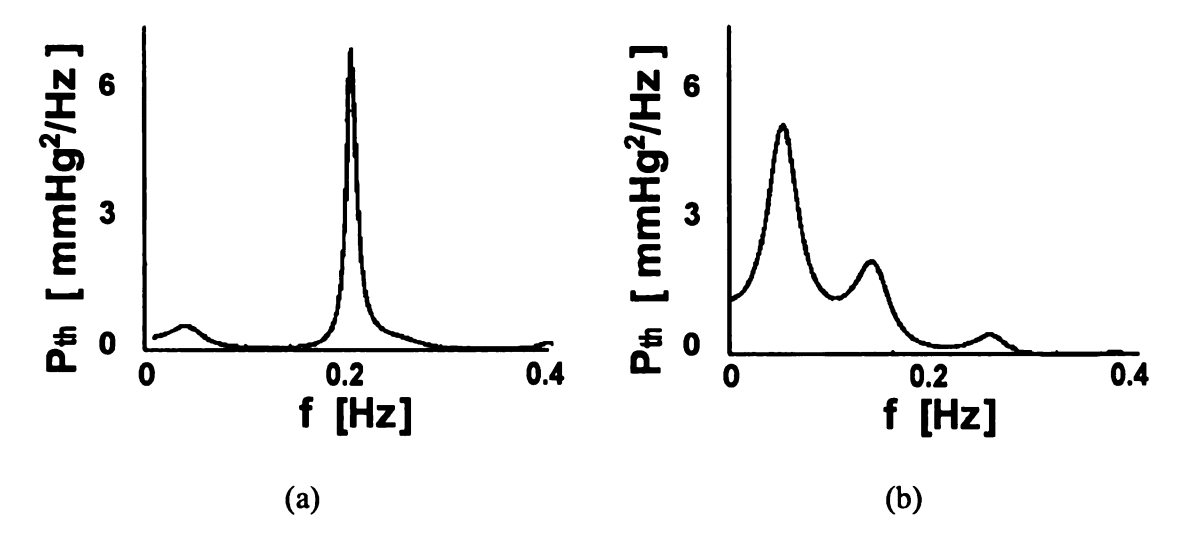


Figure 5.8 Random interval breathing power spectrum (b) is much wider than spontaneous breathing power spectrum (a).

Based on this general approach, we now identify three indices for monitoring E_{lv}^{max} changes. The detailed signal processing steps are outlined below. The signals P_a and respiratory activity in terms of either P_{th} or Q_{lu} are continuously recorded for six minutes during random-interval breathing protocol and digitized at a sampling frequency of 90Hz. Then the pulsatile components (i.e., HR variability) are removed from the P_a signal according to the following steps [Mullen et al., 1997]. First, a pulsatile heart rate (F_p) signal is defined to be a train of unit-area impulses located at the times of ventricular contraction. Then the coupling between P_a and pulsatile F_p is identified based on the following dual-input autoregressive exogenous input (ARX) equation [Perrott et al., 1996]:

$$P_{a}(t) = \sum_{i=1}^{o} a_{i} P_{a}(t-i) + \sum_{i=1}^{p} b_{i} F_{p}(t-i) + \sum_{i=0}^{q} c_{i} R(t-i) + w_{a}(t)$$
 (5.6)

where $R(t) = P_{th}(t)$ or $Q_{lu}(t)$; o, p, and q limit the number of terms in the model (model order); and $w_a(t)$ is an unobserved noise term. This equation includes three sets of unknown parameters $\{a_i, b_i, c_i\}$ whose values are determined by minimizing the variance of the unobserved noise term (linear least squares estimation). The model order is chosen by minimizing the Final Prediction Error (FPE, see Chapter 2). Next, with the newly estimated parameters $\{\hat{a}_i, \hat{b}_i\}$, the blood pressure component due only to pulsatile heart rate is calculated as follows:

$$P_{a}^{F_{p}}(t) = \sum_{i=1}^{o} \hat{a}_{i} P_{a}^{F_{p}}(t-i) + \sum_{i=0}^{p} \hat{b}_{i} F_{p}(t-i).$$
 (5.7)

This portion is finally subtracted from the original blood pressure signal to arrive at the blood pressure component not explained by pulsatile heart rate. That is,

$$P_{a}^{\overline{F_{p}}}(t) = P_{a}(t) - P_{a}^{F_{p}}(t)$$
 (5.8)

To simplify the description, from now on we use Pa to represent the blood pressure signal after removing the pulsatile components.

1) Index h₁

We decimate P_a (without the pulsatile component) and P_{th} into 1.5Hz signals, because the respiratory activity frequencies are much lower than pulsatile activity. Then h_1 (similarly to the above) is estimated based on the following ARX equation:

$$\Delta P_{a}(t) = \sum_{i=1}^{m} a_{i} \Delta P_{a}(t-i) + \sum_{i=0}^{n} b_{i} \Delta P_{th}(t-i) + w(t).$$
 (5.9)

The resulting estimate of the parameter b_0 specifically represents the effects of $\Delta P_{th}(t)$ on $\Delta P_a(t)$ independent of HR and all the other regressor variables in the above equation. Thus, the estimated index h_1 (\hat{h}_1) is b_0 . The process to identify h_1 is shown in Fig. 5.9. The impulse response from P_{th} to P_a (without pulsatile component) is fully defined by the parameters $\{a_i,b_i\}$ and reflect the mechanical effects (i.e., direct capacitive effects and enhance venous return) and sympathetic baroreflex. The direct capacitive effect b_0 is the estimated index h_1 .

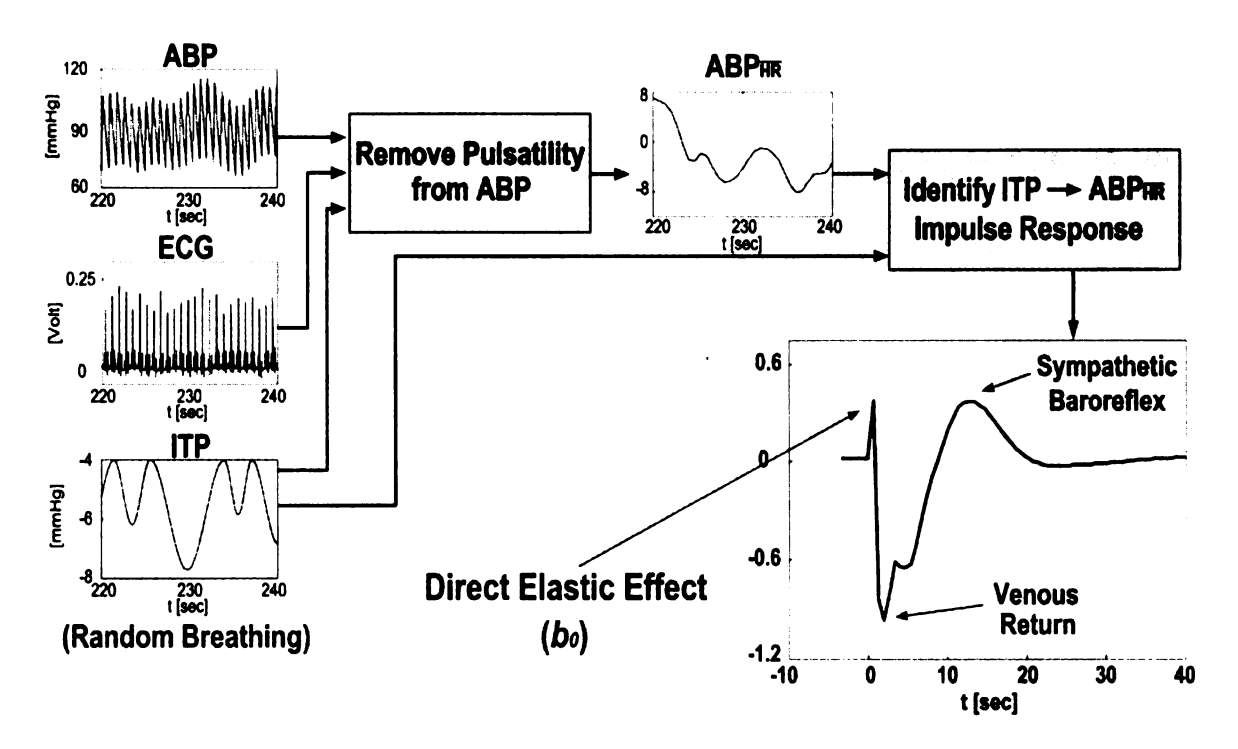


Figure 5.9 Illustration of system identification of index h_1 . First, pulsatility components are removed from P_a ; then P_{th} and the blood pressure after removing pulsatile components are decimated to 1.5Hz. the impulse response from P_{th} to the blood pressure after removing pulsatile components is identified. The estimated h_1 is the value of impulse response at time zero b_0 .

2) Index h₂

We establish four 90Hz signals, P_a^s , P_a^d , P_{th}^s and P_{th}^d , to identify the direct capacitive effects of systole and diastole. For example, the 90Hz P_a^s signal is formed as follows. First, compute the average value of P_a during systole in each beat. Then assign this value as the P_a^s signal in this beat. That is, during one specific beat, P_a^s signal is a constant value. P_a^d , P_{th}^s and P_{th}^d signals are established similarly. Finally, we decimate these four signals into 1.5Hz. To obtain an estimate of the quantity in Eq. 5.2, we identify the following three input ARX equation:

$$\Delta P_a^s(t) = \sum_{i=1}^m a_i \Delta P_a^s(t-i) + \sum_{i=1}^n b_i \Delta P_a^d(t-i) + \sum_{i=0}^q c_i \Delta P_{th}^s(t-i) + \sum_{i=1}^r d_i \Delta P_{th}^d(t-i) + w_s(t). \quad (5.10)$$

The resulting estimate of the parameter c_0 specifically represents the effects of $\Delta P_{th}^s(t)$ on $\Delta P_a^s(t)$ independent of HR and all the other regressor variables in the above equation. Thus, c_0 represents an estimate of the quantity in Eq. 5.2. Similarly, we identify the following equation:

$$\Delta P_{a}^{d}(t) = \sum_{i=1}^{s} e_{i} \Delta P_{a}^{d}(t-i) + \sum_{i=0}^{u} f_{i} \Delta P_{a}^{s}(t-i) + \sum_{i=0}^{v} g_{i} \Delta P_{th}^{d}(t-i) + \sum_{i=0}^{y} p_{i} \Delta P_{th}^{s}(t-i) + w_{d}(t) . (5.11)$$

Here, the g_0 parameter analogously represents an estimate of quantity in Eq. 5.3. Finally, based on Eqs. 5.2 and 5.3, we obtain an estimate of h_2 ($C_a E_{lv}^{max}$) from c_0 and g_0 as follows:

$$\hat{h}_2 = \frac{1 - c_0}{c_0 - g_0}. (5.12)$$

3) Index h₃

We select an initial, physiologic value for τ to obtain an estimate of proportional P_{th} (at 90Hz) from the observed Q_{lu} signal according to Eq. 5.4. Then, we implement the above steps outlined to identify h_2 using the candidate proportional P_{th} signal to estimate c_0 and g_0 . In this case, c_0 and g_0 respectively represent the estimates of the quantities in Eqs. 5.2 and 5.3, each scaled by C_{lu} . We determine an optimal estimate of τ ($\hat{\tau}$) and the ARX parameters by repeating the above steps over physiologic range of τ (e.g. 0.2-1.2 sec) and selecting the resulting parameters that minimizes the joint FPE of Eqs. 5.10 and 5.11. This optimization problem may also be solved efficiently with the Golden Section Search [Wilde et al., 1964]. Finally, we obtain an estimate of h_3 via $\hat{h}_3 = c_0/g_0$.

5.4 Evaluation

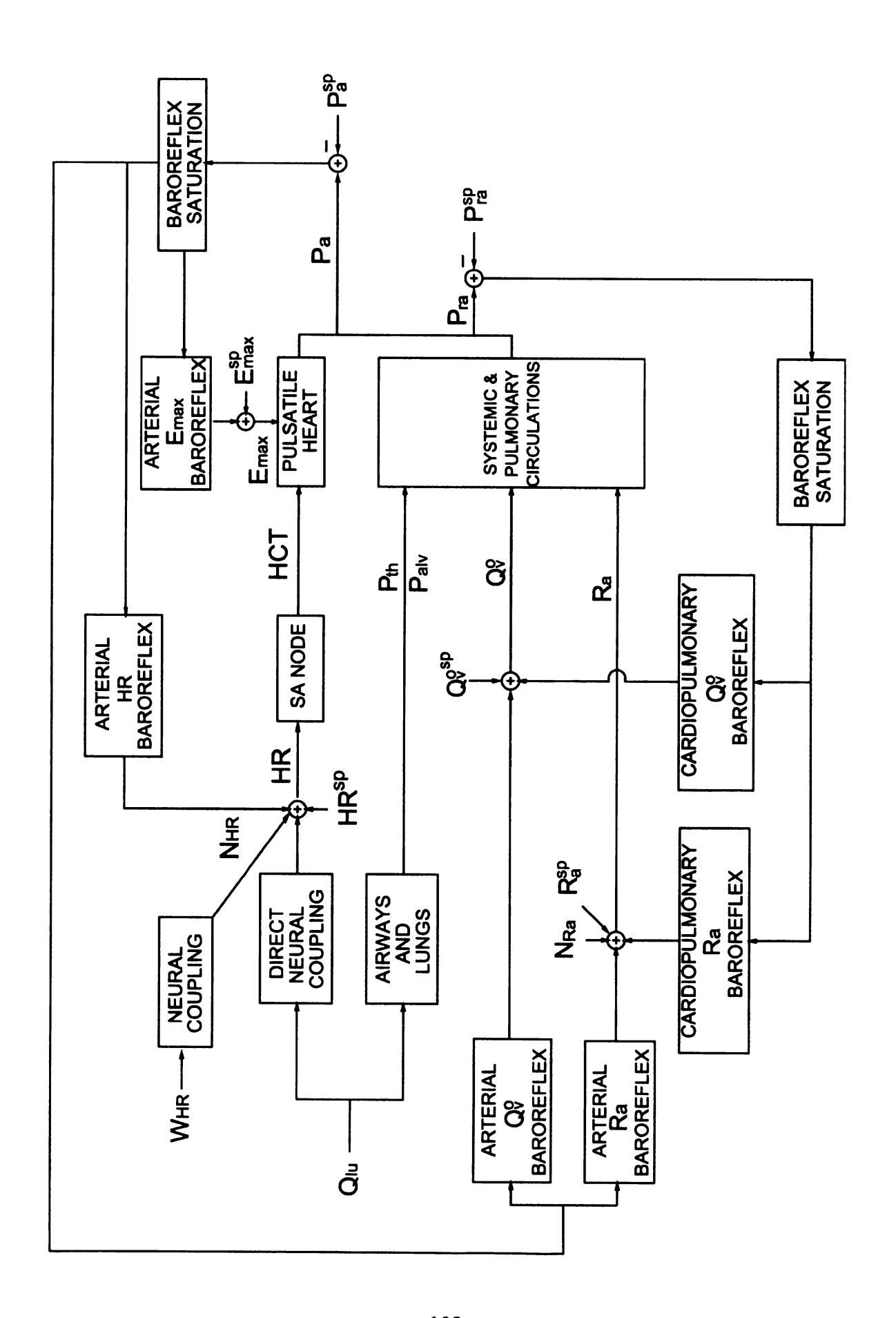
5.4.1 Theoretical Evaluation

We theoretically evaluated the three techniques based on realistic short-term beat-to-beat variability from a human cardiovascular simulator [Mukkamala and Cohen, 2001]. This simulator basically includes three parts: heart and circulation, short-term regulation and resting physiologic perturbations (Fig. 5.10) [Mukkamala et al., 2003b]. The specific aims of our simulation experiments were to determine if 1) the technique as applied to Pa and Pth signals could detect changes in E_{lv}^{max} via h_1 ; 2) the technique as applied to Pa and Pth signals could determine the value of h_2 ($C_a E_{lv}^{max}$) and detect changes in E_{lv}^{max} via h_2 ; and 3) the third technique as applied to Pa and Qtu signals could

determine the value of h_3 and detect changes in $E_{l\nu}^{max}$ via h_3 as well as determine ventilatory constant τ .

To address these specific aims, we conducted over 1000 simulation experiments under different sets of parameter values. For each set of investigated parameter values, we specifically performed the following steps. First, we executed the simulator to obtain six-minute intervals of 90Hz Pa, Pth, and Qlu signals during simulated random-interval breathing. Second, we modeled measurement noise by adding zero-mean Gaussian white noise band-limited within 0.75Hz to each of these signals with a standard deviation (SD) equal to 3% of the SD of the corresponding band-limited signals. Although this SD level was chosen arbitrarily, our results were not significantly altered by at least a doubling of this SD level). Third, we applied these three techniques to the noise corrupted signals. Fourth, we repeated the above three steps 50 times to determine the mean and 95% confidence intervals of each of the estimates (\hat{h}_1 , \hat{h}_2 , \hat{h}_3 and $\hat{\tau}$) according to a Gaussian distribution-based method [Armoundas et al., 2003]. In Eq. 5.6, the orders o=15, p=35, and q=10; in Eq. 5.9, the orders m=n=10; in Eq. 5.10, the orders m=n=q=r=7; in Eq. 5.11, the orders s=u=v=y=2. Once the above steps were completed for all of the investigated parameter value sets, we finally compared the estimated results with corresponding actual E_{lv}^{max} and τ values that we knew exactly.

Figure 5.10 Block diagram summarizing the human cardiovascular simulator (redrawn from Mukkamala, et al., 2003b). It is utilized here as the basis for theoretically evaluating the three techniques. The simulator, which generates realistic beat-to-beat hemodynamic variability, includes a pulsatile heart and circulation, a negative feedback, setpoint (sp) representation of a short-term regulatory system, and resting physiologic perturbations. The blocks in the diagram are mathematically characterized as follows: pulsatile heart and systemic and pulmonary circulations with a lumped parameter system accounting for viscous and volume storage effects; sinoatrial (SA) node with an integrate and fire device; each neural coupling and baroreflex block with impulse responses of varying static gains and system dynamics; baroreflex saturation with arctan functions; and airways and lungs with a lumped parameter system accounting for airway resistance and lung compliance. HR, heart rate; Qo, systemic venous unstressed volume; HCT, HR contraction times; Pra, right atrial pressure. See Figs. 5.5 and 5.6 captions for remaining variable definitions. W_{HR} is 1/f noise (where f is frequency), and N_{HR} is assumed to be an unmeasured, physiologic disturbance to HR. N_{Ra} is band-limited white noise that is assumed to be an unmeasured, physiologic disturbance to Ra.



5.4.2 Pilot Experimental Evaluation

We conducted a pilot experiment in an anesthetized intact canine model. A single adult purpose-bred hound cross dog (25kg) was instrumented as follows. After induction of anesthesia, the animal was intubated but allowed to maintain its own respiratory rate and depth except during certain experimental interventions. The electrocardiogram (ECG), instantaneous lung volume (integral of the airflow), intrathoracic pressure (esophageal pressure), arterial blood pressure (thoracic aortic pressure), and left ventricular pressure were measured. A syringe pump catheter was positioned in the femoral vein for drug administration. The cardio-respiratory measurements were recorded (at a sampling rate of 100Hz and 12-bit resolution) during the following three interventions: 1) baseline; 2) high dose dobutamine (3µg/kg/min i.v.); and 3) lower dose dobutamine (1.5µg/kg/min i.v.). Dobutamine was utilized to increase the left ventricular contractility. Each intervention included a spontaneous breathing period of six minutes followed by a random-interval breathing (with a manual resuscitation bag and a sequence of randomly spaced auditory tones with a mean of five seconds and a range of one to fifteen seconds) period of six minutes. A five to ten minute period of hemodynamic equilibration was allowed between each intervention.

We applied the first technique to the continuous measurements of arterial blood pressure and intrathoracic pressure at 100Hz obtained during the six-minute random-interval breathing period of each intervention. We resampled the signals to 3.3Hz in the second system identification step. In Eq. 5.6, the orders were set as follows: o=15, p=40, and q=10; in Eq. 5.9, the orders were set as m=n=5. Since we were not able to independently determine E_{lv}^{max} , we computed the maximum rate of change of left

ventricular pressure ($|dP_{lv}(t)/dt|_{max}$) as an independent measure of left ventricular contractility for each intervention. We then compared the E_{lv}^{max} changes predicted by index h_1 during the pharmacological interventions with the corresponding reference measure of contractility determined from left ventricular pressure. Note only h_1 was predicted because other indices were less sensitive to the changes in E_{lv}^{max} .

5.5 Evaluation Results

5.5.1 Theoretical Evaluation Results

Fig. 5.11 summarizes the theoretical evaluation results of the technique as applied to realistic simulated signals. All of the estimated quantities are shown in terms of their mean (x) and 95% confidence intervals (bar).

Fig. 5.11a shows the estimation results of the index h_1 as the technique is applied on the P_a and P_{th} signals during random-interval breathing. This figure specifically illustrates the estimated index h_1 (\hat{h}_1) plotted against the corresponding actual simulator value of E_{lv}^{max} . These results indicated that this technique was able to detect changes in E_{lv}^{max} as small as 10%.

Fig. 5.11b shows the h_2 estimation results of the technique applied on the P_a and P_{th} signals during random-interval breathing but with a more sophisticated analysis so as to provide more precise quantitative information. This figure specifically illustrated the estimated index h_2 (i.e., $C_a E_{lv}^{max}$) plotted against the corresponding actual simulator value of E_{lv}^{max} . The circles in the figure indicate the actual h_2 simulator value. These

results demonstrate that our technique was able to determine $C_a E_{lv}^{max}$ with little estimation bias (close correspondence between crosses and circles). However, its sensitivity in detecting changes in E_{lv}^{max} is reduced with respect to the estimation of h_1 due to the increased mathematical complexity.

Fig. 5.11c and 5.11d show the h_3 estimation results of the technique applied on the Pa and Q_{lu} signals during random-interval breathing. In contrast to the first two estimation methods, this method could be employed in practice with totally non-invasive measurements. These two figures specifically illustrate the resulting \hat{h}_3 and $\hat{\tau}$ (an estimate of τ =R_{air}C_{lu}) respectively against the corresponding actual E_{lv}^{max} and R_{air} values. The circles in the figures indicate the actual simulator values for the h_3 and τ respectively. These results demonstrate that the technique was able to estimate each of these quantities with small bias and detect actual changes in both E_{lv}^{max} and R_{air}. However, its sensitivity in detecting E_{lv}^{max} changes is the least amongst the three techniques, as it is the most complex.

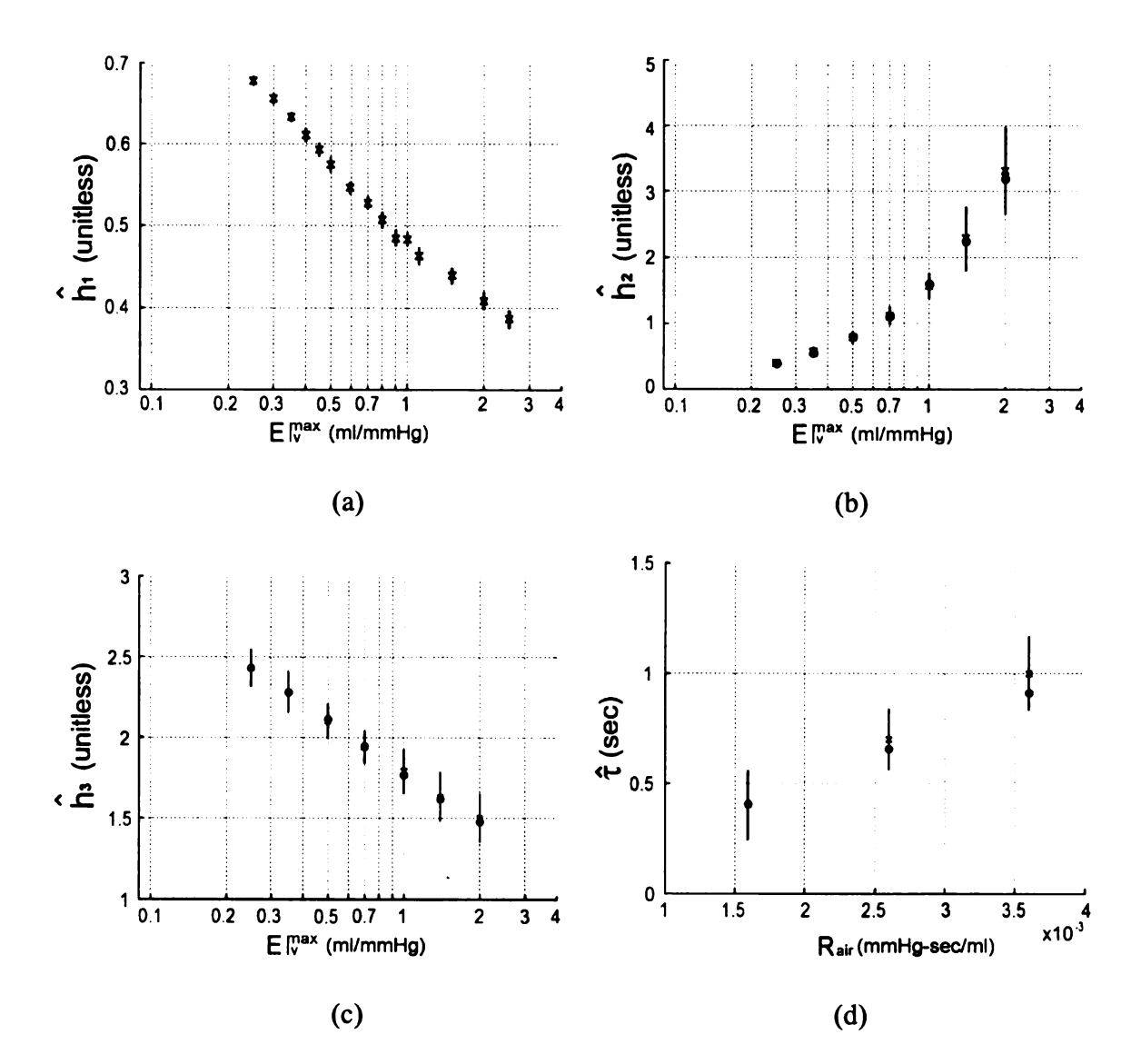


Figure 5.11 Summary of theoretical evaluation results. The results are obtained by applying the technique to realistic beat-to-beat variability generated by the human cardiovascular simulator in Fig. 5.10. All of the estimated quantities are shown in terms of their mean (x) and 95% confidence intervals (bar), whereas the corresponding actual simulator values are indicated with circles. See Figs. 5.5 and 5.6 captions for variable definitions. (a), \hat{h}_1 (an estimate of a lumped index reflecting Eqs. 5.2 and 5.3) is plotted against the corresponding actual simulator E_{lv}^{max} value. (b), \hat{h}_2 (an estimate of $C_a E_{lv}^{max}$) is plotted against the corresponding actual simulator E_{lv}^{max} value. (c), \hat{h}_3 (an estimate of h_3 in Eq. 5.5) is plotted against the corresponding actual E_{lv}^{max} simulator value. (d), $\hat{\tau}$ (an estimate of $\tau = R_{air}C_{lv}$) is plotted against R_{air} .

5.5.2 Pilot Experimental Evaluation Results

Fig. 5.12a shows example segments of the measured left ventricular and arterial blood pressure waveforms obtained during baseline and high dose dobutamine conditions. Fig. 5.12b shows example segments of changes in the measured intrathoracic pressure waveform during spontaneous (negative-pressure) breathing and randominterval (positive-pressure) breathing. This figure demonstrates that the canine respiratory pattern can indeed be randomized manually with a resuscitation bag.

Fig. 5.13 shows the contractility changes predicted by the two methods. The cross represents the value of the predicted h_1 (\hat{h}_1), and the circle represents the value of dP_{lv}/dt , and the bars represent the standard deviation. The extent of \hat{h}_1 increase from high dose to low dose dobutamine is more significant than the decrease of the value of $|dP_{lv}(t)/dt|_{max}$. These pilot results demonstrate that our technique may predict more precisely left ventricular contractility changes than the more invasive method.

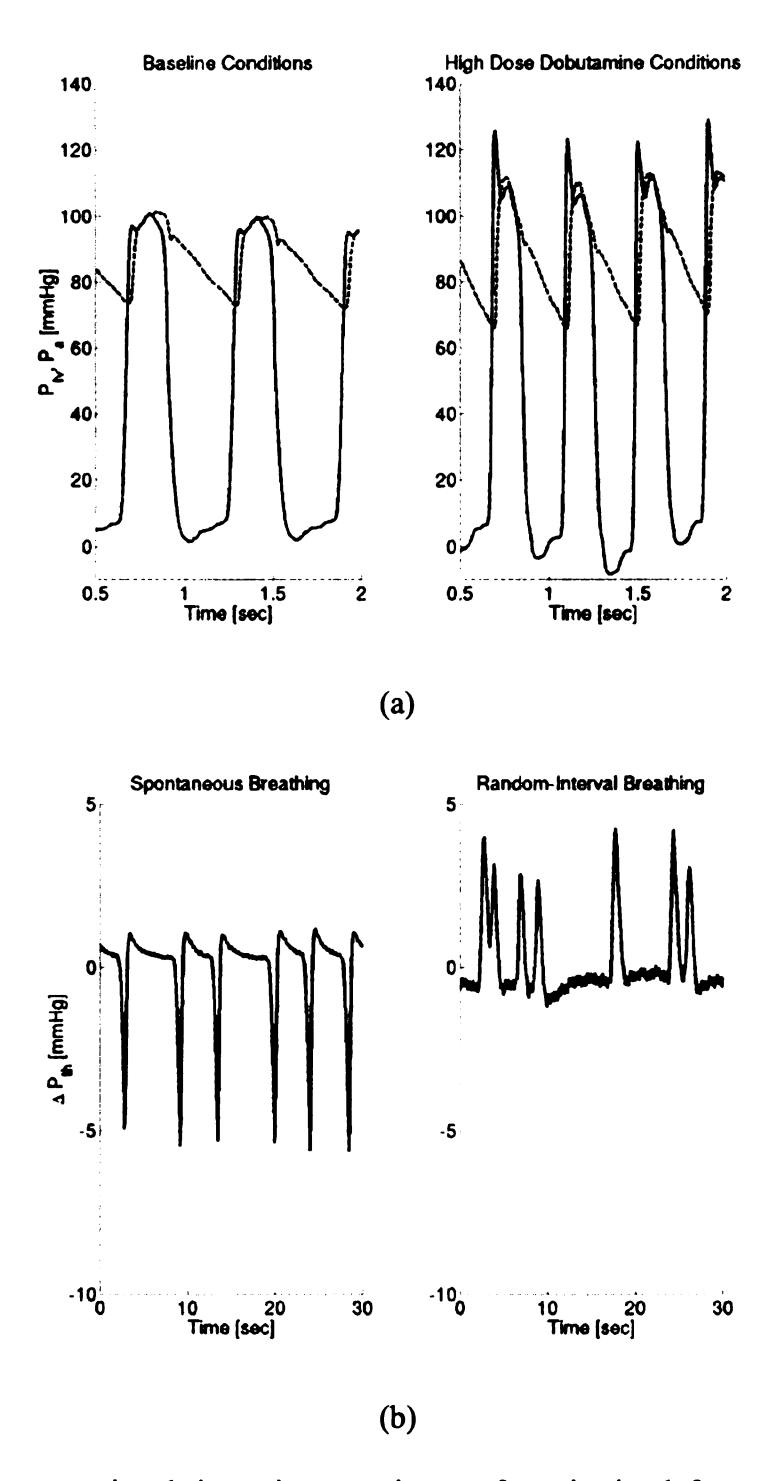


Figure 5.12 Pressure signals in canine experiment of monitoring left ventricular contractility. (a), comparison of left ventricular pressure (P_{lv}) and a random a pressure (P_a) in control and high dobutamine conditions. P_{lv} : solid line, P_a : dash line. (b), comparison of ΔP_{th} during spontaneous negative breathing and random-interval positive breathing.

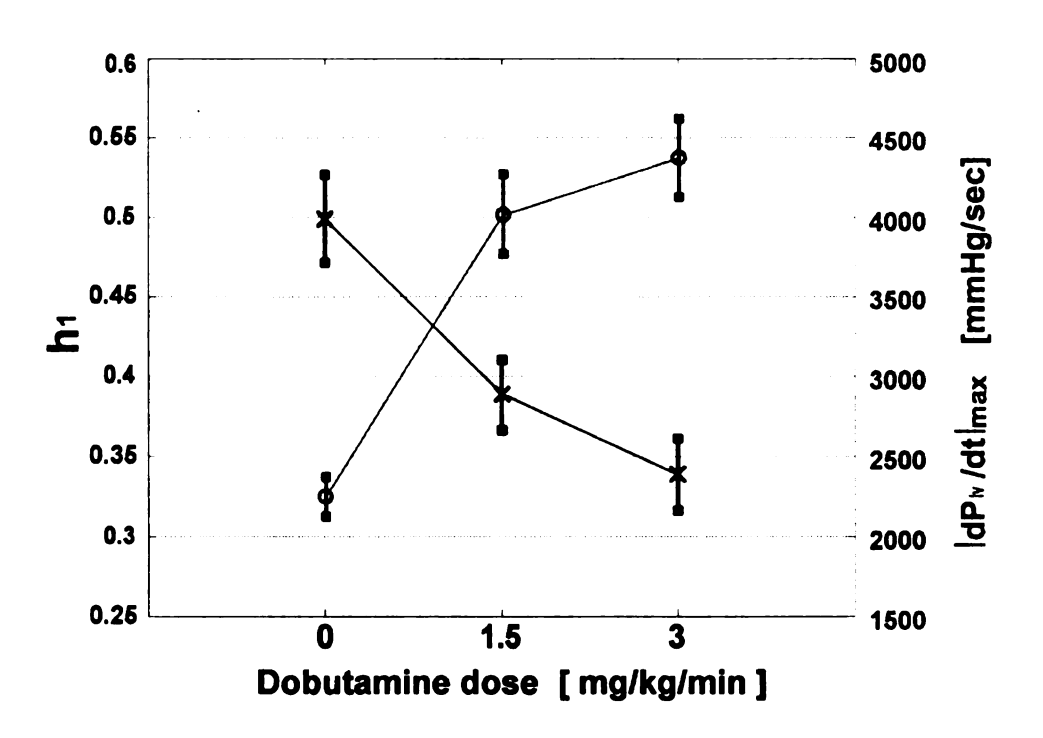


Figure 5.13 Comparison of our technique with a highly invasive measurement of canine experiment. Estimated index \hat{h}_1 and $|dP_{lv}(t)/dt|_{max}$ plotted against dobutamine dose. The estimated quantities \hat{h}_1 are shown in terms of their mean (x) and standard deviation (bar). The measured quantities $|dP_{lv}(t)/dt|_{max}$ are shown in terms of their mean (o) and standard deviation (bar). When more dobutamine is injected, contractility increases, thus h_1 should decrease and $|dP_{lv}(t)/dt|_{max}$ should increase. However, \hat{h}_1 is more sensitive than $|dP_{lv}(t)/dt|_{max}$.

5.6 Discussion

To formulate the technique, we restricted its applicability to patients without aortic stenosis and did not model both inertial and distribution effects in arterial tree. While inertial effects contribute to the detailed structure of Pa waveforms within a beat, they are relatively insignificant in accounting for the slow beat-to-beat variations that are considered here. For example, even if cardiac output increased by 50% from one beat to the next, the Pa waveform in Fig. 5.5a would be in error by 0.5mmHg (inductance of blood is typically ~0.015mmHg.s2/ml [Gurarini et al., 1998]). It is likewise known that distributed effects (e.g., wave reflections in peripheral Pa waveforms) do not confound slow beat-to-beat variations [Noordergraaf, 1978]. This may be understood by considering the limiting case in which the time scales are sufficiently long (i.e., slow changes) such that the wavelengths of the propagating waves are much longer than the dimension of the arterial tree. Under these circumstances, the arterial tree may be well represented by the lumped model in Fig. 5.5a. Importantly, this implies that beat-to-beat variability in Pa waveform is not significantly dependent on the site of its measurement in the arterial tree. We also did not model these fast effects in the ventilatory system (Fig. 5.6), as similar arguments may likewise hold [Staub, 1991].

However, in considering the identification of the second and third indices, the inertial and distribution effects in real experimental data does introduce difficulties. The dicrotic notch which denotes aortic valve closure is apparent in central arterial blood pressure waveform and could be utilized to identify the systolic and diastolic intervals. While in the readily available peripheral Pa waveform the dicrotic notch is not apparent due to distributed and viscous effects. It may be possible to determine the systolic and

diastolic intervals based on the cardiac cycle length using, for example, the well-known Bazett formula [Bazett, 1920]. Alternatively, it may only be necessary to identify a single systolic Pa and diastolic Pa sample for each beat. Studies with the human cardiovascular simulator have shown that this approach does not materially affect our results.

Index h_2 ($C_a E_{lv}^{max}$) can be utilized to estimate the ventriculo-arterial energy coupling. h_2 is closely related to E_{lv}^{max} / E_a^{eff} , where E_a^{eff} is the effective arterial elastance characterizing both the viscous and capacitive properties of the arteries [Sunagawa et al., 1983], not the reciprocal of C_a . The quantity E_{lv}^{max} / E_a^{eff} is a useful index of ventriculo-arterial coupling [Chang et al., 1997; Sunagawa et al., 1983], and may be essential for optimizing chronic heart failure therapy [Binkley et al., 1990]. h_2 may be utilized to measure the value of E_{lv}^{max} if C_a is calibrated by the technique described in Chapter 3.

In order to improve the efficiency of the system identification algorithm, a random-interval breathing protocol is employed. However it is difficult for those severe patients. The random-interval breathing then could be realized by a programmed ventilator. Therefore the monitoring of E_{lv}^{max} could be performed continuously. In the left ventricle and artery model in Fig. 5.5a, we assumed X is equal to 1/3. Actually, we simulated with X varying from 0.25 to 0.4 and applied the technique on the data. The results suggest that the value of X only affects the estimation results a little.

The results of this theoretical study indicate that the sensitivity in detecting changes in E_{lv}^{max} is best when Pa and the somewhat invasive P_{th} signals are available for analysis.

However, if only P_a and the non-invasive Q_{lu} are available, an estimate of the ventilatory system time constant $\tau = R_{air}$ C_{lu} may also be obtained. Both R_{air} and C_{lu} can vary in heart failure patients as a result of pulmonary edema. Thus, the τ estimate may possibly be utilized as a quantitative index of pulmonary edema. However, in pulmonary edema, we note that R_{air} may increase while C_{lu} decreases. The estimate of τ may therefore be more useful in which only one of these parameters is altered (e.g., asthma). This is significant to the extent that τ here may potentially be measured non-invasively.

The precise theoretical evaluation could not be achieved in an experimental model in which all of the actual parameter values would be difficult to ascertain. The theoretical validation here indeed justifies and promotes experimental testing of the technique against the traditional method for measuring E_{lv}^{max} during different levels of ventricular contractile state.

In the pilot animal experiment, the h₁ estimates were obtained with an invasive aortic blood pressure waveform. However, we contend that the estimates would not be significantly altered, if a less invasive peripheral blood pressure waveform were measured, because these two waveforms are similar on slow, beat-to-beat time scales. One difference from the theoretical evaluation is that we only were able to increase the contractility, while our technique works better when the contractility is small.

In summary, we present a novel technique to monitor the changes in left ventricular contractility in terms of E_{lv}^{max} from only respiratory-induced P_a variations obtained during a random-interval breathing protocol. The validation based on the simulated data and the pilot animal study shows the promise of the technique. With experiments on

animals and even humans in which the absolute values of E_{lv}^{max} are measured, this technique may be potentially utilized in clinical practice to help guide therapy in heart failure patients.

CHAPTER 6

CONCLUSIONS

6.1 Summary

In this thesis, we introduced three novel techniques to monitor three hemodynamic parameters, CO, LAP and left ventricular contractility in terms of E_{lv}^{max} by mathematical analysis of long time intervals of blood pressure waveforms. First, we refined a previously developed technique for continuously monitoring CO from a peripheral ABP waveform and validated it, for the first time, in humans. Second, we extended the first technique to a PAP or RVP waveform to continuously monitor both LAP and CO and evaluated it in ICU patients and a canine experiment. Third, we introduced a technique for monitoring changes in E_{lv}^{max} from peripheral ABP waveform variability induced by random-interval respiratory activity and evaluated it with respect to data sets generated from a realistic human cardiovascular simulator and a canine experiment. Each of these techniques estimate the hemodynamic parameters using system identification method combined with physiologic knowledge. The advantages of these techniques over conventional methods are that they may be realized in a less invasive, continuous, and/or safer manner. The preliminary evaluations with respect to hemodynamic data obtained from realistic computer simulations, animal subjects, human volunteers, and patients demonstrate that these techniques may indeed be capable of accurately estimating CO, LAP and E_{lv}^{max} with an acceptable accuracy in clinic. Table 6.1 summarizes the developed techniques.

Table 6.1 Summary of three hemodynamic monitoring techniques. These techniques analyze long time intervals of blood pressure waveforms using system identification combined with physiologic knowledge and are validated with different sets of experimental data.

Objectives	Measurements	Physiologic Knowledge	Advantage	Validation
СО	Peripheral ABP	Windkessel model can represent arterial tree in a long time scale	Less invasive, continuous	Healthy volunteers, ICU patients
CO, LAP	PAP or RVP	Windkessel model can represent pulmonary artery in a long time scale	Continuous, safer	ICU patients, dog experiment
E max	ABP, Pth or Qlu	Direct elastic effects	Less invasive	Simulated data, dog experiment

6.2 Future Work

This thesis does not signify an end but only a beginning. I have come to realize that there are several areas of future investigation that would be worthwhile. First, a universal model order selection criterion for both the first and second techniques is needed.

Learning methods may be one possible option. We can also try to use the OE model instead of ARX model to optimize full prediction. Second, it is very important to develop an algorithm to identify the artifact-free segments from ABP and PAP waveforms in order to have a truly automatic technique. Of course, a large number of high quality experimental measurements (both pressure waveforms and gold standard reference measurements) from animals and humans under different physiologic conditions are required to further evaluate and improve the techniques.

By the end of my thesis work, I also formulated a new technique to compute $C_a E_{lv}^{max}$ and therefore quantitatively monitor changes in E_{lv}^{max} . The advantage of this technique is that it does not require random-interval breathings, but it does need an invasive measurement of a ortic pressure. More specifically, according the two-compartment left ventricle and arterial tree model (Fig. 5.5), blood flow Qa to a orta is given by:

$$Q_a = C_a \frac{dP_a(t)}{dt} + \frac{P_a(t)}{R_a}.$$
 (6.1)

Since the volume of left ventricle is $C_{lv}(t)P_{lv}(t)$, the blood flow Q_{lv} from left ventricle is given by:

$$Q_{lv}(t) = \frac{d(C_{lv}(t)P_{lv}(t))}{dt} = \frac{dC_{lv}(t)}{dt}P_{lv}(t) + C_{lv}(t)\frac{dP_{lv}(t)}{dt}.$$
 (6.2)

During the ejection phase, assuming $R_{lv}=0$ (no aortic stenosis), $P_{lv}(t)=P_a(t)$, and $Q_{lv}(t)=-Q_a(t)$. Thus,

$$\frac{dC_{lv}(t)}{dt}P_a(t) + C_{lv}(t)\frac{dP_a(t)}{dt} = -\left(C_a\frac{dP_a(t)}{dt} + \frac{P_a(t)}{R_a}\right). \tag{6.3}$$

At the time t_{m} when E_{lv} reaches its maximum value $\,E_{lv}^{\,\text{max}}$, C_{lv} reaches its minimum

value. Then $C_{lv}(t_m) = \frac{1}{E_{lv}^{max}}, \frac{dC_{lv}(t_m)}{dt} = 0$. Substituting these two values into Eq.

6.3, we finally arrive at a simple equation for proportional E_{lv}^{max} :

$$C_{a}E_{lv}^{max} = \frac{-1}{1 + \frac{P_{a}(t_{m})}{R_{a}C_{a}\frac{dP_{a}(t_{m})}{dt}}}.$$
 (6.4)

Because t_m is not generally at the time of end-ejection [Sagawa, 1981], we would need to find a method to determine it. Once t_m is determined, $C_a E_{lv}^{max}$ could be computed at t_m using Eq. 6.4 without measuring left ventricular pressure and volume. As described in Chapter 5, C_a is nearly a constant over a long time period, thus Eq. 6.4 could be utilized to monitor changes in E_{lv}^{max} . Here, RaCa could be computed using the method of Chapter 3 or direct exponential fitting. Note that C_a can be obtained with an additional measurement of stroke volume or blood flow (e.g., flow probe, thermodilution, Doppler ultrasound) and therefore the absolute value of E_{lv}^{max} could be computed.

It is our hope that this thesis sparks these future investigations and ultimately leads to new hemodynamic monitoring systems in hospitals, at home, and with implanted devices.

BIBLIOGRAPHY

- 1. Adamson PB, Magalski A, Braunschweig F, Bo"hm M, Reynolds D, Steinhaus D, et al. Ongoing Right Ventricular Hemodynamics in Heart Failure: Clinical Value of Measurements Derived From an Implantable Monitoring System. *J. Am. Coll. Cardiol.*, 41:565-71, 2003.
- 2. Akselrod S, Gordon D, Madwed JB, Snidman NC, Shannon DC, and Cohen RJ. Hemodynamic regulation: investigation by spectral analysis. *Am. J. Physiol.*, 249: H867-875, 1985.
- 3. Akselrod S, Gordon D, Ubel FA, Shannon DC, Barger AC, and Cohen RJ. Power spectrum analysis of heart rate fluctuation: a quantitative probe of beat-to-beat cardiovascular control. *Science*, 213:220-222, 1981.
- 4. Armoundas AA, Feldman AB, Mukkamala R, Bin H, Mullen TJ, Belk PA, et al. Statistical accuracy of a moving equivalent dipole method to identify sites of origin of cardiac electrical activation. *IEEE Trans. Biomed. Eng.*, 50(12): 1360-1370, 2003.
- 5. Barcroft H, Edholm OG, McMicheal J, and Sharpey-Schafer EP. Post haemorrhagic fainting study by cardiac output and forearm flow. *The Lancet*, i:489-491, 1944.
- 6. **Bazett HC.** An analysis of the time-relations in electrocardiograms. *Heart*, 7:353-370, 1920.
- 7. Berger RD, Saul JP, and Cohen RJ. Assessment of autonomic response by broadband respiration. *IEEE Trans. Biomed. Eng.*, 36(11):1061-1065, 1989a.
- 8. Berger RD, Saul JP, and Cohen RJ. Transfer function analysis of autonomic regulation. I. Canine atrial rate response. *Am. J. Physiol.*, 256: H142-H152, 1989b.
- 9. Berne RM and Levy MN. Physiology. Mosby, Inc., St. Louis, Missouri, 1998.
- 10. Binkley PF, Van Fossen DB, Nunziata B, Unverferth DV, and Leier CV. Influence of positive inotropic therapy on pulsatile hydraulic load and ventricular-vascular coupling in congestive heart failure. *JACC*, 15(5):1127-1135, 1990.
- 11. Bourgeois MJ, Gilbert BK, von Bernuth G, and Wood EH. Continuous determination of beat-to-beat stroke volume from aortic pressure pulses in the dog. *Circ. Res.*, 39(1):15-24, 1976.

- 12. **Burkhoff D.** The conductance method of left ventricular volume estimation. *Circulation*, 81(2):703-706, 1990.
- 13. Burkhoff D, Sugiura S, Yue D, and Sagawa K. Contractility-dependent curvilinearity of end-systolic pressure-volume relations. *Am. J. Physiol.*, 252:H1218-H1227, 1987.
- 14. Burkhoff D and Sagawa K. Ventricular efficiency predicted by an analytical model. Am. J. Physiol., 250(19): R1021-R1027, 1986.
- 15. Cerutti C, Gustin MP, Molino P, and Paultre CZ. Beat-to-beat stroke volume estimation from aortic pressure waveform in conscious rats: Comparison of models. *Am. J. Physiol.*, 281:H1148-H1155, 2001.
- 16. Chakko S, Woska D, et al. Clinical, radiographic and hemodynamic correlations in the chronic congestive heart failure: conflicting results may lead to inappropriate care. Am. J. Med., 90:353-359, 1991.
- 17. Chang KC and Kuo TS. Single-beat estimation of the ventricular pumping mechanics in terms of the systolic elastance and resistance. *J. Theor. Biol.*, 189:89-95, 1997.
- 18. Chen CH, Fetics B, Nevo E, Rochitte CE, Chiou KR, Ding PYA, et al. Noninvasive single-beat determination of left ventricular end-systolic elastance in humans. *JACC*, 38(7):2028-2034, 2001.
- 19. Critchley LAH and Critchley JAJH. A meta-analysis of studies using bias and precision statistics to compare cardiac output measurement techniques. *J. Clin. Monit. Comput.*, 15:85-91, 1999.
- 20. Critchley LAH. Impedance cardiography: the impact of new technology. *Anaesthesia*, 53: 677-684, 1998.
- 21. **Diamond GA and Jacob C.** Noninvasive prediction of pulmonary-capillary wedge pressure. *N. Engl. J. Med.*, 328(19):1423-1424, 1993.
- 22. Dokainish H, Zoghbi WA, Lakkis NM, Al-Bakshy F, Dhir M, Quinones MA, et al. Optimal noninvasive assessment of left ventricular filling pressures: A comparison of tissue Doppler echocardiography and B-type Natriuretic Peptide in patients with pulmonary artery catheters. *Circulation*, 109: 2432-2439, 2004.
- 23. **Eckberg DL.** Respiratory sinus arrhythmia: a window on central autonomic regulation in man. In: *The Peripheral Circulation*, edited by Hunyor S, Ludbrook J, and Shaw J, et al. Amsterdam: Elsevier Science Publishers, 1984, p. 267-274.

- 24. Ehlers KC, Mylrea KC, Waterson CK, and Calkins JM. Cardiac output measurements: a review of current techniques and research. *Ann. Biomed. Eng.*, 14(3): 219-239, 1986.
- 25. Elstad M, Toska K, Chon KH, Raeder EA, and Cohen RJ. Respiratory sinus arrhythmia: opposite effects on systolic and mean arterial pressure in supine humans. Am. J. Physiol., 536(1):251-259, 2001.
- 26. Eriksen M, Walloe L. Improved method for cardiac output determination in man using ultrasound Doppler technique. *Med. Biol. Eng. Comput.*, 28: 555-560, 1990.
- 27. Erlanger J and Hooker DR. An experimental study of blood-pressure and of pulse-pressure in man. *Bull Johns Hopkins Hosp.*, 12:145-378, 1904.
- 28. Freeman GL, Little WC, and O'Rourke RA. The effect of vasoactive agents on the left ventricular end-systolic pressure-volume relation in closed-chest dogs. *Circulation*, 74(5): 1107-1113, 1986.
- 29. Gerhardt UMW, Scholler C, Bocker D, and Hohage H. Non-invasive estimation of cardiac output in critical care patients. J. Clin. Monit., 16:263-268, 2001.
- 30. Gratz I, Kraidin J, Jacobi AG, deCastro NG, Spagna P, and Larijani GE. Continuous noninvasive cardiac output as estimated from the pulse contour curve. *J. Clin. Monit.*, 8: 20-27, 1992.
- 31. Gurarini M, Urzúa J, Cipriano A, and González W. Estimation of cardiac function from computer analysis of the arterial pressure waveform. *IEEE Trans. Biomed. Eng.*, 45(12):1420-1428, 1998.
- 32. **Guyton AC and Hall JE.** *Textbook of Medical Physiology*. Philadelphia: W. B. Saunders Company, 1996.
- 33. Hallock P and Benson JC. Studies on the elastic properties of human isolated aorta. Am. J. Physiol., 16:595-602, 1937.
- 34. Houtman S, Oeseburg B, and Hopman MT. Non-invasive cardiac output assessment duringmoderate exercise: pulse contour compared with CO₂ rebreathing. *Clin. Physiol.*, 19:230-237, 1999.
- 35. Imholz BPM, Wieling W, van Montfrans GA, and Wesseling KH. Fifteen years experience with finger arterial pressure monitoring: assessment of the technology. *Cardiovasc. Res.*, 38: 605-616, 1998.
- 36. Iwase T, Tomita T, Miki S, Nagai K, and Murakami T. Slope of the end-systolic pressure-volume relation derived from single beat analysis is not always sensitive to positive inotropic stimuli in humans. *Am. J. Cardiol.*, 69: 1345-1353, 1992.

- 37. Kass DA, Yamazaki T, Burkhoff D, Maughan WL, and Sagawa K. Determination of left ventricular end-systolic pressure-volume relationships by the conductance (volume) catheter technique. *Circulation*, 73(3): 586-595, 1986.
- 38. Kass DA, Midei M, Graves W, Brinker JA, and Maughan WL. Use of a conductance (volume) catheter and transient inferior vena cava occlusion for rapid determination of pressure-volume relationships in man. Cathet. Cardiovasc. Diagn., 15: 192-202, 1988.
- 39. Kass DA, Beyar R, Lankford E, Heard M, Maughan WL, and Sagawa K. Influence of contractile state on curvilinearity of in situ end-systolic pressure-volume relations. *Circulation*, 79(1):167-178, 1989.
- 40. Katz AM. Physiology of the Heart. New York: Raven Press, 1992.
- 41. **Kjørstad KE, Korvald C, and Myrmel T.** Pressure-volume-based single-beat estimations cannot predict left ventricular contractility *in vivo. Am. J. Physiol.*, 282: H1739-H1750, 2002.
- 42. Lawson HC. The volume of blood: a critical examination of methods for its measurement. In: *Handbook of Physiology*, First edition, Section 2, Circulation, Volume I, Chapter 3, edited by Bethesda. American Physiological Society, 1962.
- 43. Leatherman JW and Shapiro RS. Overestimation of pulmonary artery occlusion pressure in pulmonary hypertension due to partial occlusion. *Crit. Care Med.*, 31(1): 93-97, 2003.
- 44. Levett JM and Replogle RL. Thermodilution cardiac output: a critical analysis and review of the literature. J. Surg. Res., 27:392-404, 1979.
- 45. Linton NWF and Linton RAF. Estimation of changes in cardiac output from the ABP waveform in the upper limb. Br. J. Anaesth., 86:486-496, 2001.
- 46. **Ljung L.** System Identification: Theory for the User. Englewood Cliffs, NJ: Prentice Hall, 1999.
- 47. Marik P, Heard SO, and Varon J. Interpretation of the pulmonary artery occlusion (wedge) pressure: physicians' knowledge versus the experts' knowledge. *Crit. Care Med.*, 26(10):1761-1763, 1998.
- 48. Marino PL. The ICU Book. Baltimore: Williams & Wilkins, 1998.
- 49. Martin JF, Volfson LB, Kirzon-Zolin VV, and Schukin VG. Application of pattern recognition and image classification techniques to determine continuous

- cardiac output from the arterial pressure waveform. *IEEE Trans. Biomed. Eng.*, 41(10): 913-920, 1994.
- 50. McIntyre K, Vita J, Lambrew C, Freeman J, and Loscalzo J. A noninvasive method of predicting pulmonary-capillary wedge pressure. N. Engl. J. Med., 327:1715-1720, 1992.
- 51. Moody GB and Mark RG. A database to support development and evaluation of intelligent intensive care monitoring. *Comput. Cardiol.*, 23: 657-660, 1996.
- 52. Moody GB, Mark RG, and Goldberger AL. PhysioNet: a web-based resource for study of physiologic signals. *IEEE Eng. Med. Biol. Mag.*, 20(3): 70-75, 2001.
- 53. Morris AH, Chapman RH, and Gardner RM. Frequency of technical problems encountered in the measurement of pulmonary artery wedge pressure. *Crit. Care Med.*, 12(3): 164-170, 1984.
- 54. Mukkamala R, Mathias JM, Mullen TJ, Cohen RJ, and Freeman R. System identification of closed-loop cardiovascular control mechanisms: Diabetic autonomic neuropathy. Am. J. Physiol., 276(45): R905-R912, 1999.
- 55. Mukkamala R and Cohen RJ. A forward model-based validation of cardiovascular system identification. *Am. J. Physiol.*, 281: H2714-H2730, 2001.
- 56. Mukkamala R, Reisner AT, Hojman HM, Mark RG, and Cohen RJ. Continuous cardiac output monitoring by peripheral blood pressure waveform analysis. *Comput. Cardiol.*, 30: 281-284, 2003a.
- 57. Mukkamala R, Toska K, and Cohen RJ. Noninvasive identification of the total peripheral resistance baroreflex. Am. J. Physiol., 284: H947–H959, 2003b.
- 58. Mukkamala R, Kuiper J, Ahmad S, and Lu Z. Cardiac output monitoring in intensive care patients by radial artery pressure waveform analysis. *IEEE*, *EMBC*, 2:3712 3715, 2004.
- 59. Mukkamala R, Reisner AT, Hojman HM, Mark RG, and Cohen RJ. Continuous cardiac output monitoring by peripheral blood pressure waveform analysis. *IEEE Trans. Biomed. Eng.*, 53(3): 459-467, 2006.
- 60. Mullen TJ, Appel ML, Mukkamala R, Mathias JM, and Cohen RH. System identification of closed-loop cardiovascular control: Effects of posture and autonomic blockade. *Am. J. Physiol.*, 272: H448-H461, 1997.
- 61. **Nishimura RA and Tajik AJ.** Evaluation of diastolic filling of left ventricle in health and disease: Doppler echocardiography is the clinician's Rosetta Stone. *J. Am. Coll. Cardiol.*, 30: 8-18, 1997.

- 62. Noordergraaf A. Circulatory System Dynamics. New York: Academic Press, 1978.
- 63. Omboni S, Parati G, Fratola A, Mutti E, DiRienzo M, Castiglioni P, et al. Spectral and sequence analysis of finger blood pressure variability: Comparison with analysis of intra-arterial recordings. *Hypertension*, 22: 26-33, 1993.
- 64. Osborn JJ, Russell JAG, Beaumont J, deLanerolle P, McChesney B, and Garfield F. The measurement of relative stroke volume from a ortic pulse contour pulse pressure. *Vasc. Dis.*, 5(3): 165-177, 1968.
- 65. **Perrott MH and Cohen RJ.** An efficient approach to ARMA modeling of biological systems with multiple inputs and delays. *IEEE Trans. Biomed. Eng.*, 43(1):1-14, 1996.
- 66. **Pinsky MR and Vincent JL.** Let us use the pulmonary artery catheter correctly and only when we need it. *Crit. Care Med.*, 33(5): 1119–1122, 2005
- 67. Rapoport J, Teres D, Steingrub J, Higgins T, McGee W, and Lemeshow S. Patient characteristics and ICU organizational factors that influence frequency of pulmonary artery catheterization. *JAMA*, 283(19): 2559-2567, 2000.
- 68. **Redling JD and Akay M.** Noninvasive cardiac output estimation: A preliminary study. *Biol. Cybern.*, 77: 111-122, 1997.
- 69. Remington JW and Hamilton WF. The construction of a theoretical cardiac ejection curve from the contour of the aortic pressure pulse. Am. J. Physiol., 144: 546-556, 1945.
- 70. Ristuccia HL, Grossman P, Watkins LL, and Lown B. Incremental bias in Finapres estimation of baseline blood pressure levels over time. *Hypertension*, 29: 1039-1043, 1997.
- 71. Sagawa K, Suga H, Shoukas AA, and Bakalar KM. End-systolic pressure/volume ratio: a new index of ventricular contractility. *Am. J. Cardiol.*, 40: 748-753, 1977.
- 72. Sagawa K. The end-systolic pressure-volume relation of the ventricle: definition, modifications and clinical use. *Circulation*, 63(6): 1223-1227, 1981.
- 73. Sato T, Yamashiro SM, Vega D, and Grodins FS. Parameter sensitivity analysis of a network model of systemic circulatory mechanics. *Ann. Biomed. Eng.*, 2(3): 289-306, 1974.
- 74. Saul JP and Cohen RJ. Respiratory Sinus Arrhythmia. In: Vagal Control of the Heart: Experimental Basis and Clinical Implications, edited by Levy MN and Schwartz PJ. Armonk, NY: Futura Publishing Co. Inc., 1994, p. 511-535.

- 75. Senzaki H, Chen CH, and Kass DA. Single-beat estimation of end-systolic pressure-volume relation in humans: A new method with the potential for noninvasive application. *Circulation*, 94(10): 2497-2506, 1996.
- 76. Shih H, Hillel Z, Declerck C, Anagnostopoulos C, Kuroda M, and Thys D. An algorithm for real-time, continuous evaluation of left ventricular mechanics by single-beat estimation of arterial and ventricular elastance. *J. Clin. Monit.*, 13:157-170, 1997.
- 77. Shishido T, Hayashi K, Shigemi K, Sato T, Sugimachi M, and Sunagawa K. Single-beat estimation of end-systolic elastance using bilinearly approximated time-varying elastance curve. *Circulation*, 102: 1983-1989, 2000.
- 78. **Staub NC.** Basic respiratory physiology. New York: Churchill Livingstone, 1991.
- 79. Stetz CW, Miller RG, Kelly GE, and Raffin TA. Reliability of the thermodilution method in the determination of cardiac output in clinical practice. Am. Rev. Respirat. Dis., 126: 1001-1004, 1982.
- 80. Stevenson LW and Perloff JK. The limited reliability of physical signs for estimating hemodynamics in chronic heart failure. *JAMA*, 261: 884-888, 1989.
- 81. Suga H, Kitabatake A, and Sagawa K. End-systolic pressure determines stroke volume from fixed end-diastolic volume in the isolated canine left ventricle under a constant contractile state. Circ. Res., 44: 238-249, 1973a.
- 82. Suga H, Sagawa K, and Shoukas AA. Load independence of the instantaneous pressure-volume ratio of the canine left ventricle and effects of epinephrine and heart rate on the ratio. Circ. Res., 32: 314-322, 1973b.
- 83. Suga H and Sagawa K. Instantaneous pressure-volume relationships and their ratio in the excised, supported canine left ventricle. Circ. Res., 35:117-126, 1974.
- 84. Sunagawa K, Yamada A, Senda Y, Kikuchi Y, Nakamura M, Shibahara T, et al. Estimation of the hydromotive source pressure from ejecting beats of the left ventricle. *IEEE Trans. Biomed. Eng.*, 27(6):299-305, 1980.
- 85. Sunagawa K, Maughan WL, Burkhoff D, and Sagawa K. Left ventricular interaction with arterial load studied in isolated canine ventricle. *Am. J. Physiol.*, 245(14): H772-H780, 1983.
- 86. Swan HJC, Ganz W, Forrester J, Marcus H, Diamond G, and Chonette D. Catheterization of the heart in man with the use of a flow-directed balloon-tipped catheter. N. Engl. J. Med., 283:447-451, 1970.

- 87. **Tajimi T, Sunagawa K, Yamada A, Nose Y, Takeshita A, Kikuchi Y, et al.** Evaluation of pulse contour methods in calculating stroke volume from pulmonary artery pressure curve (comparison with aortic pressure curve). *Eur. Heart J.*, 4: 502-511, 1983.
- 88. Takeuchi M, Igarashi Y, Tomimoto S, Odake M, Hayashi T, Tsukamoto T, et al. Single-beat estimation of the slope of the end-systolic pressure-volume relation in the human left ventricle. *Circulation*, 83(1): 202-212, 1991.
- 89. van der Velde ET, Burkhoff D, Steendijk P, Karsdon J, Sagawa K, and Baan J. Nonlinearity and load sensitivity of end-systolic pressure-volume relation of canine left ventricle *in vivo*. *Circulation*, 83: 315-327, 1991.
- 90. Weir EK, Michelakis ED, Archer SL, and Rubin LJ. Pulmonary hypertension. In: Cardiovascular medicine, edited by Willerson JT and Cohn JN. Philadelphia: Churchill Livingstone, 2000.
- 91. Welkowitz W, Cui Q, Qi Y, and Kostis JB. Noninvasive estimation of cardiac output. *IEEE Trans. Biomed. Eng.*, 38(11): 1100-1105, 1991.
- 92. Wesseling KH, Jansen JRC, Settels JJ, and Schreuder JJ. Computation of aortic flow from pressure in humans using a nonlinear, three-element model. Am. J. Physiol., 74(5): 2566-2573, 1993.
- 93. Wilde DJ. Optimum Seeking Methods. Englewood Cliffs, NJ: Prentice-Hall, Inc., 1964.
- 94. **Zong W, Moody GB, and Mark RG**. Reduction of false arterial blood pressure alarms using signal quality assessment and relationships between the electrocardiogram and arterial blood pressure. *Med. Biol. Eng. Comput.*, 42(5): 698-706, 2004.